INTERFACIAL EFFECTS AND INHOMOGENEOUS MAGNETIC STATES IN MAGNETIC HETEROSTRUCTURES

A Dissertation

by

PAVEL LAPA

Submitted to the Office of Graduate and Professional Studies of
Texas A&M University
in partial fulfillment of the requirements for the degree of

DOCTOR OF PHILOSOPHY

Chair of Committee,	Winfried Teizer
Co-Chair of Committee,	Axel Hoffmann
Committee Members,	Joseph Ross
	Wayne Saslow
	Ibrahim Karaman
Head of Department,	Peter McIntyre

August 2017

Major Subject: Physics

ABSTRACT

Many interfacial effects occurring in magnetic heterostructures are related to emergence of inhomogeneous magnetic states. In these states, a magnetic order and a direction of magnetization change significantly on the scale of a few nanometers along the thickness of the heterostructures.

This PhD dissertation covers interfacial effects and inhomogeneous magnetic states in three different types of magnetic heterostructures. First, we investigated an unusual exchange bias effect between pinned and unpinned uncompensated magnetization in antiferromagnetic FeMn, which is in proximity with diamagnetic Cu. Using a specially designed antiferromagnet-ferromagnet spin valves, it was shown that even a 110-kOe magnetic field cannot reverse the pinned uncompensated magnetization at the Cu/FeMn interface. The experimental results indicate that the pinning is induced by stress developed in the FeMn/Cu multilayers due to strong thermal contraction of Cu.

Second, we studied magnetic behavior of heterostructures composed of two immensely different ferromagnetic material: rare-earth Gd and permalloy, which are coupled antiferromagnetically. Magnetic field causes an appearance of in-plane domain walls and states in which magnetization is not collinear to a magnetic field. Using a combination of magnetometry and magnetotransport measurements, it was investigated how these inhomogeneous magnetic states evolve at different magnetic fields and temperatures. Fitting experimental dependences to the proposed micromagnetic model allowed obtaining microscopic parameters of the Py/Gd heterostructures. It was also discovered that microdisks composed of the Py/Gd multilayers demonstrate unusual

thermal behavior: the microdot magnetization can be transformed from a single domain state to a vortex state in a constant magnetic field by changing the temperature. Moreover, for some temperature ranges, the change in temperature is the only possibility to nucleate the vortex in the disks.

Third, we considered special superconductor/ferromagnet heterostructures, for which, the inhomogeneous magnetic states are constructed artificially to generate odd-triplet superconductivity. It was shown that the suppression of the critical temperature observed for the inhomogeneous magnetic states, which was reported previously by other groups, was not due to the odd-triplet superconductivity. Additionally, kinetic inductance measurements revealed that a slight change in the magnetic field affects the superconducting condensate much stronger than possible generation of the odd-triplet pairing.

DEDICATION

To

The bright memory of my father Lapa Nikolai Nikolaevich

ACKNOWLEDGEMENTS

I would like to express my greatest gratitude to all my scientific advisors who have worked with me throughout the course of my PhD program. I am very lucky that I have had this privilege to work with so many well-known scientists who are also such wonderful people.

First, I am sincerely thankful to Winfried Teizer my advisor from Texas A&M University. Dr. Teizer was always there to offer me encouragement and pushed me toward finishing my PhD. I enjoyed his guidance and support. At the same time, he provided me with the freedom of choosing my own way to solve problems and establishing new collaborations.

I want to express my deepest thanks to Igor V. Roshchin, without whose guidance I would not be here today. Dr. Roshchin has enabled me to have many opportunities I would not otherwise have had. Due to his support I became a graduate student at Texas A&M University. His unique approach to solving scientific problems and extreme attention to detail enabled me to develop as a scientist while simultaneously producing fruitful research. Additionally, he was always willing to extend his support outside of his normal working hours even for areas outside of the scientific spectrum. His quality of work and methods will continue to influence me through the course of my life.

I would also like to express my gratitude to Axel Hoffmann who offered me the unique opportunity to work at Argonne National Laboratory. He provided me with guidance and support both academically and with funding of my research. Dr. Hoffmann's deep insight in various scientific areas has been a great benefit and example to me. Outside

of his scientific expertise, I greatly admire Dr. Hoffmann's extraordinary capability to organize our work in the lab in a way that utilizes the best qualities of individual group members. Moreover, he has always approached me and my fellow lab mates with very uplifting and jovial attitude which always put me into a good mood.

I was lucky to work and collaborate with a lot of great scientists in Argonne National Laboratory. In addition to Dr. Hoffmann, I was mentored by Valentin Novosad, J. Samuel Jiang. Their invaluable expertise in different areas of magnetism and superconductivity tremendously impacted the projects I have been developing. I am sincerely thankful to John Pearson and Vladimir Efremenko for technical support and expertise on various scientific equipment in the lab. I express my thanks to all postdocs and graduate students in thin film group for the friendly atmosphere and fruitful collaborations: Trupti Khaire, Benjamin Jungfleisch, Wanjun Jiang, Stephen M. Wu, Wei Zhang, Hilal Saglam, Joseph Sklenar, and especially, my closest collaborator Junjia Ding.

I had a unique experience of conducting polarized neutron reflectometry measurements on the Magnetism Reflectometer at the Spallation Neutron Source at Oak Ridge National Laboratory. I am very thankful for this opportunity to work with the lead instrument scientist Valeria Lauter, a wonderful woman and a great scientist. I am also grateful to the tool scientists: Artur Glavic, Haile Ambaye. A detailed model that Artur Glavic developed for reflectometry data fits delivered crucial information on magnetic and atomic structures of the FeMn-based films. These fits were included into the dissertation.

I would like to thank my friend Dogan Kaya, a graduate student who had studied the exchange bias effect in the FeMn/Cu heterostructures in Dr. Roshchin's group at Texas

A&M University before I joined it. A part of the magnetometry measurements of the FeMn/Cu multilayers presented in this dissertation was obtained in collaboration with him. I am also thankful to Charudatta Phatak for assisting in conducting transmission electron microscopy.

I am thankful to Prof. Johan van Lierop from the Department of Physics and Astronomy at University of Manitoba and his graduate student Elizabeth Skoropata for acquiring the Mössbauer measurements and their analysis.

I would like to thank the members of my degree committee: Dr. Joseph Ross, Dr. Wayne Saslow, and Dr. Ibrahim Karaman. Guidance and feedback I obtained in private conversation with them and during my preliminary examination helped me to progress in my research.

Finally, I would like to thank Texas A&M University and Argonne National Laboratory for providing financial support during my PhD program.

CONTRIBUTORS AND FUNDING SOURCES

This work was supervised by advisors, Professors Winfried Teizer and Igor V. Roshchin of the Department of Physics and Astronomy, and co-advisor Doctor Axel Hoffmann of Argonne National Laboratory. The dissertation committee members were Professors Joseph Ross, Wayne Saslow of the Department of Physics and Astronomy and Ibrahim Karaman of the Department of Materials Science and Engineering.

Technical support and expertise were provided by John Pearson, Vladimir Efremenko, Valentin Novosad, J. Samuel Jiang, and Junjia Ding.

A part of superconducting spin valves covered in Chapter V was grown by Trupti Khaire.

Neutron reflectometry measurements were conducted on the Magnetism Reflectometer at the Spallation Neutron Source at Oak Ridge National Laboratory in collaboration with Valeria Lauter, Artur Glavic, Haile Ambaye. Artur Glavic developed a model for fitting reflectometry data.

Mössbauer measurements and their analysis were conducted by Professors Johan van Lierop and his graduate student Elizabeth Skoropata from the Department of Physics and Astronomy at University of Manitoba.

A part of magnetometry data presented in Chapter III was obtained in collaboration with a graduate student Dogan Kaya who was a member of Professor Roshchin's research group at Texas A&M University.

Transmission electron microscopy was conducted by Doctor Charudatta Phatak.

The work was supported by Texas A&M University, Texas A&M University – CONACyT collaborative research program, and the Department of Energy Office of Science, Basic Energy Sciences, Material Sciences and Engineering Division.

NOMENCLATURE

AC	Alternating Current
AF	Antiferromagnet (Antiferromagnetic)
AFSV	Antiferromagnet-Ferromagnet Spin Valve
BCS	Bardeen-Cooper-Schrieffer
DC	Direct Current
DOS	Density Of States
EB	Exchange Bias
ETO	Electrical Transport Option
F	Ferromagnet (Ferromagnetic)
GMR	Giant Magnetoresistance
KI	Kinetic Inductance
MPMS	Magnetic Property Measurement System
MRAM	Magnetoresistive Random-Access Memory
NR	Neutron Reflectometry
OOMF	Object Oriented MicroMagnetic Framework
PNR	Polarized Neutron Reflectometry
PPMS	Physical Property Measurement System
RE	Rare-Earth
RF	Radio Frequency
RKKY	Ruderman–Kittel–Kasuya–Yosida
SAF	Synthetic Antiferromagnet

SDCR	Single-Domain Coherent Rotation
SLD	Scattering Length Density
SQUID	Superconducting Quantum Interference Device
SV	Spin Valve
TEM	Transmission Electron Microscopy
TM	Transition Metal
VSM	Vibrating Sample Magnetometer
XRD	X-Ray Diffraction
XRR	X-Ray Reflectometry

TABLE OF CONTENTS

Page

LIST OF FIGURES

Page

CHAPTER I

INTRODUCTION

Magnetic materials exhibit a wide variety of interesting properties that give rise to fundamental research questions in magnetism. Additionally, studying magnetic materials has led to a large number of new technological applications. As an example, manipulation of magnetization at the nanoscale enabled creating efficient nonvolatile magnetic data storage media, which underlies modern information technologies. The recent endeavor to use the spin magnetic moment instead of the electric charge for signal transmission gave origin to spintronics, a quickly developing branch of magnetism.[1]

Two materials in close proximity to each other can mutually interact. The thin interfacial region between the materials possesses properties derived from both of them, as well as some unique properties that are not inherent to either of the adjoining materials. Combining one magnetic material with another magnetic or nonmagnetic material can cause an emergence of new phenomena at the interface. Thus, such proximity generates opportunities for exploring novel magnetic properties of materials.[2]

Special devices, so-called “heterostructures”, in which materials with different properties are combined with each other through common interfaces, are designed for exploiting these new properties and phenomena, which emerge at interfaces. Development of thin and ultrathin film-growth techniques and heterostructures-fabrication methods has led to significant progress in studying proximity effects experimentally. As of today, studying interfacial physics and proximity effects is one of the key topics of magnetism research. The discovered phenomena are of great interest from a basic science point of

view as well as for practical applications.[3] Magnetic multilayers are used as polarizers and analyzers in neutron scattering technology.[4] Due to anisotropic magnetoresistance and giant magnetoresistance effects, the resistance of specific magnetic heterostructures strongly depends on direction and amplitude of the external magnetic field. This property lies at the bottom of many magnetoresistive detectors. With respect to information technology, development of magnetic heterostructures has tremendously impacted magnetic data storage. For example, magnetic superlattices with strong perpendicular anisotropy are used as high-density magnetic recording media. A complex magnetic structure is a key component of a tunneling magnetoresistive read head,[5] which reads a bit of information in hard disk drives. Recently, it was discovered that the magnetization can be effectively switched by passing a spin-polarized current through magnetic heterostructures. Today, many efforts are undertaken to use this effect for developing a new, non-volatile, magnetic random-access memory.

For many practical applications or experimental studies that involve magnetic heterostructures, it is crucial to control the relative orientation of magnetization in different magnetic layers and a distribution of magnetization over a heterostructure thickness in general. It is also important to know how magnetization of the heterostructures reverses when an external magnetic field and temperature change. In this PhD work, the interfacial effects that occur at the interface with magnetic materials were studied. The work includes three projects focused on studying different magnetic heterostructures. The common aspect of the projects is controlling the spatial distribution of magnetization over the heterostructures' thickness which is crucial for understanding

microscopic processes that occur in the heterostructures. Thus, the common goal of these projects is to use interfacial interaction to stabilize inhomogeneous magnetic states in a controlled manner.

The first project considered in this PhD dissertation covers the effect of exchange bias which usually occurs due to an interaction of a ferromagnet and an antiferromagnet, and which manifests itself as a shift of the magnetization curve. Although the exchange bias effect has been intensively studied for the last 60 years, some aspects of its microscopic mechanism are still unclear. One of these unclear processes which underlies the effect is magnetization pinning. Understanding the mechanism responsible for this pinning would allow to resolve disputes about the origin of the exchange bias effect and can potentially lead to an effective control of exchange bias.

For a "classical" exchange bias system composed of a ferromagnet/antiferromagnet composite, the unidirectional anisotropy is due to a pinned uncompensated magnetization which occurs in an antiferromagnet after the system is cooled down through the antiferromagnetic ordering temperature in the presence of a magnetic field. Thus, it is crucial to understand: how does the uncompensated magnetization occur in an antiferromagnet, which microscopic mechanism is responsible for the pinning of this magnetization, and how does this pinned uncompensated magnetization behave at different temperatures and magnetic fields? When a classical exchange bias system is investigated using magnetometry, most of the measured magnetic signal comes from the ferromagnet. Hence, it is difficult to trace how the magnetic properties of the antiferromagnet change. Thus, magnetometry measurements of the

classical exchange bias system do not convey important information about the processes that occur in the antiferromagnet. In this project, a “non-classical” exchange bias system, which is composed of antiferromagnetic FeMn and diamagnetic Cu is considered. Because the system does not contain any explicit ferromagnetic layer, the entire magnetic moment is due to the uncompensated magnetization. This allows the uncompensated magnetization to be defined very accurately. To analyze the behavior of the pinned magnetization at different temperatures and magnetic fields a new magnetoresistive technique was developed. Using the technique, it was demonstrated that the pinned magnetization cannot be reversed even if a 110-kOe magnetic field is applied. This experimental observation allowed us to make an important conclusion on the nature of the pinning.

Generally, tuning the interaction between two ferromagnetic layers allows for controlling magnetic parameters of these heterostructures including coercitivity, Curie temperature, saturation magnetization, and even chirality of the magnetization. Among different magnetic heterostructures, multilayers composed of transition and rare-earth metals are a special category because of various unique properties. First, the magnetic moment in rare-earth metals is due to strongly localized f-electrons, which makes the exchange interaction responsible for the ferromagnetism much weaker for the rare-earth metals than for most of the transition metals. In particular, this explains a comparatively low Curie temperature of ferromagnetic rare-earth metals (Gd has the highest among them, Curie temperature of 293 K). The proximity between the rare-earth and transition metals results in a significant change in the magnetic order at the interface. Second, the sign of exchange coupling between rare-earth and transition metals differs depending on the rare-

earth elements. For the heavy rare-earth Gd and transition metals the coupling is antiferromagnetic.[6, 7] This provides an opportunity to synthesize artificial ferrimagnets for spintronics application. Due to the antiferromagnetic coupling and reduced magnetic order in Gd, applying a magnetic field yields in-plane domain walls in the Gd/transition metal heterostructures. That is, the magnetization gradually changes direction along the thickness of the heterostructures. It means that contrary to ordinary ferromagnets where magnetic fields erase domain walls, a magnetic field generates domain walls in the heterostructures composed of Gd and a transition metal.

In the second project of the dissertation, the formation of the in-plane domain walls and magnetization reversal in the heterostructures composed of permalloy (Py), magnetically soft $Ni_{81}Fe_{19}$ alloy, and Gd were studied using magnetometry, magnetotransport, and micromagnetic simulations. The combination of the different techniques allowed us to determine the distribution of magnetization over the heterostructure thickness at different temperatures and magnetic fields. In addition, a mechanism of the magnetization reversal in artificial-ferrimagnet microdisks composed of Py and Gd was investigated.

The third part of the dissertation covers the effect of proximity between a superconductor and a ferromagnet. Despite a well-known fact that ferromagnetic and superconducting materials are antagonistic to each other, a series of theoretical works predicts an emergence of new superconducting states at the interface between these materials. In particular, it was shown that if a thin superconducting layer is in proximity with two ferromagnetic layers, whose magnetizations are not collinear, it leads to a

generation of so-called odd-triplet Cooper pairs at the superconductor/ferromagnet interfaces. These pairs have a non-zero projection of the total spin on the magnetic field direction and thus can propagate for a long distance in the ferromagnets. The goal of the project is to check if it is possible to excite long-range spin-triplet pairing in a superconducting layer which is in proximity with two ferromagnetic layers and how the excitation affects the superconducting condensate. Again, controlling magnetization distribution over the heterostructure thickness is crucial because the pairing is sensitive to the mutual orientation of the magnetizations. For this purpose, a specially designed spin valve was fabricated enabling control of the magnetizations in the valve by a static magnetic field.

CHAPTER II

SAMPLE-FABRICATION AND MEASUREMENTS TECHNIQUES

II.1 Sample Fabrication Techniques

II.1.1 Magnetron sputter deposition

Sputter deposition, or sputtering, is a process of material deposition onto a substrate by ejecting atoms from a material target. Prior to sputtering, a vacuum chamber is pumped to a low base pressure, typically of the order of 10^{-8}–10^{-7} Torr. Then, the chamber is filled with an inert gas (Ar). Free electrons, which naturally appear in the chamber due to the negative potential applied to the target, collide with Ar atoms and ionize them. The electrons generated after the ionization collide with other Ar atoms, producing additional positively charged ions. The ionization process leads to the formation of a hot stable plasma in the chamber. Due to an electrostatic attraction, the positive Ar ions are accelerated toward the target, bombarding it. The high kinetic energy of the bombarding ions causes the atoms to be ejected from the target and move toward the substrate. The atoms adhere to the substrate, binding with each other, forming a continuous film over time.

In order to accelerate the deposition rate and isolate the substrate from the hot plasma, strong permanent magnets are installed underneath the target. The magnetic field produced by the magnets keeps electrons in the vicinity of the target. This provides that, first, the hot plasma does not extend to the substrate, and second, the localization of the plasma strongly enhances the probability of the ionization, significantly increasing the deposition rate.

For growing superconducting spin valves and synthetic antiferromagnets, the homogeneity of the deposition is especially important. Thus, to improve the uniformity of the thickness over the films, the position of the substrate holder was oscillated with respect to the target.

II.1.2 Optical lithography

Optical lithography is used for creating a photoresist mask on a substrate. Subsequent material deposition in combination with lift-off or material etching enable creating structural elements on the substrate. Two different lithography processes were used in this work for the samples fabrication: contact-mask and maskless optical lithography.

For the mask lithography, a Karl Suss MA6 mask aligner was used. This instrument brings a specially prepared mask containing a desirable design into proximity with a substrate. The vacuum mode was utilized, which removes the air gap between the mask and substrate, thus providing a higher resolution. After that, a high-intensity ultraviolet light was illuminated onto the substrate through the mask. This changes the chemical structure of the exposed photoresist. For a positive photoresist (s1813), the area exposed to the light becomes soluble and can be removed by a developer (CD-26). As the result, a photoresist mask is formed on the substrate surface. For the maskless lithography, a narrow light beam is traced over a film's surface exposing some of its areas. A Microtech laser writer LW405 was used for maskless lithography.

The contact-mask lithography yields high resolution; however, it lacks versatility provided by the laser writing. Different masks are required for patterning different designs.

In special cases, it is necessary to obtain a negative tone using a positive photoresist, for example, to pattern an image of photoresist disks using a mask, which in combination with a positive photoresist provides an array of holes. In these cases, an image-reversal procedure is used. The procedure consists in baking an exposed wafer in an ammonia environment. When the ammonia penetrates into the exposed area, it changes the chemical structure of the exposed resist. This makes the originally exposed area insoluble in the developer, while the originally unexposed area can be removed in the developer after flood exposure of the wafer. For the image reversal procedure used in this work, samples were baked at 100 ºC in NH_3 environment for 30 minutes (Yield Engineering Systems image reversal oven), flood exposure was performed using Karl Suss MA6 mask aligner.

II.1.3 Ion beam milling

Ion beam milling is an anisotropic physical-etching process which is used for controllable removal of materials from selected areas of the films. The method is based on blasting away material by bombarding a film with high-energy Ar ions. For selective milling, a photoresist mask is patterned on top of the film using optical lithography. The vacuum chamber with the sample and ion-beam gun are pumped to 10^{-7} Torr. After that, the pressure of 1.5×10^{-4} Torr is set by letting Ar gas flow into the chamber. To produce Ar ions, the electrons emitted from the filament move toward the anode and collide with Ar atoms, producing Ar ions. Similarly to the magnetron sputter guns, strong permanent magnets are installed near the anode to enhance the probability of Ar ionization and hence ion beam intensity. The electric field, produced by the negatively biased grid, accelerates the ions toward the film. Due to electric repulsion, the beam of the positive particles tends

to diverge. Additionally, a large positive charge can build up at the substrate over time, deflecting the beam and thus decreasing the milling rate. To avoid these undesirable effects, a neutralizer filament is placed in the beam path. The electrons emitted by the filament into the beam make it quasi neutral.

It is preferred to direct the beam at a well-defined angle to the film surface. This provides optimum removal of the milled material. At the same time, the sample holder must be rotated in order to obtain a uniform milling profile. Our setup lacks the rotating stage, consequently, only small samples were ion-milled (1.5 cm × 1.5 cm and smaller). These samples were installed with the surface of the film perpendicular to the ion beam.

II.2 Measurements Techniques

II.2.1 SQUID magnetometry

Magnetic moments of the samples were measured using superconducting quantum interference device (SQUID) magnetometers (Quantum Design Magnetic Property Measurement System [MPMS]).[8] The main parts of the magnetometer are a 70-kOe superconducting magnet and a detection coil which is connected to a SQUID sensor. The detection coil is a specially shaped superconducting wire operating as a second-order gradiometer, which is kept in the center of the superconducting magnet under a liquid-helium temperature. The sample is mounted on a non-magnetic holder (set inside a plastic straw or glued to a quartz rod), which is attached to a long rod. The assembly is vertically set into the magnetometer's chamber so that the sample is located at the center of the detection coil. The temperature inside the chamber near the sample can be changed in the range between 1.8 K and 400 K, and can be controlled with the accuracy of 0.5 K.

The operational principle of the device is as follows. The rod with the sample is moved in a controlled fashion for a DC (direct current) scan mode, the motion is a series of discrete predefined displacements; for a VSM (vibrational sample magnetometer) mode, the motion is a vibration with predefined frequency and amplitude. Since the sample is inductively coupled to the detection coil, the motion causes induction of superconducting current in the coil. In turn, the detection coil is coupled to the SQUID loop using a flux transformer. The read-out electronics control the voltage on the feedback loop in order to cancel the magnetic flux through the SQUID loop. Thus, the SQUID detector operates as an extremely sensitive current-to-voltage converter: current induced in the detection coil is converted into a voltage in the SQUID detector.[9] Since the operation of the SQUID detector is strongly influenced by the surrounding magnetic field, the detector is installed outside the magnet and completely isolated from the magnetic field by a superconducting shield. Thus, the voltage on the SQUID detector is defined only by the amplitude of the current in the detector's circuit. This voltage is proportional to the variation in the magnetic flux through the detection coil. To determine the magnetic moment of the sample, the magnetometer's software fits the dependence of the voltage on the sample position using a model spatial response provided by an ideal magnetic dipole.

Although the sensitivity of the SQUID magnetometer is 1×10^{-8} emu, there are parasitic effects which stochastically corrupt some measurement scans. First, it is nominally implied that due to the gradient structure of the second-order detector the uniform magnetic field does not induce any current in the coil. In practice, the coils of the detectors are never perfectly balanced, as the result of this, the current is induced in the

circuit when the magnetic field changes, this current produces significant noise. Quenching the SQUID circuit after each field-ramping procedure allows to partially eliminate the parasitic current. It was determined that this noise causes a strong distortion of some measurement scans. Second, a significant noise is produced by the superconducting vortex flow in the solenoid. To reduce the influence of these parasitic effects, seven scans were produced for each data point, and three out of seven measured magnetic moments that showed the highest deviation from the average value were rejected. Additionally, each measurement scan was performed 30–45 seconds after the magnetic field was stabilized. This pause is required for stabilization of magnetic vortices in the superconducting magnet and increasing the stability of the magnetic field.

II.2.2 Electronic transport measurements

All transport measurements were conducted in the conventional four-probe geometry using a physical property measurement system (PPMS) by Quantum Design. In this system, temperature can be changed in the 1.8–300 K range, and the maximum magnetic field that can be applied is 140 kOe. The samples under study were cut into narrow stripes with dimensions around 10 mm×2 mm. Thin silver wires were used as leads. They were attached to the samples using a wire bonder. To apply an in-plane magnetic field at different angles with respect to the current or magnetization, the samples were installed on a horizontal rotator. Because the rotator's stage contains a thermometer located in close proximity to the sample, the external temperature can be measured and controlled very accurately. The zero-degree angle on the rotator corresponds to the orientation of the stripe in which its long edge is parallel to the external magnetic field.

Most of the measurements were conducted using an electrical transport option (ETO) of the PPMS, which implies passing an alternative current (AC) and measuring voltage at a given excitation frequency using a lock-in amplifier. Since the sample stripes in this study have a significant width, their resistance is below 100 Ω. Hence, in order to measure the resistance with a sufficient accuracy, a current of 1 μA was applied.

For the ETO measurements, the maximum frequency of the AC current is 200 Hz. To measure kinetic inductance of a superconducting wire, an AC current with a frequency of up to 100 kHz must be applied. Thus, for the kinetic inductance measurements, a Keithley 6221 current source capable of providing an AC current with the frequency of up to 100 kHz was used for the current biasing, while the voltage at the excitation-current frequency was measured using an SR830 DSP lock-in amplifier. The measurement devices and the PPMS were controlled via GPIB and a custom LabVIEW program.

II.2.3 Polarized neutron and X-ray reflectometry

SQUID magnetometry measures magnetization of samples averaged over volume. Sometimes, it is important to determine the spatial distribution of the magnetization over the heterostructure thickness. Polarized neutron reflectometry (PNR)[10] is a very sensitive non-destructive technique which allows measuring nuclear and magnetic profiles of magnetic heterostructure with a sub-nanometer resolution.[11-13]

The operational principle of the technique is as follows. Neutrons produced by a neutron source pass through a polarizer and a set of slits, which yields a highly polarized collimated neutron beam. The beam hits the surface of the measured film at a small angle (typically $0^o - 2^o$) which enables neutrons to penetrate into the film and scatter on its

nuclear and magnetic structures. Due to diffraction of the scattering neutrons, the intensity of the reflected beam strongly depends on the incident and reflected angles. The resulting angular dependence of the reflectivity for a smooth multilayer can be represented as a combination of a dissipative and quickly oscillating components. The reflection can be modeled as a scattering on a one-dimensional spatial potential $V(z)$, which varies along the thickness, z, of the multilayer. $V(z)$ can be expressed as

$$V(z) = \frac{2\pi\hbar}{m} N(z)b(z) \pm (\vec{\mu}(z) \cdot \vec{B}), \qquad \text{(II-1)}$$

where m is the neutron mass, $N(z)$ and $b(z)$ denote distributions of the nuclear density and the coherent scattering length over the film thickness, respectively, while $\vec{\mu}(z)$ is the distribution of the magnetization and $\vec{B}$ is the magnetic induction in the film.[14] The $N(z)b(z)$ term, which is usually called a neutron scattering length (SLD) density, characterizes the nuclear form factor of the multilayer, whereas $\vec{\mu}(z) \cdot \vec{B}$ describes the interaction with the magnetization form factor.

There are two factors important for understanding the polarized neutron scattering. First, the sign of the magnetic interaction depends on the neutron polarization (spin-up or spin-down). Second, for multilayers composed of strong ferromagnets, the magnetic- and nuclear-interaction terms are of the same order of magnitude. These properties enable simultaneous analyses of the structural profile of the multilayers and the depth dependence of the magnetization along the magnetic field by measuring reflectivity for two neutron polarizations. The modeling and refinement of the experimental reflectivity curves is usually conducted numerically using the Parratt formalism,[15] a recursive model which takes into account indexes of refraction and interfacial roughness of heterostructures.

Along with studying the magnetization along the magnetic field, PNR also allows analyzing the in-plane magnetization, which is perpendicular to the magnetic field. This is achieved by measuring the number of neutrons that change polarization after the reflection, *e.g.*, spin-up to spin-down and spin-down to spin-up. This, so-called, spin-flop reflectivity is extremely useful for studying the magnetization distribution in antiferromagnetically coupled multilayers,[10, 16] as well as multilayers in which the magnetization is not collinear over the thickness (exchange-spring magnets[17]).

X-ray reflectometry (XRR) is a technique similar to neutron reflectometry (NR) without polarization analysis. A collimated monochromatic x-ray beam hits a surface of a multilayer, and the intensity of the reflected X-ray beam is measured in a small-angle specular geometry. Similarly to NR, the angular dependence of the reflectivity is modeled as a scattering on a one-dimensional potential, which enables determining the chemical form factor (x-ray SLD profile) for the multilayer. XRR provides information about the electronic and, hence, related chemical structure of a multilayer. To investigate magnetic structure of heterostructures, along with PNR, resonance x-ray magnetic scattering and x-ray circular dichroism techniques can be used.

The PNR measurements were performed at the BL-4A beamline of the Spallation Neutron Source in Oak Ridge National Laboratory. The data were obtained using a time-of-flight magnetism magnetometer with highly polarized beam ($1.8\ \text{Å} < \lambda < 14.0\ \text{Å}$; $\Delta\lambda = 2.74\ \text{Å}$). Small angle x-ray reflectometry measurements were performed with Philips and Bruker diffractometers using Cu K-alpha radiation.

The PNR measurements were conducted by Pavel Lapa (the author of the dissertation) and Igor Roshchin, in close collaboration with the instrument scientists: Valeria Lauter, Artur Glavic, and Haile Ambaye. Pavel Lapa (the author of the dissertation) processed the PNR data. However, due to Artur Glavic rich experience, a model that he developed for fitting reflectometry data provided more crucial information on the magnetic and atomic structures of the samples. Artur Glavic's fits were included into the dissertation.

CHAPTER III

EXCHANGE BIAS EFFECT IN IRON-MANGANESE/COPPER HETEROSTRUCTURES

III.1 Introduction to Exchange Bias

III.1.1 Challenges of exchange bias

In 1956, Meiklejohn and Bean[18] discovered that cooling oxidized Co particles in an external magnetic field gives rise to a unidirectional anisotropy or so-called "exchange bias" (EB). It was shown that the direction of the cooling magnetic field defines a preferred, "easy" direction for the magnetization of Co, which causes the magnetization curve of the particles to shift along the magnetic-field axis (Figure 1). Meiklejohn and Bean realized that the EB occurs due to an interaction between a ferromagnetic core of the particle (Co) and its antiferromagnetic shell (CoO). The effect has been intensively studied for the last 60 years, which has led to discoveries of hundreds of new EB systems, including thin films,[19] fine particles,[18, 20] and bulk materials.[21]

The ongoing interest toward the EB effect is stimulated by three main factors. The first factor is a fundamental aspect. Up to date, some properties of the ferromagnet-antiferromagnet interaction and the EB, in particular, still remain unclear. The development of the theory is hampered by the lack of understanding of microscopic processes that occur at the interface between a ferromagnet and an antiferromagnet. There is no clear picture of how structural and magnetic properties of ferromagnetic and antiferromagnetic materials change at the interface. The second factor is that the antiferromagnetic materials are much less studied than the ferromagnetic ones. The main

reason for this is that there are fewer experimental techniques available for characterization of antiferromagnets. To some extent, the study of the EB effect can be regarded as one of these techniques. For example, analysis of the EB effect can deliver such crucial information about the antiferromagnet as its magnetic anisotropy, the size of antiferromagnetic domains and their thermal stability. The third factor stimulating the interest toward EB is its use for practical applications. The ability to pin magnetization in a specific direction has been utilized in magnetic hard drive read heads and sensors. For example, EB is used to stabilize magnetization of reference layers in GMR spin valves and MRAM tunnel junctions.[22] There are efforts to use the EB for "engineering" magnetic anisotropy.[23, 24] There are evidences that the EB helps overcoming the superparamagnetic limit[25] for magnetic nanoparticles[26, 27] as well as assisting stabilization of domains in magnetic media.[28, 29] It is believed that an enhancement of the EB in three-dimensional bulk compounds could lead to developing novel rare-earth-free permanent magnets.[21, 30]

III.1.2 The phenomenological picture and theoretical models of EB effect

The term "classical EB system" is commonly used to refer to a bilayer heterostructure composed of a thin antiferromagnetic (AF) layer and a ferromagnetic (F) one. The Curie temperature of the F layer, T_C, is typically higher than the Néel temperature of the AF layer, T_N, *i.e.*, $T_C > T_N$. The adopted phenomenology of the exchange bias mechanism in the system can be described as follows. At T above T_N, the sample is subjected to a magnetic field that is sufficient to saturate the magnetization in the F layer. The AF is in the paramagnetic phase at this temperature [Figure 1(a)]. When the sample is cooled down through T_N in the magnetic field (field-cooling procedure), the magnetic

moments of the AF atoms near the AF/F interface are exchange coupled to the moments in the F layer, and depending on the sign of the coupling, they are aligned along or opposite to the magnetization in the F layer [Figure 1(b)]. Let us assume without loss of generality that the direction of the magnetic field during the field-cooling is defined as positive. If the AF has a sufficiently high anisotropy, the uncompensated moments in the AF layer which are located near the interface with the F layer, stay pinned below T_N. When the hysteresis loop is measured at $T < T_N$, the magnetization in the F layer cannot rotate freely because it is coupled to the pinned uncompensated moments at the interface. In the case of ferromagnetic coupling between the AF and F layers, if the pinned moments are aligned along the positive direction of the magnetic field and the field is swept from the positive to the negative direction, the reversing of the F magnetization is impeded by the anchoring force produced by the pinned layer [Figure 1(b)]. Hence, the first coercive field is higher than in the case of the F alone, without the AF layer. When the magnetic field is swept in the opposite direction, the magnetization reversal is assisted by the pinned layer which tends to align the magnetization in the F along the positive field direction. The second coercive field decreases in relation to that for the single F layer. As a result, the hysteresis loop becomes shifted along the field axis in the negative direction [Figure 1(b)]. The value of the shift is called EB field, H_E. If the pinned magnetization is along the negative direction of magnetic field, the mechanism remains the same, but instead of the loop shift toward the negative fields, it is shifted in the positive direction of the field.

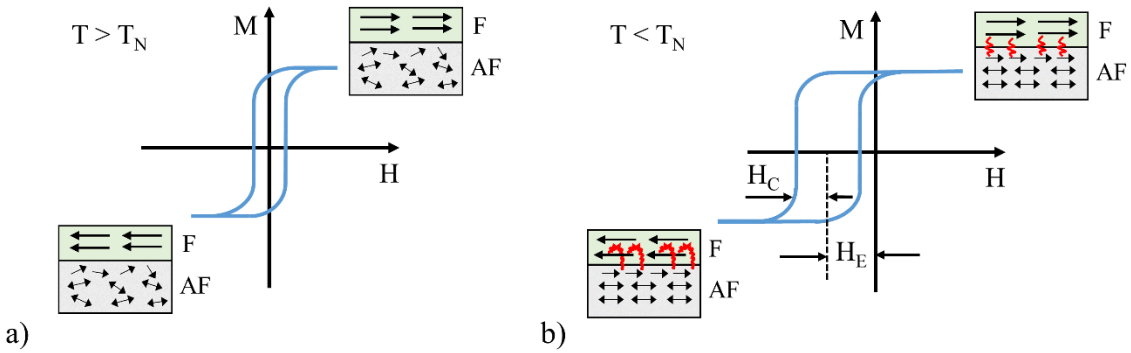

Figure 1 Schematic hysteresis loops of a film composed of ferromagnetic (F) and antiferromagnetic (AF) layers and magnetization inside the layers at (a) temperature T above the Néel temperature of the AF, T_N, and (b) after the bilayer was cooled down in an external magnetic field below T_N.

A number of theoretical models were proposed for a quantitative description of the EB. Importantly, none of these models is universal, *i.e.*, each model can explain some experimental observations for a particular EB system, but not all of them. The main problem is that all the models are based on oversimplified atomic and magnetic structures of the AF-F interface which seems to affect the validity of the results. Furthermore, different materials combinations may emphasize different aspects of the complex interactions between F and AF layers.

The first, intuitive, model of the EB effect was proposed by Meiklejohn and Bean[18] for an AF with a fully uncompensated interface. They assumed that the F and AF layers are in a single-domain state, and the corresponding macro-spins can rotate coherently in the plane of the film (Figure 2). After the AF/F bilayer is cooled down through T_N in a magnetic field, the entire uncompensated surface of the AF gets pinned in the direction of the field. The strength of this pinning is defined by the anisotropy of the AF, K_{AF}, which

is assumed to be high. Similarly to the Stoner-Wohlfrarth model,[31] the energy of the AF/F bilayer per unit area can be represented as

$$E_{Total} = - M_F H t_F \cos(\varphi_H - \varphi_F) + K_F t_F \sin^2(\varphi_F) + \quad \text{(III-1)}$$

$$+ K_{AF} t_{AF} \sin^2(\varphi_{AF}) - J_{EB} \cos(\varphi_F - \varphi_{AF}),$$

where t_F and t_{AF} are thicknesses of the F and AF layers, respectively, M_F is the magnetization and K_F is the anisotropy of the F layer, J_{EB} is the areal coupling energy between the F and AF layers.[32] Minima of E_{Total} with respect to φ_F and φ_{AF} define stable configurations of spins at a given field, which enables simulating a hysteresis loop and determining H_C and H_E. For the case when the direction of spins in the AF layer is fixed, the Meiklejohn-Bean model provides

$$H_E = \frac{2J_{EB}}{M_F t_F}. \quad \text{(III-2)}$$

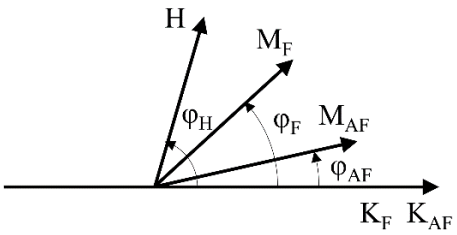

Figure 2 Schematic illustrates the orientations of magnetizations (M_F, M_{AF}), magnetic field (H), and anisotropies (K_F, K_{AF}) in the Meiklejohn and Bean model.

The absolute value of the EB field calculated using the Meiklejohn and Bean model significantly exceeds the EB field observed in the experiments.[19] It had been realized that the rigid-spin approximation imposed too strong of a limitation for the spins in the AF and F layers. The experimental results indicate that the spin structure of the AF layer is not preserved during the magnetization reversal in the F layer.[12] Néel[33] proposed

that a considerable overestimation of the coupling energy can be avoided if it is assumed that the exchange stiffness in the F and AF is finite and the anisotropy of the AF is low. Under these assumptions, magnetization reversal occurs through the nucleation of an in-plane domain wall, a part of which is located in the AF layer. A significant amount of energy is required for the nucleation of a domain wall, which results in a considerable reduction of the EB field. The Néel model yields H_E comparable to that observed in experiments. The main drawback of the model is that the F layer must be thick enough to accommodate the in-plane domain wall. The concept of in-plane domain wall in the AF layer was further developed in the Mauri[34] model and a partial-wall theory proposed by Kim and Stamps.[35]

Meiklejohn-Bean and Néel models are based on the assumption of a totally uncompensated interface in an AF, which is unlikely to be realized in practice. An introduction of monoatomic steps and defects into these models would drive the absolute energy of the AF-F interaction and consequently the EB field to zero. Malozemoff[36] proposed a model predicting the EB for any randomly disordered AF surface. For this, a totally compensated AF surface with monoatomic defects was considered. It was shown that, due to each defect, reversing the spin structure in the AF or F layers changes the energy of the system by E_D. The sign and the absolute value of E_D depend on the defect size and location, but on average, for each defect, $| E_D | = 2zJ$, where z is a number of order unity and J is the exchange coupling constant. It was proposed that, in order to minimize the local interfacial energy, the AF layer breaks into domains when the AF/F bilayer is cooled down through the Néel temperature. At low temperatures, this lateral domain

structure gives rise to an effective anisotropy which makes it more favorable for the magnetization in the F layer to be aligned along the direction of the cooling field. The Malozemoff model predicts that

$$H_E = \frac{2\sqrt{A_{AF}K_{AF}}}{M_F t_F}, \qquad \text{(III-3)}$$

where A_{AF} is the exchange stiffness in the AF. One can see that, similarly to the Meiklejohn-Bean model, H_E is inversely proportional to the magnetization of the F layer and its thickness. Equation (III-3) provides reasonable values of H_E for some real EB systems.[32]

In the Malozemoff model, the pinned AF domains and concomitant EB effect appear due to interfacial roughness. However, in addition to the defects at the interface, real AFs have defects in the bulk, which influence the nucleation of the AF domains. To improve the Malozemoff model, Nowak *et al.*[37, 38] proposed a so-called "domain state model" of the EB. Their idea was that any AF, in addition to defects at the interface, has some defects throughout its volume. Some of these defects are locally non-magnetic. Similarly to the Malozemoff model, if the sample is cooled down in a magnetic field, domains form in the AF. However, in contrast to the Malozemoff model, the domain walls pass mostly through the non-magnetic sites. This causes a significant reduction of the exchange energy related to the domain wall nucleation. The AF domain structure formed during the field-cooling procedure favors the orientation of the F magnetization along the cooling field, which results in the EB shift of the hysteresis loop. The main result of the domain state model, namely, the EB depends on the concentration of non-magnetic defects

in an AF layer was also confirmed experimentally. Thus, it was shown the dilution of an AF CoO layer with non-magnetic Mg defects[39] or by controlling the amount of O sites during the oxidation of CoO[40] results in the significant enhancement of the EB field.

Koon[41] applied micromagnetic numerical calculations to determine the spin configuration at the F/AF interface. It was discovered that in the case of a fully compensated interface, the spins in a few atomic monolayers of the AF layer, next to the AF/F interface, tend to rotate to 90º with respect to the magnetization in the F layer. This leads to a formation of a domain wall in the AF parallel to the interface. A similar spin-flop state occurs in an AF in a high magnetic field. According to Koon's calculations, if the AF layer is sufficiently thick, the spin flop state in the AF layer produces an asymmetric energy landscape for the magnetization in the F layer. The energy asymmetry can be treated as an effective unidirectional anisotropy which yields the EB effect. The main limitation of Koon's model is that the spins are restricted to rotate in plane. Similarly to Koon's approach, Schulthess and Butler[42] used a microscopic Heisenberg model. They showed that, if the condition of the in-plane rotation is not imposed, the EB effect does not occur and the spin-flop state results only in enhancing coercivity. On the other hand, it was demonstrated that the presence of the defects at the AF/F interface causes the EB effect. Thus, Schulthess and Butler confirmed the validity of the Malozemoff model micromagnetically.

All models considered so far are intended for explaining the EB shift of the hysteresis loop. However, there are other phenomena related to the EB effect that are left uncovered by these theories. First, it was observed that the EB-shift of the hysteresis loop

is accompanied by an increase in the coercive field.[43] Among the discussed models only the Schulthess and Butler approach explains the enhancement of the coercivity. Second, some EB systems after being cooled down through the Néel temperature are in a state that is not stable thermodynamically. The experiments show that cycling the magnetic field results in a reduction of H_C and H_E as well as modification of the loop shape, a so-called "training effect".[44-47] Third, in addition to the unidirectional pinning and the increase in coercivity, the hysteresis loop of an AF/F bilayer may drastically change its shape if the bilayer is cooled down in a magnetic field; sometimes the loop may become asymmetric.[48] In order to address all these issues, a spin-glass model[49, 50] of the EB was developed.

Within the spin-glass model, it is assumed that due to the chemical intermixing of materials and defects, the interface between the F and AF layers is not perfect, and hence, the atomic and spin structures of the materials may be frustrated at the AF/F interface. For the film cooled down in a magnetic field, the frustrated spins can be divided into two categories according to their pinning: frozen-in and rotatable. The rotatable spins respond to the magnetic field, reversing with the magnetization in the F layer. However, the frustration results in a complicated energy landscape for the magnetization in the F layer. For the rotatable spins, this impedes the reversal, which results in the enhancement of the coercivity. Most of the frozen-in spins are rigidly pinned, the coupling of these spins with the F layer yields the shift of the loop. Glassiness causes a part of the frozen-in spins to flip from the pinning direction if a high enough magnetic field is applied, which gives rise to the training effect. Based on the fact that the spin-glass model is capable explaining an enhancement of coercivity, training effect, the change in hysteresis loop shape, it provides

a good description of the EB effect for some EB systems. However, its main disadvantage is that it depends on many parameters defined by the glassiness of the material at the F/AF interface, which are extremely difficult to define.

Different materials have different crystal structures, and furthermore, the atomic and magnetic structures of the AF/F interfaces may vary significantly for different systems. This makes it fundamentally impossible to develop a universal model of EB. There are a number of detailed reviews covering the theoretical[23, 32, 51, 52] and experimental[52-55] aspects of the EB effect.

III.1.3 Motivation to study non-classical exchange bias system

The phenomenological picture and most models of the EB are built on one common assumption: an AF has a pinned uncompensated magnetization at the boundary with the F layer and this pinned magnetization is responsible for shifting the loop. Two important questions arise. First, what is the origin of this pinned uncompensated magnetization? What is the role of the interface in the development of the uncompensated magnetization and its pinning? Answers to these questions would allow developing more accurate microscopic mechanism of the EB effect.

For a perfect AF, the spin structure can be represented as a combination of different spin sublattices with magnetic moments that compensate each other. This provides a zero net magnetization inside the perfect AF. However, it does not mean that a complete compensation must also occur at the surface of the AF. For example, if the entire surface consists of one AF sublattice, this dominating sublattice is responsible for the appearance of the uncompensated magnetization at the surface.[56] Moreover, even if the surface is

composed of equal numbers of spins from different AF sublattices, its magnetization can still be uncompensated if the sublattices become non-equivalent at the surface. For example, it was shown that the equivalence of different AF sublattices can be broken at the surface of magnetoelectric AFs.[57] Importantly, for a magnetoelectric AF or an AF with a dominated sublattice, the uncompensated surface magnetization is an integral part of the AFs staggered spin structure. This means that to reverse this uncompensated magnetization, the entire antiferromagnetic domain must be reversed. This property makes this surface magnetization extremely stable.

It is known that the crystallographic structure of a real AF film cannot be absolutely perfect. Local drift of crystallographic composition, strain, and dislocations cause the appearance of uncompensated spins inside an AF and at its surface. The uncompensated spins in the depth of an AF provide a small net magnetization. In regards to the pinning, first, the magnetic moments on defects (at the surface or in the bulk of an AF) can get pinned because of the high magnetic viscosity or spin glassiness. Second, similarly to the Malozemoff[36] and Koon[41] models, if the AF with the uncompensated magnetization is cooled down in a magnetic field, it can become energetically favorable for the AF to break into domains. The majority of the uncompensated moments contained in the AF domains align along the cooling field thus minimizing the Zeeman energy. On a microscopic level, the uncompensated moments related to defects are not an integral part of the AF staggered structure. The neighboring-atom interaction leads to the appearance of an effective unidirectional anisotropy for these uncompensated moments rather than rigid pinning expected from AFs with a dominating sublattice at the interface.

A real AF always has some uncompensated magnetization. Besides, there are mechanisms which provide a part of the uncompensated magnetization to become pinned after cooling the sample in a magnetic field. However, if there are pinned and unpinned moments in AFs and they interact with each other, is it possible to observe the EB effect in a system which consists of an AF only? To answer this question, the magnetic properties of multilayers composed of AF FeMn and non-magnetic (diamagnetic) Cu were studied. Although there is no explicit F layer in the FeMn/Cu multilayers, significant magnetization (about 0.1 μ_B/f.u., μ_B is Bohr's magneton) develops at low temperature. Moreover, the FeMn/Cu multilayers demonstrate EB despite the absence of an explicit F layer, and hence, it is not a classical EB system.

The main motivation for this project was to determine the mechanism responsible for the appearance of the uncompensated magnetization and its pinning in the FeMn/Cu heterostructures and to obtain distribution of the pinned and unpinned magnetization in the FeMn layers. To do this, a series of FeMn/Cu and FeMn/Ta bilayers and multilayers were fabricated and systematically studied using magnetometry, magnetotransport, neutron-reflectometry, and Mössbauer techniques. To investigate the interdependence of structural and magnetic properties of FeMn, micro-cantilevers were used for studying the dependence of the internal stress on temperature. Additionally, a special antiferromagnet-ferromagnet spin valve was developed to analyze the pinning of the uncompensated magnetization in the FeMn/Cu heterostructures obtained after different cooling down procedures, as well as in different magnetic fields and temperatures.

III.2 Methods Used for Study of FeMn-based Multilayers

III.2.1 Growing of FeMn-based Films

Different sets of samples were prepared using two different magnetron systems: by the group of Prof. Casey W. Miller at the University of South Florida, and by myself at the Argonne National Laboratory. Special care was taken to ensure that nominally the same multilayers, but prepared using different vacuum deposition systems, had the same properties and demonstrated the same magnetic behavior.

All multilayers were deposited on top of Si/SiO2 substrates. DC and RF magnetron sputter deposition was used to prepare the samples. Prior to the deposition, the substrates were cleaned in acetone and ethanol/methanol using ultrasonic agitation. The following parameters were used for the deposition at the University of South Florida: base pressure was 1.8×10^{-8} Torr, the pressure during sputtering was 3 mTorr, Ta (DC-sputtering) growth rate was 0.76 Å/s; Cu (DC-sputtering) growth rate was 2.1 Å/s; and FeMn (RF-sputtering) growth rate was 0.47 Å/s. The following parameters were used for the deposition in the Argonne National Laboratory: the base pressure was 1×10^{-7} Torr, the sputtering pressure was 3 mTorr, Ta (DC-sputtering) growth rate was 1 Å/s; Cu (RF-sputtering) growth rate was 0.84 Å/s; and FeMn (DC-sputtering) growth rate was 0.12 Å/s.

For the magnetometry study three groups of samples were prepared. The first group consists of multilayer heterostructures Ta(5 nm)/[FeMn(t_{FeMn})/Cu(5 nm)]$_{10}$/Ta(5 nm). The second group is identical to the first one but has Ta instead of Cu, i.e., Ta(5 nm)/[FeMn(t_{FeMn})/Ta(5 nm)]$_{10}$/Ta(5 nm). The third group consists of two multilayers: Ta(5 nm)/[Cu(5 nm)/FeMn(5 nm)/Ta(5 nm)]$_{10}$/Ta(5 nm) and Ta(5 nm)/[Ta(5 nm)/FeMn(5

nm)/Cu(5 nm)]$_{10}$/Ta(5 nm). Additionally, Ta(5 nm)/FeMn(15 nm)/Ta(5 nm), Ta(5 nm)/FeMn(15 nm)/Cu(5 nm)/Ta(5 nm), and Ta(5 nm)/Cu(5 nm)FeMn(15 nm)/Cu(5 nm)/Ta(5 nm) films were prepared for Mössbauer and neutron reflectivity measurements. The choice of Cu and Ta for the study can be justified by the fact that these non-magnetic materials are traditionally used as seed layers because they have lattice parameters, a, similar to those of FeMn: a_{Cu} = 3.61 Å, a_{Ta} = 3.31 Å, and a_{FeMn} = 3.63 Å at room temperature.

Two groups of spin-valve heterostructures were prepared for the electronic-transport study. The first group consists of two valves: Ta(5 nm)/Cu(5 nm)/Py(2 nm)/Cu(5 nm)/FeMn(5 nm)/Cu(5 nm)/Ta(5 nm) (short Py/Cu/FeMn) and Ta(5 nm)/Cu(5 nm)/FeMn(5 nm)/Cu(5 nm)/Py(2 nm)/Cu(5 nm)/Ta(5 nm) (short FeMn/Cu/Py). The spin valves from the second group have structures identical to the structures of the AFSVs from the first group but the thickness of the FeMn layers for those valves is 15 nm.

III.2.2 Magnetometry measurements of low-magnetic-moment FeMn-based multilayers

Magnetometry measurements were conducted using Quantum Design SQUID VSM and SQUID MPMS magnetometers. Since there are no ferromagnetic materials in the films, the films' magnetic moment is expected to be low (of the order of 10^{-7}–10^{-6} emu/cm^2), hence, any magnetic contamination can significantly contribute to the measured signal and lead to a wrong data analysis. Special precautions during fabrication and measurements were taken to avoid any ferrous contamination of the films. Only non-magnetic, plastic, tweezers were used for handling the samples. For the SQUID-VSM-

magnetometer measurements, a quartz holder was utilized; the size of the samples was around 5 mm × 5 mm, and they were attached to the holder using a low-magnetic-susceptibility glue. For the SQUID-MPMS-magnetometer measurements, the size of a sample was chosen to fit tightly inside a plastic straw without an excessive deformation of it. No Kapton or Teflon tapes were used for fixing the samples.

III.2.3 Fabrication of microcantilevers for measuring thermally induced stress in FeMn-based films

The microcantilevers array for measuring a thermally induced stress in the FeMn-based films was fabricated using a photolithography-based 6-step process:

Step I) A clean Si/Si_3N_4(1000 nm) substrate was covered by S1813 positive photoresist and baked on a hot plate at 115 °C for 5 minutes. Then, the array of the inverse microcantilevers with dimensions 200 μm × 20 μm and 200 μm × 50 μm was patterned on the substrate using a laser-writer. The written pattern was developed by immersing the sample to the CD-26 developer and stirring gently for 40 sec.

Step II) The Ta(5 nm)/[FeMn(5 nm)/Cu(5 nm)]$_{10}$/Ta(5 nm) film was sputtered on top of the substrate with the developed pattern. After a lift-off in the acetone bath, the substrate contained an array of FeMn/Cu tongues attached to the substrate surface [Figure 3(b)].

To release the FeMn/Cu tongues for obtaining the suspended Si_3N_4(1000 nm)/Ta(5 nm)/[FeMn(5 nm)/Cu(5 nm)]$_{10}$/Ta(5 nm) cantilevers, Si_3N_4 around the tongues and Si underneath the tongues must be etched.

Step III) To protect the film while etching an S1813-photoresist mask was patterned on top of the film using the same lithography procedure as in the step I.

Step IV) Si_3N_4 around the tongues was removed using reactive-ion etching with CF4.

Step V) Si beneath the tongues was removed using XeF_2 dry-etching. The process was monitored using an optical microscope. The etching was stopped when all the cantilevers became completely suspended. Since the XeF2 etching is isotropic, the depth of the holes under the cantilevers is comparable to their width (100 μm) [Figure 3(c)].

Step VI) The photoresist mask used to protect the film while etching was removed by keeping the sample in the acetone bath for 24 hours. No ultrasonic cleaning was performed.

III.2.4 Measurements of cantilever bending at different temperatures

To measure the bending of cantilevers at different temperatures, the sample with cantilevers was glued to a small copper edge, which was installed on a cold finger of a probe station [Figure 3(a)]. Deflection of the cantilevers at different temperatures was observed through a glass window in the vacuum chamber using a microscope. Based on the deflection, the internal stress in the film can be estimated.

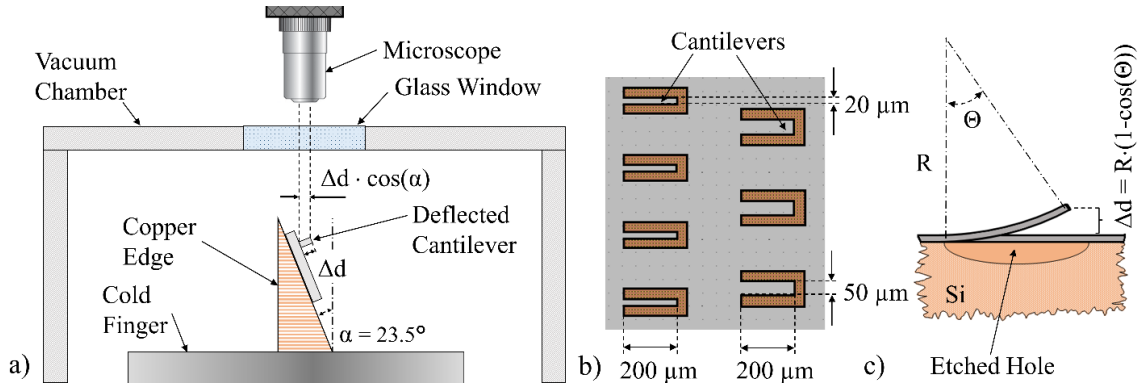

Figure 3 (a) Schematic of the experimental set-up used for measuring the bending of Si_3N_4/Ta(5 nm)/[FeMn(5 nm)/Ta(5 nm)]$_{10}$/Ta(5 nm) microcantilever at temperatures within a 8–400 K range. (b) Design of the cantilevers. (c) Cross section of the sample with the cantilever deflected by Δd from the sample surface (R is the curvature radius).

III.3 Characterization of FeMn-based Films Using X-ray Diffraction

X-ray diffraction (XRD) measurements were conducted for characterization of the Ta(5 nm)/[FeMn(5 nm)/Ta(5 nm)]$_{10}$/Ta(5 nm) [Figure 4(a)] and Ta(5 nm)/[FeMn(5 nm)/Cu(5 nm)]$_{10}$/Ta(5 nm) [Figure 4(b)] films. The peaks at $2\Theta = 69^\circ$ and $2\Theta = 30^\circ$ in both spectra are due to Si(400) and Si(211) reflections, respectively.[58] Further analysis shows that Ta(5 nm)/[FeMn(5 nm)/Cu(5 nm)]$_{10}$/Ta(5 nm) [Figure 4(b)] film is polycrystalline and the peak observed at 43º is due to a (111)-texture in the FeMn and Cu lattices in the direction perpendicular to the film surface.[59] The structure of this peak suggests two possible scenarios of FeMn and Cu growth in this film. First, since the lattice parameter of FeMn and Cu are similar (a_{Cu} = 3.61 Å, a_{Ta} = 3.31 Å, a_{FeMn} = 3.63 Å) and the texture is not perfect, the structural quality of the FeMn and Cu (111)-peaks is low and they overlap with each other providing a combined broad peak. The other possibility is that the 5-nm-thick FeMn and Cu layers grow coherently on top of each other. Under this condition, the lattice expansion/contraction would make the net lattice parameter identical

for both materials, which again would yield a single peak in the XRD spectrum. The surface reconstruction of the lattice at the FeMn/Cu interfaces would explain the broadening of this common peak. Since the peak at 43º looks very symmetric [Figure 4(b) inset], the latter scenario is more plausible.

The spectrum for the Ta(5 nm)/[FeMn(5 nm)/Ta(5 nm)]$_{10}$/Ta(5 nm) film looks very different from that for the Ta(5 nm)/[FeMn(5 nm)/Cu(5 nm)]$_{10}$/Ta(5 nm) film. There is no (111) peak of FeMn at 43º, instead, a significant reflection in the 32º–45º range is observed. It is not clear what produces this increase in the scattering. First, small crystallite grains and non-uniform lattice distortion can cause a modest broadening of an XRD peak.[60] However, it is very unlikely that these phenomena can lead to such a broad peak as observed for the FeMn/Ta multilayer. Second, it is possible that the crystalline structures of the FeMn and Ta layers vary along the thickness of the film. However, there are no reasons which can justify such a significant change in the lattice parameters for FeMn and Ta. Most probably, Ta and FeMn are amorphous in the FeMn/Ta multilayer. Further analysis needs to be conducted to characterize the FeMn/Ta multilayers. Importantly, the (111) texture of FeMn is probably not realized in these multilayers. Lance Ritchie and *et al.*[61] showed that bilayers composed of FeMn and permalloy (Py) demonstrate the strongest EB effect when FeMn has the (111) texture. Namely, even for a classical AF/F exchange bias system, there is correlation between the atomic structure of FeMn and EB.

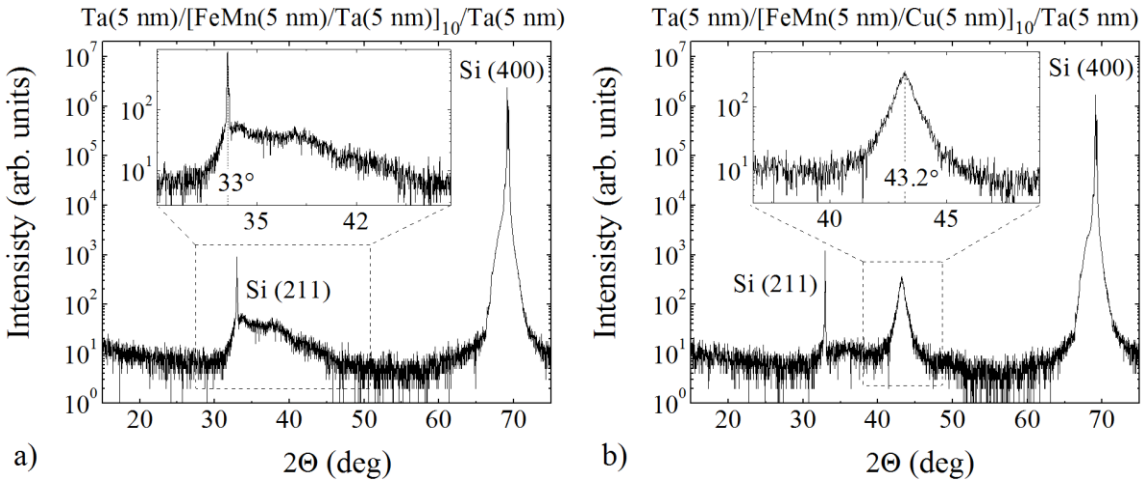

Figure 4 X-ray diffraction spectra for the (a) Ta(5 nm)/[FeMn(5 nm)/Ta(5 nm)]$_{10}$/Ta(5 nm) and (b) Ta(5 nm)/[FeMn(5 nm)/Cu(5 nm)]$_{10}$/Ta(5 nm) films.

III.4 Magnetometry Study of FeMn-based Heterostructures. Characterization of EB in FeMn/Cu Multilayers

At the first stage of the project, magnetometry was used to study magnetic behavior of the FeMn-based films. A part of the magnetometry data were obtained in collaboration with Dogan Kaya.[62] The idea was to measure an uncompensated magnetization of the FeMn and to see how this magnetization is affected by the thickness of the layer and proximity with diamagnetic Cu and Ta. It was expected that a 5-nm-thick FeMn layer has a very low magnetization, around 10^{-7} emu/cm^3. To maximize the magnetic moment and thus increase accuracy of the measurements, the stacks consisting of 10 repeats of FeMn and, Ta or Cu, were prepared for the study.

The hysteresis loops for the Ta(5 nm)/[FeMn(5 nm)/Ta(5 nm)]$_{10}$/Ta(5 nm) and Ta(5 nm)/[FeMn(5 nm)/Cu(5 nm)]$_{10}$/Ta(5 nm) films after subtraction of the diamagnetic response produced by the substrates are shown in Figure 5(a and b), respectively. The

magnetic moments per unit area were measured at 10 K after the films were cooled down in a 70-kOe magnetic field from 300 K. Since the multilayers do not contain any other magnetic materials, only the antiferromagnetic response produced by the FeMn was expected. However, one can see that the magnetization of these multilayers rises non-linearly with the field and the loops demonstrates hysteretic behavior. The remanent magnetizations and coercivity fields for these multilayers are nonzero. Moreover, the loop for the FeMn/Cu multilayer demonstrates about a 1-kOe EB shift after the field cooling, while no EB shift is observed for the multilayers with Ta.

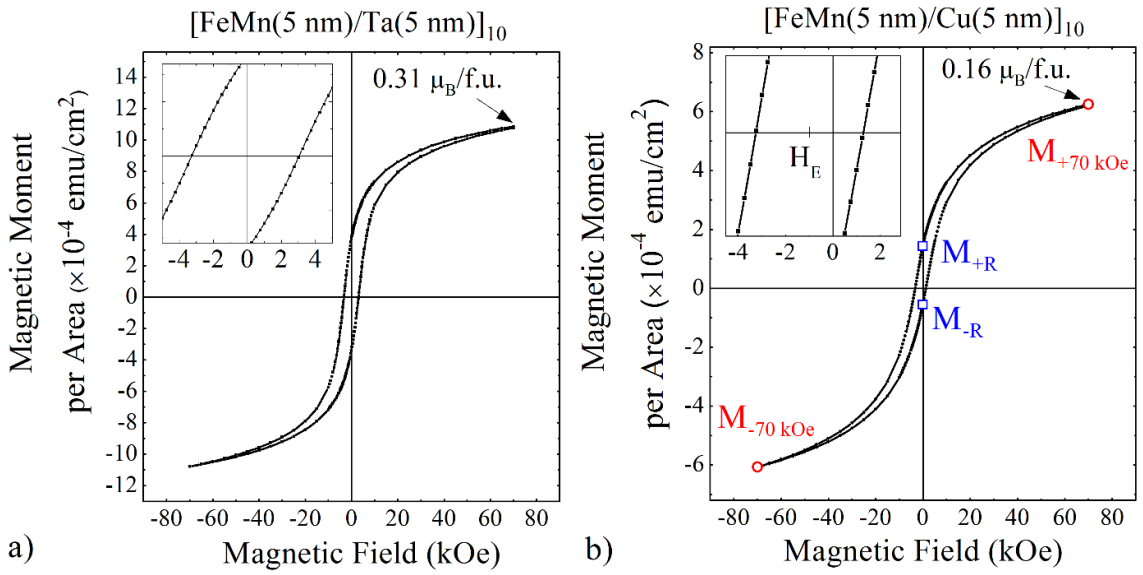

Figure 5 Hysteresis loops measured at 10 K for the (a) Ta(5 nm)/[FeMn(5 nm)/Ta(5 nm)]$_{10}$/Ta(5 nm) and (b) Ta(5 nm)/[FeMn(5 nm)/Cu(5 nm)]$_{10}$/Ta(5 nm)[62, 63] films after a 70-kOe-magnetic-field cooling from 300 K. Magnetic field was applied in plane. The insets show the central parts of the loops. Magnetic moments at 70-kOe magnetic field are shown in Bohr magneton per formula unit. (After Ref. [62, 63])

All the FeMn/Cu and FeMn/Ta multilayers demonstrate a significant magnetization although they do not contain explicit ferromagnetic layers. We attribute this

magnetization to a combination of two contributions. The first contribution is a paramagnetic-like magnetization provided by the AF ordered FeMn. The second contribution is due to an uncompensated, ferromagnetic-like, magnetization in FeMn. To disentangle these contributions the hysteresis loops were measured at 10 K after a 70-kOe-field cooling from 400 K. Then, two parameters of the hysteresis loops, the absolute value of the magnetic moment per unit area at a 70-kOe and -70-kOe magnetic fields, *i.e.*, $M_{<70\ kOe>} = (M_{70\ kOe} + | M_{-70\ kOe} |)/2$, and the absolute value of the unpinned remanent magnetic moment per unit area, *i.e.*, $M_{<R>} = (M_R + | M_{-R} |)/2$, [Figure 5(b)] were plotted as functions of the FeMn layers thickness, t_{FeMn} (Figure 6). To a first approximation, $M_{<70\ kOe>}$ is a sum of the AF and ferromagnetic-like magnetizations, while $M_{<R>}$ is proportional only to the ferromagnetic-like magnetization. Both $M_{<R>}$ and $M_{<70\ kOe>}$ monotonically increase with increasing t_{FeMn}. Almost a linear scaling with t_{FeMn} suggests that both AF and ferromagnetic-like magnetizations are almost proportional to the thickness of the FeMn layers. Hence, it is possible to conclude that the unpinned uncompensated magnetization is distributed homogeneously within the FeMn layers.

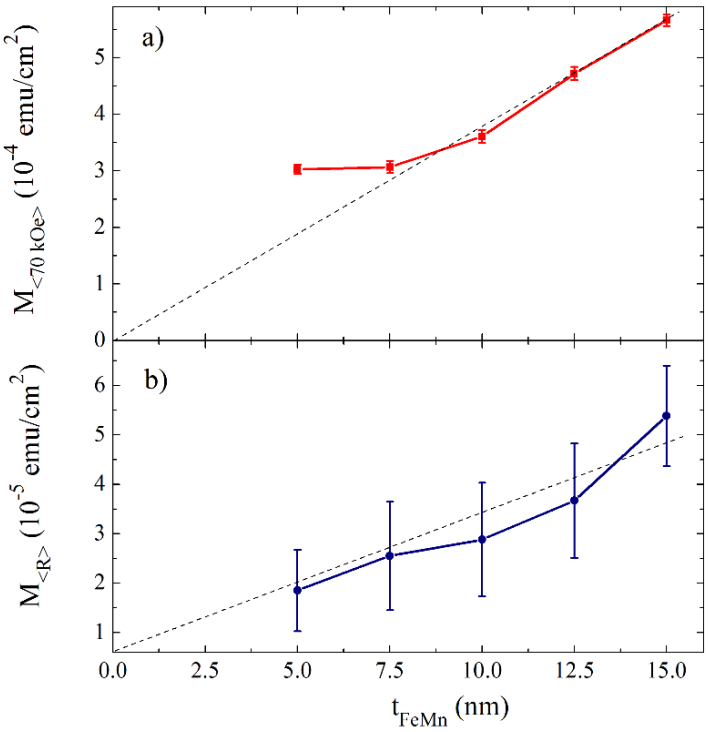

Figure 6 (a) The absolute value of the unpinned magnetic moment per unit area at 70-kOe and -70-kOe magnetic fields, *i.e.*, $M_{<70\ kOe>}=(\ M_{70\ kOe}+|\ M_{-70\ kOe}\ |)/2$, and (b) the absolute value of the remanent unpinned magnetic moment per unit area, *i.e.*, $M_{<R>} = (M_R + |M_{-R}|)/2$ as functions of the FeMn-layer thickness (t_{FeMn}) for the Ta(5 nm)/[FeMn(t_{FeMn})/Cu(5 nm)]$_{10}$/Ta(5 nm) films.[62] The dashed lines are linear fits. The hysteresis loops were measured at 10 K after a 70-kOe-field cooling from 400 K. (After Ref. [62])

To analyze the behavior of the pinned uncompensated magnetization, dependences of the absolute value of H_E, $|H_E|$, (black line/dots) and H_C (red line/dots) on the FeMn-layer thickness (t_{FeMn}) were obtained from the hysteresis loops [Figure 7(a)]. The H_C (t_{FeMn}) dependence does not demonstrate any interesting trend. H_E decreases with increasing the FeMn-layers thickness, and to a first approximation, scales almost inversely proportional to t_{FeMn} [Figure 7(b)]. For various proximity-effect systems, scaling with inverse thickness is an indication that the proximity effect is driven by the interface. For example, in a classical EB system composed of the F and AF layers, the EB field is inversely

proportional to the thickness of the F layer [Equation (III-2) and (III-3)]. For the FeMn/Cu system, the unpinned uncompensated magnetization that plays a role of the ferromagnet is uniformly distributed within the FeMn layer. Hence, it means that the pinned magnetization must be located at the interface between the FeMn and Cu layers.

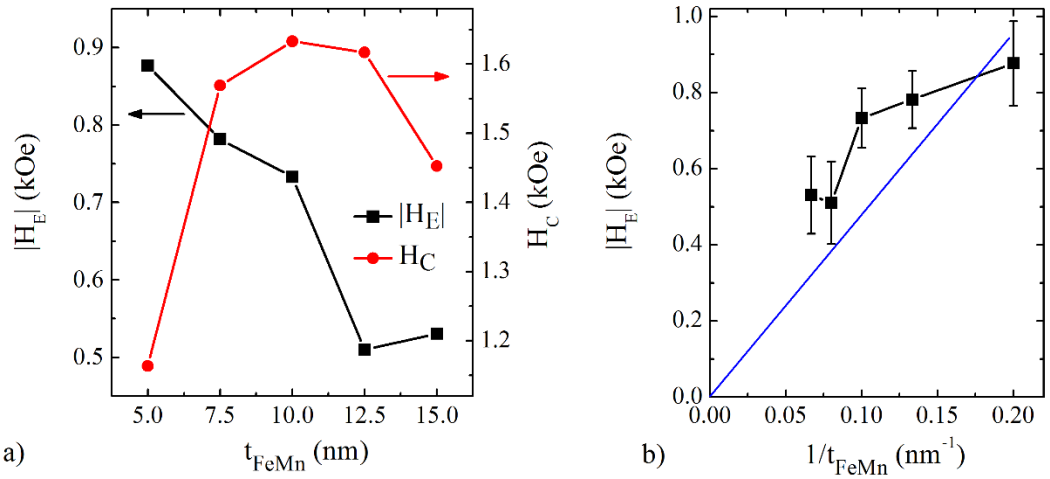

Figure 7 (a) The absolute value of the EB field, $|H_E|$, (black line/squares) and coercive field, H_C, (red line/dots) as functions of the FeMn-layer thickness (t_{FeMn}) for the Ta(5 nm)/[FeMn(t_{FeMn})/Cu(5 nm)]$_{10}$/Ta(5 nm) films. The 70 kOe hysteresis loops were measured at 10 K after a 70-kOe field cooling from 400 K. (b) $|H_E|$ as a function of inverse thickness of the FeMn layers ($1/t_{FeMn}$) (black line/squares), linear fit of the $|H_E|$ ($1/t_F$) dependence (blue line). (After Ref. [62])

To understand how parameters of the Ta(5 nm)/[FeMn(5 nm)/Cu(5 nm)]$_{10}$/Ta(5 nm) film change with temperature, a series of 70-kOe hysteresis loops was measured at different temperatures after the film was cooled down in a 70-kOe magnetic field from 300 K. The temperature dependences of $|H_E|$, H_C are shown in Figure 8(a). As one can see, $|H_E|$ grows monotonically upon decreasing temperature from 200 to 50 K, whereas the coercivity remains almost constant in this temperature region. Below 50 K, both $|H_E|$ and

H_C experiences significant growth. Data in Figure 6 and Figure 7 were measured in collaboration with Dogan Kaya.

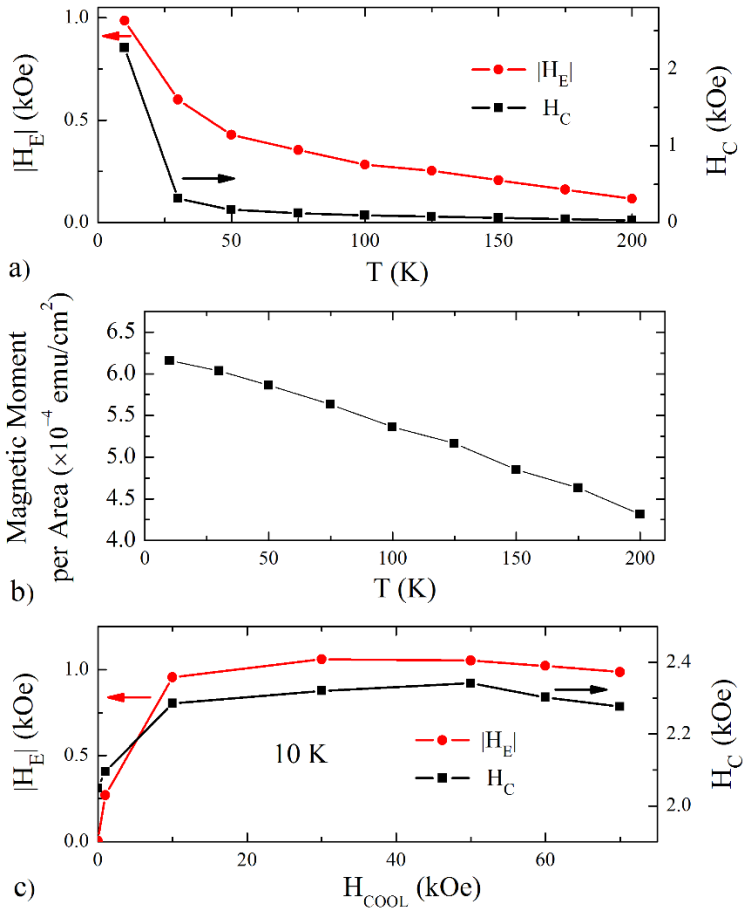

Figure 8 (a) Temperature dependences of $|H_E|$ and H_C for the Ta(5 nm)/[FeMn(5 nm)/Cu(5 nm)]$_{10}$/Ta(5 nm) film. (After Ref. [62]) (b) The temperature dependence of the magnetic moment per area for the Ta(5 nm)/[FeMn(5 nm)/Cu(5 nm)]$_{10}$/Ta(5 nm) film measured in the 70-kOe magnetic field. (c) $|H_E|$ and H_C as functions of a cooling field amplitude for the Ta(5 nm)/[FeMn(5 nm)/Cu(5 nm)]$_{10}$/Ta(5 nm) film. To define H_E and H_C the 70-kOe hysteresis loops were measured at 10 K after cooling in H_{COOL} field from 300 K.

Simultaneous change in H_E and H_C can signify that either the pinning of the uncompensated moments at the interface or the coupling of the uncompensated moment within the FeMn layer increase at low temperatures. The latter possibility is less plausible

since the same measurements show that magnetization of the FeMn/Cu films rises monotonically upon decreasing the temperature from 300 K to 10 K [Figure 8(b)], thus indicating the magnetic order does not change drastically below 50 K. Figure 8(a) shows the behavior of the EB field only below 200 K. However, a significant EB shift of the loop was observed even at room temperature if the film is cooled down from 400 K. This observation signifies that a long-range AF order exists in the FeMn layers even at room temperature.

Figure 8(c) shows the dependences of H_E and H_C on the cooling-field amplitude, H_{COOL}, for the Ta(5 nm)/[FeMn(5 nm)/Cu(5 nm)]$_{10}$/Ta(5 nm) film. The data were obtained based on the analysis of 70-kOe magnetization curves measured at 10 K after the film was cooled down in H_{COOL} field from 300 K. H_E and H_C rise with increasing H_{COOL} until H_{COOL} reaches 10 kOe, after that H_E and H_C are almost constant. This behavior can be an indication that the ferromagnetic-like component of the magnetization is saturated by the 10-kOe magnetic field.

In summary, the magnetometry measurements showed that, in the FeMn/Cu and FeMn/Ta multilayers, the nominally AF FeMn layer has a significant uncompensated magnetization. Analysis of the hysteresis loops for the FeMn/Cu multilayers with different thicknesses of the FeMn layer suggests that the unpinned uncompensated magnetization is uniformly distributed within the depth of the FeMn layers, whereas the pinned magnetization is located at the interface between the FeMn and Cu layers.

III.5 Mössbauer Spectroscopy of Ta/FeMn/Ta and Ta/FeMn/Cu Films

The magnetometry measurements revealed that unpinned uncompensated magnetization is uniformly distributed within the FeMn layers. What is the origin of this uncompensated magnetization? First, the uncompensated magnetization inside FeMn can appear due to a chemical disorder with respect to Fe and Mn positions. Thus, a local redistribution of Fe and Mn or their loss is responsible for the uncompensated moments in the FeMn lattice. Second, for the sample with Cu, yet another scenario is possible. Namely, Cu can diffuse into the FeMn alloying with Mn. This would lead to an excess of Fe clusters in FeMn layers and the appearance of the uncompensated magnetization. This scenario is not relevant to the FeMn/Ta multilayer because it is known that Ta does not easily alloy with other metals. To find out which of these two mechanisms is realized, the chemical environment of Fe nuclei was analyzed by means of Mössbauer spectroscopy. This experimental technique is an extremely sensitive tool for studying local environment of nuclei. One of its main benefits is its sensitivity to a slightly different local electron density caused by chemical inhomogeneity.

The conversion electron Mössbauer spectra for the Ta(5 nm)/FeMn(15 nm)/Ta(5 nm) and Ta(5 nm)/FeMn(15 nm)/Cu(5 nm)/Ta(5 nm) films were collected at the University of Manitoba. The measurement was performed at room temperature using a WissEl constant acceleration spectrometer with a 10-GBq CoRh-57 source. Fe-57 was used as a probe isotope and a line shift is reported relative to its absorption peak.

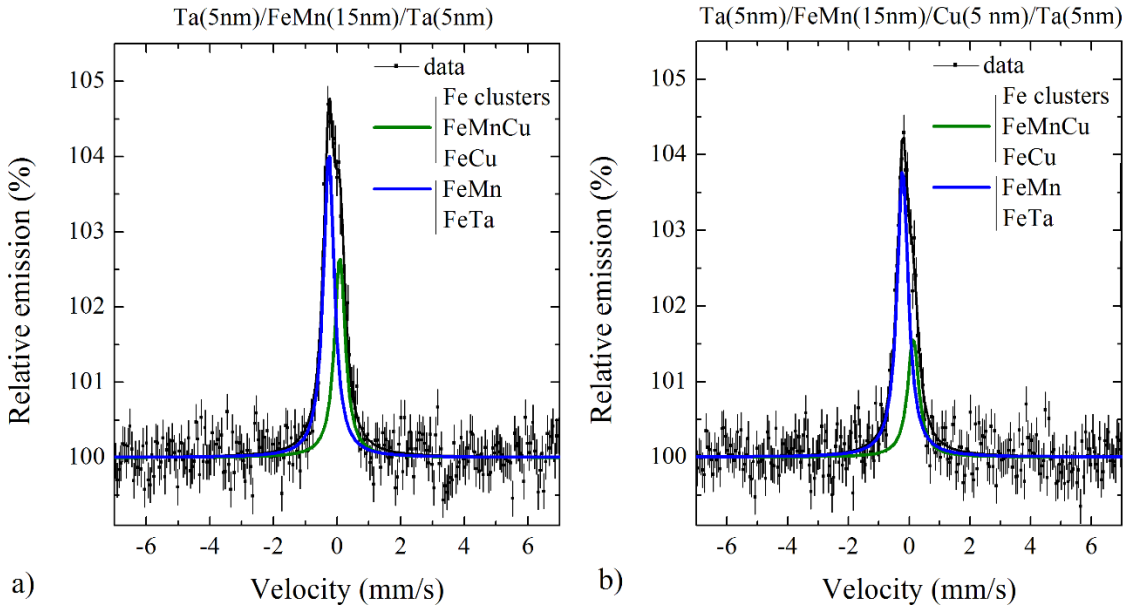

Figure 9 Mössbauer spectra for (a) Ta(5 nm)/FeMn(15 nm)/Ta(5 nm), and (b) Ta(5 nm)/FeMn(15 nm)/Cu(5 nm)/Ta(5 nm) films.

For both samples, Mössbauer spectra have wide asymmetric peaks at zero velocities (Figure 9). The analysis showed that the spectra can be fitted as a convolution of two singlet peaks with different isomer shifts. The shift of the major singlet peak is corresponding to Fe nuclei in FeMn[64, 65] or FeTa[65] alloys. The small, positively shifted peak is consistent with Fe nuclei in Fe clusters[66] or FeMnCu,[67] FeCu[68] alloys. The fact that the positively shifted peak is inherent for both samples, with and without Cu, indicates that alloying with Cu is unlikely. Hence, formation of the Fe clusters is most likely related to the defects in the FeMn lattice. The Fe clusters have a non-zero magnetic moment and they are responsible for the uncompensated magnetization of the FeMn layers. Analysis of the hysteresis curves (Figure 5) showed that only 2% of Fe atoms need to be involved in the clusters formation to provide the amount of the ferromagnet-like signal presented for the FeMn-based multilayers (of the order of 10^{-5} emu). At the same time, fitting of

Mössbauer spectra shows that up to 40% of Fe atoms in FeMn are involved in the formation of the Fe clusters. This indicates that only a small fraction of the Fe clusters is ferromagnetic.

III.6 X-ray and Polarized Neutron Reflectometry Study

III.6.1 Experimental reflectivity data for FeMn-based films

In order to investigate the uncompensated magnetization and its relation to the chemical inhomogeneity in the FeMn layers, Ta(5 nm)/Cu(5 nm)/FeMn(15 nm)/Cu(5 nm)/Ta(5 nm) and Ta(5 nm)/FeMn(15 nm)/Ta(5 nm) films were studied using x-ray reflectometry (XRR) and neutron reflectometry (NR).[69]

Polarized neutron reflectometry (PNR) is as a very sensitive nondestructive tool for determining a magnetization profile in the EB heterostructures.[11-13] For the FeMn-based films, it was expected that the uncompensated magnetization inside the FeMn layer is high enough to cause the neutrons with different polarizations (spin-up and spin-down) to be scattered differently on this uncompensated magnetization. The difference in spin-up and spin-down scattering length profiles should have allowed reproducing the magnetic profiles in the FeMn-based films. Thus, it was expected that the distribution of magnetization over the multilayer would be determined using PNR and compared to the distribution proposed based on the magnetometry results.

Aside from the determination of the magnetic profiles with PNR, there is another benefit of using the NR for study of the FeMn-based heterostructures. Namely, both NR and XRR are capable conveying the information on the chemical structure in the heterostructures, however, these techniques can complement each other. A traditional

XRR is a powerful tool for studying atomic structure of multilayers and it is sensitive to a local electronic density. In the case of Fe and Mn, the local electronic densities almost coincide, which means that the XRR cannot distinguish between Fe and Mn, and hence, detect a chemical phase separation in the FeMn layer. In contrast, the NR is based on neutrons' interaction with the nuclei. Nuclear scattering cross-sections are different for Fe and Mn, which provides a distinct difference in scattering on Fe and Mn lattices. This is very valuable for studying the structural profile of the FeMn-based films.

The following procedure was used for the PNR measurements. The samples were cooled down in an 11.5-kOe in-plane magnetic field from room temperature to 5 K. Then, to eliminate the possibility of changing magnetization due to any training effects, the magnetic field was swept 3 times between 11.5 and -11.5 kOe. After that, the signals from the spin-up and spin-down channels were measured in 11.5 and -11.5 kOe. It was expected that the unpinned uncompensated magnetization follows the direction of the magnetic field, hence, this magnetization affects equally the spin-up and spin-down reflectivity curves measured at 1.15 and -1.15 T fields. For the pinned magnetization, this is not the case and this leads to the difference of the reflectivity curves measured in 11.5 and -11.5 kOe. Analyzing this difference should have enabled reproducing the pinned magnetization profile.

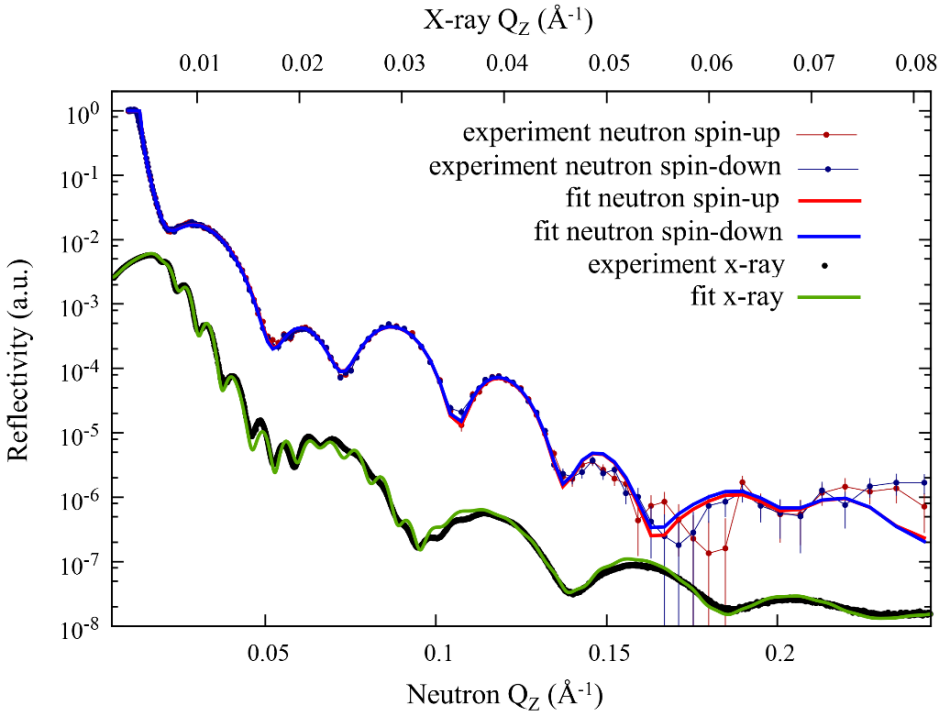

Figure 10 Polarized neutron reflectivity and x-ray reflectivity as functions of wave vector transfer perpendicular to the surface, Q_Z, for the Ta(5 nm)/Cu(5 nm)/FeMn(15 nm)/Cu(5 nm)/Ta(5 nm) film. Neutron spin-up experimental data – maroon dots/thin line, spin-up fit – thick red line, neutron spin-down experimental data – blue dots/thin line, spin-down fit – thick blue line, x-ray experimental data – black dots, x-ray fit red line – green line. The bottom scale shows Q_Z for the neutron beam, the top scale shows Q_Z for the x-ray beam.

Figure 10 shows the PNR and XRR spectra for the Ta(5 nm)/Cu(5 nm)/FeMn(15 nm)/Cu(5 nm)/Ta(5 nm) film. Although the signal from both neutron polarizations is high and the noise becomes considerable only at high wave vector transfers (Q_z is a component of wave vector transfer perpendicular to the film surface), the difference between the spin-up and spin-down PNR curves is very small. This is because the uncompensated magnetization is very low. Fitting the resulting spin-asymmetry allows obtaining a magnetic component of the scattering length density (SLD) and thus evaluating the profile

of the magnetization in the film [red curves Figure 11(a), the right scale bar]. This procedure allowed us to estimate the magnetization of the FeMn layer to be about 5 emu/cm^3. This is comparable to the magnetization of the FeMn/Cu multilayers measured with magnetometry. Unfortunately, because this magnetization is so low, it is impossible to reliably determine the uncompensated magnetization depth profile.

Simultaneous fitting of the NR and XRR spectra provided structural components of the SLD for the Ta(5 nm)/Cu(5 nm)/FeMn(15 nm)/Cu(5 nm)/Ta(5 nm) [Figure 11(a)] and Ta(5 nm)/FeMn(15 nm)/Ta(5 nm) [Figure 11(b)] films. For both films, the XRR SLD profiles are almost symmetric with respect to the middle of the FeMn layer, except for the upper Ta layers, whose SLD are insignificantly smeared due to an accumulated roughness and oxidation. In contrast, the PNR SLD profiles look very asymmetric. Importantly, for the Ta/Cu/FeMn/Cu/Ta film [Figure 11(a)], there is a significant dip inside the FeMn layer by the interface with the lower Cu layer. For the Ta/FeMn/Ta film, there is a similar dip in the FeMn layer near the interface with the upper Ta layer [Figure 11(b)], but its depth is much smaller than that in the case of the film with Cu. This feature is very robust for the Ta/Cu/FeMn/Cu/Ta film. Several different models with different parameters (roughness, thickness) were used to fit these SLDs, and all of them yielded the deep dip in the FeMn layer of the film with Cu. This suppression of the SLD in the FeMn layer is attributed to a Mn-rich portion of FeMn near the bottom Cu layer.

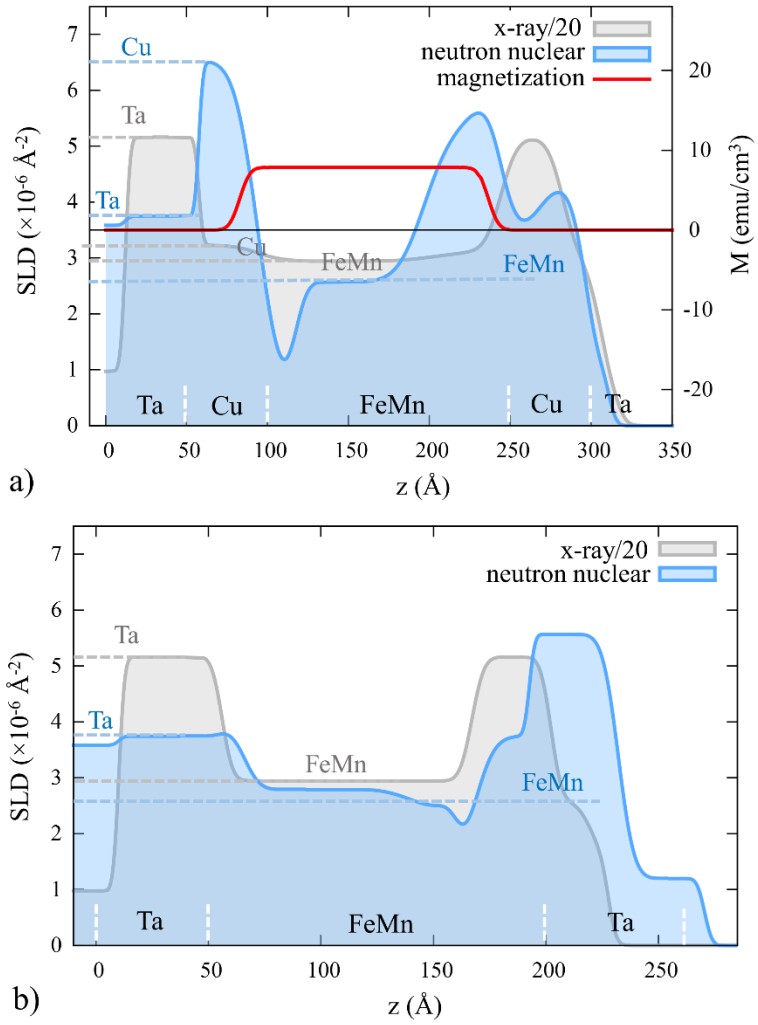

Figure 11 XRR and PNR SLD depth profiles for (a) Ta(5 nm)/Cu(5 nm)/FeMn(15 nm)/Cu(5 nm)/Ta(5 nm) and (b) Ta(5 nm)/FeMn(15 nm)/Ta(5 nm) samples. The interface between the substrate (Si/SiO_2) and the films at $z = 0$. The nominal values of SLD for the material composing the film are shown with dashed horizontal lines. The nominal thicknesses of the layers are shown above the horizontal scale bar. (After Ref. [69])

III.6.2 Discussion of reflectivity data for FeMn-based films

The structural analysis demonstrates that due to the Mn-rich region, the top and the bottom interfaces of FeMn with Cu are not identical in the Ta/Cu/FeMn/Cu/Ta structure. Redistribution of Mn can lead to inhomogeneity of the magnetic state in FeMn.

In principle, a part of FeMn layer with increased Mn content can be antiferromagnetic, while the other part with increased Fe content can exhibit a weak ferromagnetic or ferrimagnetic magnetization. The coexistence of ferromagnetic and antiferromagnetic regions in the FeMn layer can be the reason for the observable exchange bias in FeMn/Cu heterostructures.

Another scenario of magnetization pinning may be realized due to the Mn-rich area by the interface with the bottom Cu. Namely, Mn can diffuse into Cu.[70] This leads to a formation of a CuMn alloy which is a spin glass material.[71] Similarly to spin glass model of the EB described above, a part of Mn spins in the interfacial CuMn alloy freezes at low temperatures and does not respond to the external magnetic field. Unpinned moments in FeMn are exchange coupled to frozen spins at the interface which provides unidirectional anisotropy and EB effect. A recent study of magnetic behavior in a spin glass ($Cu_{1-x}Mn_x$)/ ferromagnet (Co) system[50] showed that the system exhibits the same spectrum of phenomena as classical antiferromagnet/ferromagnet exchange bias systems (loop shift, increasing coercivity and training effect). Thus, the spins frustration at the interface with the bottom Cu and FeMn may give rise to the pinning. However, for the $Cu_{1-x}Mn_x$ alloys, the spin glass state is observed only when $x > 0.7$.[72, 73] The freezing temperature of the spin glass is below 170 K for all $x > 0.7$. First, the EB is observed even at room temperature in the FeMn/Cu multilayers. Second, based on the PNR SLD depth profiles for the Ta(5 nm)/Cu(5 nm)/FeMn(15 nm)/Cu(5 nm)/Ta(5 nm) film [Figure 11(b)], the spin-glass $Cu_{1-x}Mn_x$ alloy ($0.7 < x < 1$) may form only in a thin layer between FeMn and Cu. However, this layer would consist only of a few atomic monolayers of material. This

makes it unlikely that the pinning would be sufficiently strong to provide the observable EB effect. Thus, it can be concluded that although the spin-glass scenario of the pinning may take place, it is doubtful that it plays the dominant role in the EB effect observed in the FeMn/Cu multilayers.

III.7 Magnetometry Measurements of Ta/FeMn/Cu and Cu/FeMn/Ta Multilayers

To check if the chemical separation in the FeMn layer observed with the NR influences its magnetic properties, two multilayers were fabricated: Ta(5 nm)/[Ta(5 nm)/FeMn(5 nm)/Cu(5 nm)]$_{10}$/Ta(5 nm) and Ta(5 nm)/[Cu(5 nm)/FeMn(5 nm)/Ta(5 nm)]$_{10}$/Ta(5 nm). These multilayers were cooled down in a 70-kOe magnetic field from 300 K to 10 K and their hysteresis loops were measured at 10 K (Figure 12). The results of these measurements are quite surprising. First, the Cu/FeMn/Ta multilayer demonstrates the EB effect (H_E = -500 Oe), while the Ta/FeMn/Cu multilayer does not. This suggests that the pinning occurs only at the interface with the bottom Cu layer. Moreover, since the magnetometry measurement of the FeMn/Cu multilayers showed that the pinned moments must be localized near the interface to provide the observed scaling of H_E with the thickness of FeMn layers, the pinned magnetization may be directly related to the Mn-rich portion of FeMn revealed by the NR measurements. No pinning occurs if the Cu layer is on top of the FeMn.

The second unexpected result of these measurements is that the magnetization of the Ta/FeMn/Cu multilayer is almost twenty times lower than that for the Cu/FeMn/Ta multilayer. It is not clear which microscopic mechanism is responsible for the

uncompensated magnetization. As it was mentioned previously, alloying Cu with Fe or Mn can lead to the uncompensated moments in FeMn. Again, the magnetometry of the FeMn/Cu multilayers suggests that these magnetic moments must be distributed more or less homogeneously within the FeMn layer. It is reasonable to assume that either Cu diffuses deep inside into the FeMn layer through its intergrain boundaries, or the Cu layer modifies the crystal structure of FeMn, for example, stretching or compressing it. This would have led to an imbalance between different AF sublattices and an appearance of the uncompensated magnetization. Then, it is not clear why the FeMn/Ta multilayer demonstrates a significant uncompensated magnetization even though it does not contain any Cu layer. Further analysis is needed to understand how the underlayer and overlayer affects the atomic and magnetic properties of FeMn.

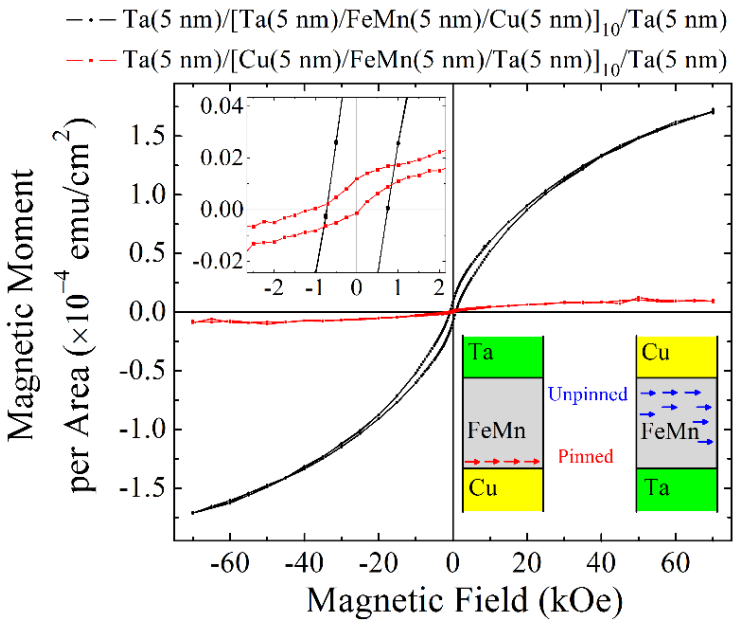

Figure 12 Magnetization curves for the Ta(5 nm)/[Ta(5 nm)/FeMn(5 nm)/Cu(5 nm)]$_{10}$/Ta(5 nm) film (black dots/line) and the Ta(5 nm)/[Cu(5 nm)/FeMn(5 nm)/Ta(5 nm)]$_{10}$/Ta(5 nm) film (red squares/line) measured at 10 K after the films were cooled down from 300 K in the 70-kOe magnetic field.

III.8 FeMn-based Antiferromagnetic-Ferromagnetic Spin Valves

III.8.1 Design of spin valves for probing pinned uncompensated magnetization

For a classical AF/F EB system, the pinned uncompensated magnetization is low compared to the magnetization of the F layer. For example, H. Ohldag and *et al.*[74] used x-ray magnetic circular dichroism for investigating the EB effect in NiO/Co, IrMn/Co, and PtMn/CoFe bilayers and showed that the pinned uncompensated moments are a small fraction of the interfacial monolayer (about 4%).

Presumably, since the FeMn-based multilayers do not have explicit F layers, the pinned magnetization must compose a substantial part of its total magnetization. One might assume that the value of the pinned magnetization in the FeMn-based EB system can be estimated based on the vertical shift of its hysteresis loops. Unfortunately, even without regards to the pinned magnetization, the horizontal shift of the hysteresis loop is always accompanied by the vertical shift. It is impossible to resolve the contribution to the vertical shift caused by the pinned magnetization from that due to the effective unidirectional anisotropy without making additional assumptions on the pinning.[75-78] Hence, classical magnetometry measurements do not allow to determine the pinned uncompensated magnetization in the non-classical FeMn EB system. Also, we were unable to measure the depth profile of the pinned uncompensated magnetization using the PNR measurements. The question arises: is it possible to use any other technique which is complimentary to the magnetometry, for example transport measurements, to determine the location of the pinned moments?

Heterostructures composed of two F layers separated by a conducting buffer, so-called "spin valves", are widely used in various scientific studies and technological applications. Due to spin-dependent scattering, the resistance of the spin valves depends on the relative orientation of the magnetizations in the F layers; this is a so-called "giant magnetoresistance" (GMR) effect. The resistance is high when the magnetizations are antiparallel to each other and low when they are parallel. In a classical GMR spin valve, one of the F layers is in proximity to an AF. Due to the EB effect, the direction of the magnetization in this F layer changes insignificantly until the external field exceeds the EB field for the AF/F bilayer. The external magnetic field changes the direction of the other, "free", F layer which yields a change in resistance.

To study the pinned uncompensated magnetization in FeMn, we fabricated a spin valve that consists of the F (Py) and AF (FeMn) layers separated by a thin conducting buffer (Cu), a so-called "antiferromagnet-ferromagnet spin valve" (AFSV). Py stands for permalloy with the $Ni_{0.81}Fe_{0.19}$ composition. After the AFSV is cooled down in a magnetic field, the pinned uncompensated magnetization in the FeMn layer plays the role of the fixed ferromagnetic layer of a classical GMR spin valve. Similarly to a classical GMR spin valve, the resistance of the AFSV depends on the relative magnetizations in the F layer and the pinned/unpinned magnetization in the AF. It was expected that the measurements of the angular dependences of the AFSV resistance in different magnetic fields would allow analyzing the orientation and magnitude of the pinned uncompensated magnetization.

III.8.2 Py/Cu/FeMn antiferromagnet-ferromagnet spin valve

For the first test, the Ta(5 nm)/Cu(5 nm)/Py(2 nm)/Cu(5 nm)/FeMn(5 nm)/Cu(5 nm)/Ta(5 nm) AFSV [Figure 13(d)] was cooled down in a 70-kOe magnetic field from 300 K to 10 K applied along the long edge of the stripe (Θ_{COOL} = 0º). The angular dependences of the resistance, *R*, for the AFSV measured in 200-Oe (green line/open dots) and 70-kOe (black line/solid dots) magnetic fields are shown in Figure 13(a). The curves demonstrate that the AFSV resistance has a sinusoidal dependence on the angle of rotation, Θ. For both curves, *R* has local maxima at 0º and 180º. At 180º, the pinned uncompensated magnetization in FeMn is opposite to the magnetization in the Py layer, while they have the same orientation at 0º. Since the electrons polarized by Py scatter on the pinned uncompensated magnetization in the FeMn layer [Figure 13(e)], the resistance at 0º is lower than the resistance at 180º. In general, the angle-dependent part of the $R(\Theta)$ curves measured in the 200-Oe and 70-kOe magnetic fields can be represented as a combination of two harmonic components: R_1-$R_2\cos(\Theta)$ and R_3-$R_4\cos(2\Theta)$, where R_3, R_4, R_3, R_4 are fitting parameters. The first component, proportional to $\cos(\Theta)$, is due to the anisotropic magnetoresistance of Py,[79] while the second component, proportional to the $\cos(2\Theta)$, is due to the GMR effect related to the scattering on the pinned uncompensated magnetization. This GMR component is responsible for the asymmetry of the $R(\Theta)$ curves with respect to the direction of the cooling field.

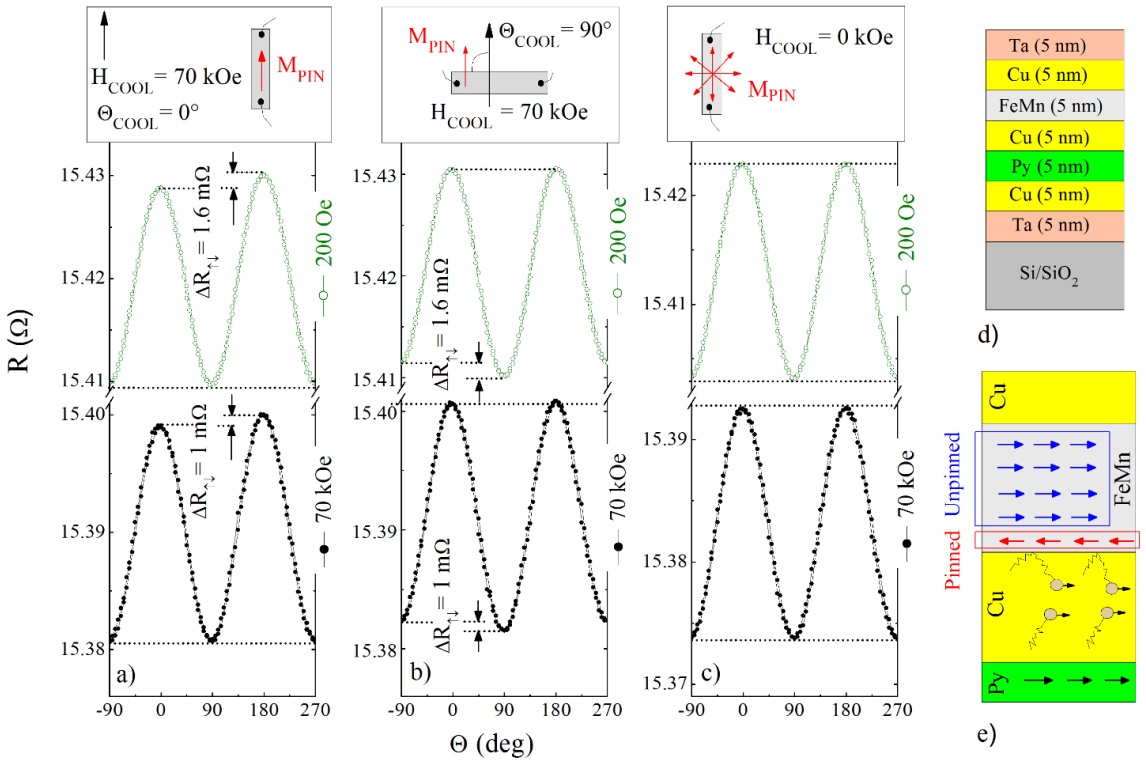

Figure 13 The angular dependences of resistance for the Ta(5 nm)/Cu(5 nm)/Py(2 nm)/Cu(5 nm)/FeMn(5 nm)/Cu(5 nm)/Ta(5 nm) AFSV measured in the 200-Oe (green line/open dots) and 70-kOe magnetic fields (black line/solid dots). The AFSV was cooled down (a) in a 70-kOe magnetic field applied parallel to the long edge of the stripe (Θ_{COOL} = 0º), (b) in a 70-kOe magnetic field applied perpendicular to the long edge of the stripe (Θ_{COOL} = 90º), (c) in the zero magnetic field. The top insets depict the orientation of the valve while cooling and the direction of the pinned magnetization in it. (d) The structure of the AFSV. (e) The schematics depicts the scattering of electrons on the pinned magnetic moments at the bottom Cu/FeMn interface. (After Ref. [63])

To confirm that the GMR effect is caused by the pinned uncompensated magnetization in FeMn, the angular dependences of the resistance were measured after cooling down the Py/Cu/FeMn AFSV in the 70-kOe field applied perpendicular to the long edge of the stripe [Figure 13(b)], and after zero-field cooling [Figure 13(c)]. If Θ_{COOL} = 90º, R(0º) is equal to R(180º), whereas R(90º) is lower than R(180º). The decrease in resistance at Θ_{COOL} and its increase at Θ_{COOL} ± 180º is in agreement with the proposed

mechanism of GMR. When the AFSV is cooled down in zero magnetic field, the magnetic moments at the Cu/FeMn interface are pinned in random directions, hence, the AFSV does not exhibit the GMR effect [Figure 13(c)].

As discussed previously, for a classical spin valve, in which the magnetization in one of the F layers is pinned due to the EB with an AF, the GMR disappears if the amplitude of the external magnetic field considerably exceeds the EB field for the AF/F stack. Surprisingly, for the Py/Cu/FeMn AFSV, the difference between the resistances measured at Θ_{COOL} and Θ_{COOL} -180º, $\Delta R_{\uparrow\downarrow}$, is not zero even at 70 kOe. Moreover, $\Delta R_{\uparrow\downarrow}$ measured at 70 kOe is only 40 % smaller than $\Delta R_{\uparrow\downarrow}$ measured in 200 Oe [$\Delta R_{\uparrow\downarrow}$(200 Oe) = 1.6 mΩ, $\Delta R_{\uparrow\downarrow}$(70 kOe) = 1 mΩ] [Figure 13(a and b)]. Figure 14(a) shows the dependence of $\Delta R_{\uparrow\downarrow}$ on the amplitude of the magnetic field in which $\Delta R_{\uparrow\downarrow}(\Theta)$ was measured, H_{MEAS}. According to this dependence, the GMR is present even in 110 kOe, moreover, $\Delta R_{\uparrow\downarrow}$ becomes almost constant in high H_{MEAS}.

The hysteresis loop for the FeMn/Cu multilayers demonstrates about 2 kOe coercivity, which means that even unpinned uncompensated magnetization does not reverse in a small magnetic field. Hence, it can be assumed that both pinned and unpinned magnetization should have contributed to $\Delta R_{\uparrow\downarrow}$ measured in 200 Oe for the Py/CuFeMn AFSV, consequently, a considerable enhancement of $\Delta R_{\uparrow\downarrow}$ should have been expected when H_{MEAS} is below 2 kOe. However, no low-H_{MEAS} features are observed in the experimental $\Delta R_{\uparrow\downarrow}(H_{MEAS})$ curve [Figure 14(a)]. This observation suggests that scattering on the pinned uncompensated magnetization considerably prevails the scattering on the unpinned magnetization.

For those EB models which assume the presence of an uncompensated magnetization at the AF/F interface, the pinned uncompensated magnetization is included into the final expression for the EB field implicitly. Specifically, Equation (III-2) contains the areal coupling energy between the F and AF layers, J_{EB}, which is proportional to the pinned uncompensated magnetization at the AF/F interface. It means that, according to the Meiklejohn and Bean model, H_E must be proportional to the pinned magnetization. At the same time, according to the Drude model, $\Delta R_{\uparrow\downarrow}$ is inversely proportional to the mean free path of the free electrons which is inversely proportional to the density of the scattering centers or the pinned uncompensated magnetization. Hence, to a first approximation, $\Delta R_{\uparrow\downarrow}$ for the Py/Cu/FeMn AFSV and H_E for the Ta(5 nm)/[FeMn(5 nm)/Cu(5 nm)]$_{10}$/Ta(5 nm) multilayer are proportional to the pinned uncompensated magnetization in FeMn. It was of great interest to measure temperature and cooling-field dependences of $\Delta R_{\uparrow\downarrow}$ [Figure 14(b and c)] and compare them with the same dependences of H_E [Figure 8(a and c)]. It was observed that both $\Delta R_{\uparrow\downarrow}$ and $|H_E|$ grow with increasing H_{COOL}, but the shapes of these dependences are different [Figure 14(c) and Figure 8(c)]. H_E is saturated when H_{COOL} = 20 kOe, while $\Delta R_{\uparrow\downarrow}$ grows monotonically up to 140 kOe. $|H_E|$ demonstrates a slow rise when the temperature is decreasing from 200 K to 50 K followed by fast growth in the temperature region between 50 and 10 K [Figure 8(c)]. At the same time, $\Delta R_{\uparrow\downarrow}$ for the Py/Cu/FeMn AFSV experiences linear growth when the temperature decreases below 200 K, leveling off at around 130 K [Figure 14(c)]. It is not clear why $\Delta R_{\uparrow\downarrow}$ and H_E demonstrate such different trends. Along with the pinned uncompensated magnetization, H_E is strongly affected by the coupling between the pinned

and unpinned uncompensated magnetizations in FeMn. In principle, it is possible that H_E is mostly mediated by this coupling, that in turn, results in the absence of the correlation between the $\Delta R_{\uparrow\downarrow}(T)$ and $H_E(T)$ curves.

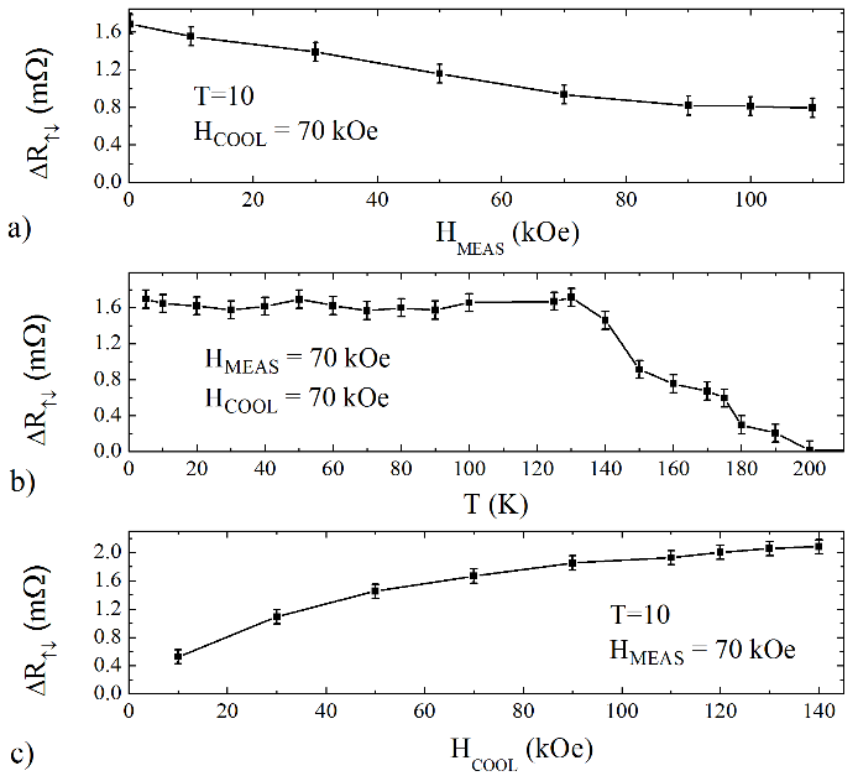

Figure 14 The difference between the resistances measured at Θ_{COOL} and Θ_{COOL} -180º, $\Delta R_{\uparrow\downarrow}$, for the Ta(5 nm)/Cu(5 nm)/Py(2 nm)/Cu(5 nm)/FeMn(5 nm)/Cu(5 nm)/Ta(5 nm) AFSV as functions of (a) magnetic field the $R(\Theta)$ dependences were measured, H_{MEAS}, (b) temperature, and (c) magnetic field the valve was cooled down, H_{COOL}. (After Ref. [63])

III.8.3 FeMn/Cu/Py antiferromagnet-ferromagnet spin valve

Figure 15(a) shows the angular dependence of the resistance for the FeMn/Cu/Py AFSV measured at 10 K in a 70-kOe magnetic field after the AFSV was cooled down from 300 K in the 70-kOe magnetic field. Although GMR is present, it is an order of magnitude smaller than that for the Py/Cu/FeMn AFSV (see the inset). Moreover, $\Delta R_{\uparrow\downarrow}$=

0 mΩ for the FeMn/Cu/Py AFSV with a 15-nm-thick FeMn layer. Hence, as it was already shown previously using the NR and magnetometry techniques, the two interfaces of FeMn with Cu are not identical. The pinned magnetization is formed only at the bottom Cu/FeMn interface, and no pinning occurs at the top FeMn/Cu interface. For the FeMn/Cu/Py AFSV with a 5-nm-thick FeMn layer, the FeMn thickness is comparable to the spin-diffusion length in FeMn (1.8 ± 0.5 nm).[80] Presumably, a part of the polarized carriers is able to penetrate through the 5 nm of FeMn layer and scatter on the bottom Cu/FeMn interface [Figure 15(c)], thus providing the small GMR observed in the experiment.

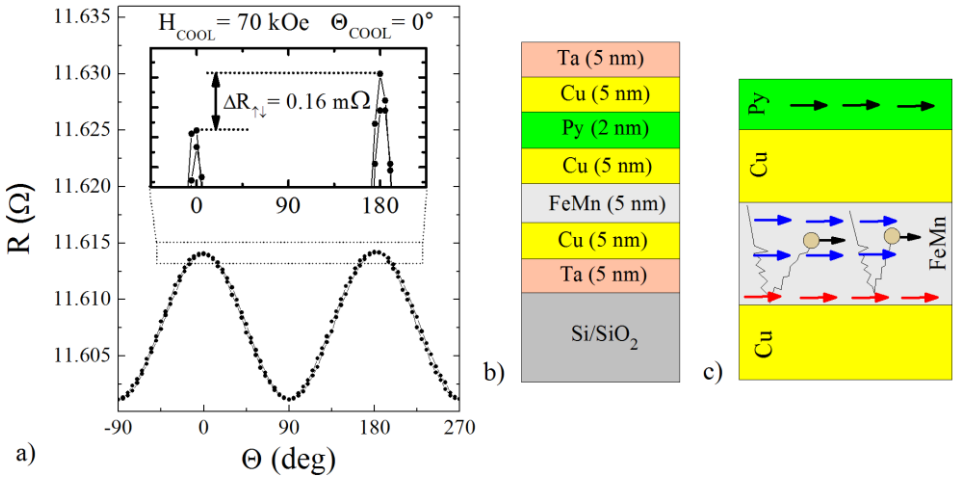

Figure 15 (a) The angular dependence of the resistance for the Ta(5 nm)/Cu(5 nm)/FeMn(5 nm)/Cu(5 nm)/Py(2 nm)/Cu(5 nm)/Ta(5 nm) AFSV measured at 10 K in a 70-kOe magnetic field after the AFSV was cooled down from 300 K in the 70-kOe magnetic field. (b) The structure of the AFSV. (c) The schematic depicts the scattering of electrons on the pinned magnetic moments at the bottom Cu/FeMn interface. (After Ref. [63])

III.8.4 Discussion of magnetotransport data

Magnetoresistance measurements have been utilized previously for studying pinned and unpinned uncompensated magnetization in AFs.[81-83] However, measuring

angular dependences of the AFSVs resistance provides a unique capability: the behavior of the pinned uncompensated magnetization can be studied in high magnetic fields. Thus, it was demonstrated that there is a pinned uncompensated magnetization at the bottom Cu/FeMn interface which does not reverse even in a 110-kOe magnetic field.

In general, a pinned uncompensated magnetization can be due to an imbalance between the AF sublattices (and thus the "culprit" spins are still a part of those sublattices), or due to the defects. For the former scenario, the average over a macroscopic scale given by $<\vec{m}\cdot\vec{L}>$ is non-zero, while for the latter, this average is zero. Here, $\vec{L}$ is the AF order parameter, the vector difference between the magnetizations of the sublattices, $\vec{L} = \overrightarrow{M_1} - \overrightarrow{M_2}$ in case of two sublattices, and $\vec{m}$ is the uncompensated magnetizations in the AF. In the first case, $\vec{m} = \overrightarrow{M_1} + \overrightarrow{M_2} \neq 0$. As a result, in the first case, the system is at a macroscopic equilibrium. In contrast, in the second scenario, the system is not at the thermodynamic equilibrium: the two states with the opposite direction of $<\vec{m}>$ have the same energy, and thus, a moderate field can reverse the direction of $<\vec{m}>$ to the opposite. That is, due to the random nature of defects, the two configurations with the opposite directions of this magnetization have the same value for the energy term describing macroscopic coupling to the AF order parameter (vector $\vec{L}$). As a result, when a finite field sufficient to overcome the uniaxial anisotropy, i.e. to rotate this magnetization 90° away from the initial state (the direction of the cooling field) is applied, the coupling to the AF does not give the preference to one of the two opposite magnetization directions.

The fact that the pinning survives in a high magnetic field, indicates that the pinned magnetization is uniquely linked to the orientation of the AF domain (described by $\vec{L}$). In

this case, applying arbitrarily high magnetic field isothermally will not change the direction of the pinned uncompensated magnetization, unless the entire AF domain is reversed or the AF order is destroyed (via e.g. spin flop). Thus, the pinned magnetization is in an equilibrium state with the spin structure of FeMn, and hence, its origin is attributed to the imbalance between the AF sublattices.

III.9 Interdependence of Structural and Magnetic Properties. Stress in FeMn/Cu Multilayers Films

III.9.1 Correlation between internal stress in multilayer and exchange bias

During the PNR measurements for the Ta(5 nm)/[FeMn(15 nm)/Cu(5 nm)]$_{10}$/Ta(5 nm) film, it was noticed that the shape of the collimated neutron beam got distorted after the reflection (the top-right inset Figure 16). The same beam reflected by the Ta(5 nm)/[FeMn(15 nm)/Ta(5 nm)]$_{10}$ multilayer did not demonstrate this behavior. The distortion of the beam can be explained by bending of the FeMn/Cu sample (the top-right inset Figure 16), which happens due to the difference of thermal expansion of the materials in different layers. Among five materials composing the samples (Si, SiO_2, Cu, Ta, FeMn), Cu has the highest thermal expansion coefficient, α, whereas Si and SiO_2 have the lowest coefficients: at 300 K, $\alpha_{Cu} = 16.69\times10^{-6}$ K^{-1}, $\alpha_{FeMn} = 10.2\times10^{-6}$ K^{-1}, $\alpha_{Ta} = 6.6\times10^{-6}$ K^{-1}, $\alpha_{Si} = 2.62\times10^{-6}$ K^{-1}, $\alpha_{SiO2} = 0.55\times10^{-6}$ K^{-1}.[84-90] Hence, the highest stress is expected in the multilayer with Cu, which can lead to deformation of the entire sample at low temperatures.

Figure 16 shows a temperature dependence of the beam-profile bending, defined as a number of detector's pixels the top and bottom of the profile are horizontally shifted

with respect to each other (green line), as well as the dependence of $|H_E|$ (black line). The curves demonstrate a similar trend: both bending and $|H_E|$ grow at low temperatures. Based on this correlation and the fact that the bending is observed only for the multilayer with Cu, it was proposed that the stress can be responsible for the pinning magnetization in FeMn.[69]

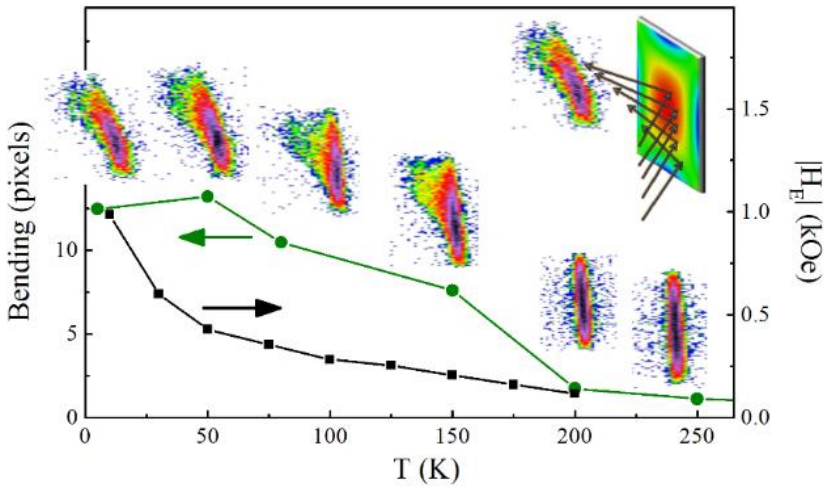

Figure 16 The temperature dependences of the neutron-beam-profile bending (green dots/line) and the absolute value of exchange bias field, $|H_E|$ (black squares/line). The bending is defined as a number of detector's pixels the top and bottom of the profile are horizontally shifted with respect to each other. The images near each green dot show the neutron-beam profile at the corresponding temperatures. The top-right inset depicts the neutron scattering on the bent (twisted) sample. (After Ref. [69])

III.9.2 Mechanisms of uncompensated magnetization pinning due to internal stress in FeMn

There are two main mechanisms which can relate the internal stress and the deformation of the FeMn lattice to the enhancement of the exchange bias field. As discussed previously, the lattice mismatch between FeMn and Cu is about 0.5%. This provides coherent growth of these layers without relaxing by generating misfit or

dislocation. The XRD characterization confirms that assumption. In contrast, the lattice mismatch for FeMn and Ta is about 10%. Additionally, the XRD data indicate that Ta and FeMn are most probably amorphous in the FeMn/Ta multilayers [Figure 4(a)]. Hence, the stress in the FeMn/Ta multilayer is relaxed by generating misfits and dislocations. The temperature expansion characteristics of FeMn and Cu are different in the 10–300 K temperature range.[84, 86, 89, 90] Cu contraction significantly exceeds that for FeMn, Ta, and Si. Hence, the mismatch of the thermal expansions can produce a significant internal stress in FeMn and Cu layer at low temperatures.

The stress can change the magnetic anisotropy of the FeMn atoms at the interface with Cu making it magnetically harder, which enhances pinning.[91-93] However, the enhancement of the anisotropy causes a moderate change in the coercivity and EB field. It is not anticipated that the anisotropy keeps the pinned uncompensated magnetization at the Cu/FeMn interface from reversing in a 110-kOe magnetic field.

Along with enhancing the anisotropy, the stress can also affect the symmetry of the AF sublattices, which can lead to the pinning of the uncompensated magnetization at the bottom Cu/FeMn interface. The mechanism of this pinning can be as follows. Since the FeMn crystal has a face centered cubic structure, three different AF magnetic structures can be realized for the crystal: 1Q, 2Q, 3Q.[94, 95] First principle calculations showed that the 3Q magnetic structure corresponds to the lowest energy, thus, 3Q is a ground magnetic state of the system. Following Belashchenko[57] and Andreev[96] arguments, since the time-reversal symmetry is broken for the 3Q structure, it can be assumed that an equilibrium magnetization appears at the boundary of the FeMn lattice. However, for the

exchange-only interaction, the 3Q structure is forbidden from having the magnetization at the boundary, while, for spin-orbit coupling, the surface magnetization is relatively low. At the same time, it is also known that the 3Q structure is piezomagnetic, and consequently, the stress can generate the magnetization at the boundary of the FeMn layer. This surface magnetization is a part of the AF spin structure, and hence, to reverse this magnetization the entire AF domain must be reversed. Based on the fact that the pinned magnetization at the bottom Cu/FeMn interface does not reverse even in high magnetic fields, this pinning scenario is more consistent for explanation of the EB effect in the FeMn/Cu multilayers.

III.9.3 Study of internal stress in FeMn-based films at room temperature using profilometry measurements

To check the hypothesis on the coherent growth of FeMn and Cu layers, the internal stress in the FeMn/Cu and FeMn/Ta multilayers at room temperature was analyzed using a three-dimensional contact profilometer (Dektak 8).

Initially, the surface profile of two clean 2" Si/SiO_2 wafers were measured, which allowed determining the substrates radius of curvature before the deposition, R_{PRE}. Then, the Ta(5 nm)/10x[FeMn(5 nm)/Cu(15 nm)]/Ta(5 nm) and Ta(5 nm)/10x[FeMn(5 nm)/Ta(15 nm)]/Ta(5 nm) films were deposited at an ambient temperature on top of the first and second substrates, respectively. After that, the surface profiles of the substrates with the films were scanned again to determine the curvature radius of the substrate after the deposition, R_{POST}. Knowing R_{POST} and R_{PRE}, the average stress σ in the FeMn/Cu and FeMn/Ta multilayers can be estimated using the Stoney equation:[97]

$$\sigma = \frac{1}{6}\left(\frac{1}{R_{POST}} - \frac{1}{R_{PRE}}\right)\frac{Et_S^2}{(1-\upsilon)t_F}, \qquad \text{(III-4)}$$

where E is Young's modulus of the substrate, υ is Poisson's ratio of substrate, t_S is the substrate thickness, t_F is the film thickness. The measurements show that there is a small tensile stress in the as-grown Ta(5 nm)/10x[FeMn(5 nm)/Cu(15 nm)]/Ta(5 nm) film, $\sigma_{FeMn/Cu} = 2.2 \times 10^8$ Dynes/cm^2. At the same time, the stress in the Ta(5 nm)/10x[FeMn(5 nm)/Ta(15 nm)]/Ta(5 nm) film is compressive, $\sigma_{FeMn/Ta} = -2.9 \times 10^9$ Dynes/cm^2. The absolute value of $\sigma_{FeMn/Ta}$ is almost an order of magnitude higher than $\sigma_{FeMn/Cu}$. These results are rather unexpected: The small lattice mismatch between FeMn and Cu (0.5 %), combined with the coherent growth should produce larger stress in FeMn grown on Cu, than in FeMn grown on Ta. The much larger lattice mismatch between FeMn and Ta (10 %) produces defects that should relax growth-induced stress in FeMn grown on Ta. Moreover, Ta is very likely to be amorphous, which should produce even smaller stress on FeMn. In contrast, the experimental results indicate the opposite relation between the stress magnitudes for the two samples. This means that some other factors, for example an in-plane growth morphology, must play a crucial role here. The difference in the stress sign for the multilayers with Cu and Ta is a strong confirmation for that. Thus, the stress measurement of the as-prepared samples cannot help us verifying the hypothesis about growth-induced strain in FeMn.

III.9.4 Study of internal stress in FeMn-based at different temperatures using microcantilever measurements

The bending of the neutron beam profiles at different temperatures suggests only that there is a cooling-induced deformation in the FeMn/Cu multilayers. However, it is challenging to measure the amount of the bending and the internal stress in the film using this technique. In order to study the thermally-induced stress in the FeMn-based multilayers in a more controllable manner, we fabricated Si_3N_4 microcantilevers with $[FeMn(5\ nm)/Cu(5\ nm)]_{10}$ film on top of it. The stress develops in the films when the cantilever is cooled down. The internal stress in the film can be evaluated based on the deflection of the cantilevers' tip at different temperatures.[98] This stress is inversely proportional to the curvature radius of the cantilever, R [Equation (III-4)]. In turn, if the deflection of the cantilever Δd is small [Figure 3(c)], it can be expressed as

$$\Delta d = R(1-\cos(\Theta)) \approx L^2/(2R), \qquad \text{(III-5)}$$

where L is the length of the cantilever. Hence, to a first approximation, the internal stress is proportional to the deflection of the cantilever.

Photographs of the cantilever taken at 290 K and 10 K are shown in Figure 17(a and b), respectively. The cantilevers' deflection is substantial at low temperatures. Analysis of the photos taken at different temperatures yielded a temperature dependence of the cantilever deflection, Δd [Figure 17(c)]. The cantilevers start to bend when the temperature decreases below 250 K. Two different temperature regions can be distinguished in the $\Delta d(T)$ curve. The deflection, Δd, grows rapidly between 200 and 160 K. Below 160 K, Δd grows at a lower rate. Even though both Δd and H_E rise when

the temperature is decreased, the shapes of the $\Delta d(T)$ curve [Figure 17(c)] and the $H_E(T)$ curve [Figure 8(a)] are very different. At the same time, the shape of the $\Delta d(T)$ curve almost reproduces the shape of the $\Delta R_{\uparrow\downarrow}(T)$ curve for the Py/Cu/FeMn AFSV [Figure 14(b)]. As discussed, to a first approximation, $\Delta R_{\uparrow\downarrow}$ is proportional to the pinned magnetization in FeMn. Hence, the temperature dependence of the pinned uncompensated magnetization at the Cu/FeMn interface correlates with that for the internal stress in the FeMn/Cu multilayer. This indicates that the pinning in the FeMn/Cu multilayers can be produced by stress. As discussed above, the stress increases the anisotropy and breaks the symmetry between different AF sublattices of FeMn, which results in appearance of the strongly pinned uncompensated magnetization at the Cu/FeMn interface.

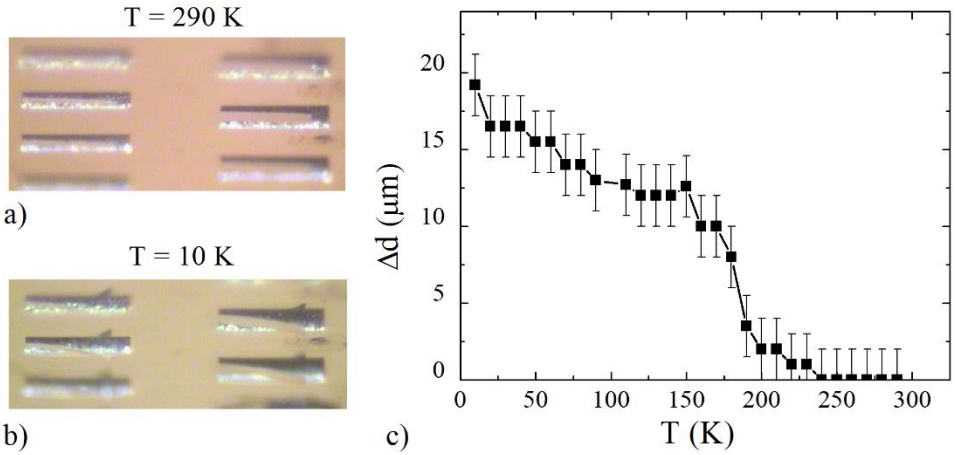

Figure 17 The photo of Si_3N_4/Ta(5 nm)/[FeMn(5 nm)/Cu(5 nm)]$_{10}$/Ta(5 nm) microcantilevers taken at (a) 290 K and (b) 10 K. (c) The deflection of the cantilever, Δd, at different temperatures.

III.9.5 Exchange bias in FeMn/Cu multilayer grown on top of Si_3N_4 membrane

To investigate the effect of the internal stress on the pinned magnetization and the EB, a [FeMn(5 nm)/Cu(5 nm)]$_{10}$ multilayer film was grown on top of a 100-nm-thick

Si_3N_4 membrane. The size of the membrane is 5 mm × 5 mm. The film was deposited only on a 1.5 mm × 1.5 mm Si_3N_4 window in the middle of the membrane. The goal was to check the following hypothesis: since the thickness of the FeMn/Cu multilayer film is comparable to the thickness of the Si_3N_4 layer, the internal stress inside the multilayer is different compared to the stress in the FeMn/Cu multilayer grown on the Si/SiO_2 substrate. Hence, it was expected that the difference in the stress would affect the magnetic properties (H_E, H_C, M_R) of the multilayer.

The magnetization curve of the multilayer was measured at 10 K after the sample was cooled down from 300 K to 10 K in the 70-kOe magnetic field. The measurement showed that the coercive and EB fields of the multilayer on the Si_3N_4 membrane were identical to those for the multilayer on the Si/SiO_2 substrate. Thus, this experiment did not confirm a direct correlation between the EB and stress in the FeMn/Cu multilayer. A further study is necessary to conclude on the interdependence of structural and magnetic properties of the FeMn/Cu multilayers.

III.10 Conclusions on Exchange Bias in FeMn/Cu Multilayer

The FeMn/Cu multilayer is a unique heterostructure which demonstrates the EB effect even though it does not contain any explicit ferromagnetic materials. The analysis shows that the EB effect originates from the interaction between the pinned and unpinned uncompensated magnetizations in FeMn. The magnetometry measurements demonstrated that the unpinned uncompensated magnetization is homogeneously distributed within the FeMn layers, while the pinned uncompensated magnetization forms at the interfaces

between FeMn and Cu. This unpinned uncompensated magnetization originates from the Fe clusters which exist in the FeMn lattice due to the defects.

Combination of the neutron and x-ray reflectometry demonstrated that, for the Cu/FeMn/Cu trilayer, the chemical structure of the FeMn layers is very inhomogeneous over its thicknesses. Namely, the FeMn contains the Mn-rich portion near the interface with the bottom Cu layer.

The specially designed ferromagnet-antiferromagnet spin valves were developed to study the pinned uncompensated magnetization using the magnetotransport approach. The angle-dependent measurements of the spin valves resistance revealed that the pinning occurs only at the interface between FeMn and the bottom Cu layers. Thus, two interfaces of FeMn with Cu are different structurally and magnetically. It was shown that the pinned magnetization does not reverse even in a 110-kOe magnetic field. Such strong pinning can occur only if the pinned magnetic moments are a part of the AF spin structure of FeMn. The defects in FeMn or spin-glass CuMn alloy between the FeMn and Cu layers would have caused considerably weaker pinning.

Since the temperature dependences of the pinned uncompensated magnetization and the internal stress in the FeMn/Cu multilayer correlate with each other, it was assumed that the interdependence of structural and magnetic properties can be responsible for the pinning of the uncompensated magnetization. Namely, first, because of the piezomagnetism of the AF 3Q structure of FeMn, and second, due to the fact that the time-reversal symmetry is broken for this 3Q structure, the internal stress results in the appearance of the uncompensated magnetization at the FeMn boundaries. It is important

that this magnetization is a part of the AF spin structure, and hence, it preserves its direction unless the entire AF domain is reversed. The fact that the strongly pinned magnetization was detected at the bottom Cu/FeMn interface partially confirms the assumption that the EB effect for the FeMn/Cu multilayers can be caused by the internal stress. It is believed that this mechanism can also be responsible for the EB effect in many other EB systems. Potentially, the stress may enable controlling the EB and hence magnetization of the AF/F heterostructures.

CHAPTER IV

MAGNETIZATION REVERSAL IN PERMALLOY/GADOLINIUM MULTILAYERS AND MICRODISKS*†

IV.1 Introduction

IV.1.1 Rare earth/transition heterostructures

In 1935, Urbain, Weiss, and Trombe reported ferromagnetism in Gd. This discovery triggered a quickly-developing era of rare-earth (RE) magnetism.[99] Due to a variety of unique properties and phenomena RE metals demonstrate, RE magnetism remains a rapidly developing, albeit immensely challenging, scientific topic even today. Magnetic moments of the RE elements come mostly from the angular momentum of 4*f* electrons which are highly screened by 5*s* and 6*p* orbitals; the radii of the 4*f* orbitals are much smaller than radii of the filled 5*s* and 6*p* orbitals, as well as the interatomic distances in the RE crystals.[100] The strong localization yields, for example, that the angular and spin moments of the RE atoms in a crystal are similar to those for free RE atoms. At the same time, the strong localization makes the direct exchange coupling insignificant for the RE metals. It was shown that indirect or so-called Ruderman–Kittel–Kasuya–Yosida (RKKY) interaction[101] is responsible for the exchange coupling in RE metals; specifically, the

* Portions of this chapter are reprinted from Pavel N. Lapa, Junjia Ding, John E. Pearson, Valentine Novosad, J. S. Jiang, and Axel Hoffmann "Magnetization reversal in Py/Gd heterostructures" (arXiv:1703.08626 (2017)), which is a preprint of the article submitted for publication to the Physical Review B journal.

† Portions of this chapter are reprinted from Pavel N. Lapa, Junjia Ding, Charudatta Phatak, John E. Pearson, J. S. Jiang, Axel Hoffmann, and Valentine Novosad "Magnetic vortex nucleation/annihilation in artificial-ferrimagnet microdisks" (arXiv:1705.06398 (2017)), which is a preprint of the article submitted for publication to the Journal of Applied Physics.

interaction of the 4*f* electrons occurs by means of an indirect coupling through 5*d* and 6*s* electrons forming a conductive band. All REs can be divided into two categories depending on their atomic mass: light (from Ce to Eu) and heavy (from Gd to Tm). All heavy RE are ferromagnetic. Gd and Tb have the highest Curie temperature among them, 293 K and 230 K, respectively. The light REs exhibit antiferromagnetism, and reorder ferromagnetically at low temperatures. With respect to the magnetic structure, RE elements demonstrate a variety of spin-waves states in which the magnetization gradually changes its direction on the scale of an interatomic distance.[100]

Due to the indirect exchange interaction, the magnetic order of a RE can be considerably modified by tuning the spatial distribution of free electrons. One of the ways to do this is to place a thin layer of a RE metal into a proximity with another material. It is argued that even for a Gd film grown on a non-magnetic W substrate, magnetic order near the surface can be significantly enhanced.[102-104] When Gd is in proximity with a transition metal (TM), the effect becomes even more prominent.[105, 106] For a Fe/Gd multilayer, it was demonstrated that a few atomic monolayers of Gd coupled to the Fe layer have Curie temperature comparable to that of Fe,[107] regardless of the Curie temperature of bulk Gd being only 293 K. Another interesting property of Gd/TM heterostructures is an antiferromagnetic exchange interaction between Gd and TM. This results in magnetizations of adjacent Gd and TM layers being opposite to each other without any magnetic fields applied. The unusual antiferromagnetic coupling in combination with the enhancement of magnetic order triggered the use of Gd/TM heterostructures for artificial ferrimagnets applications. As of today, artificial ferrimagnets

have been implemented for spin mixing in superconducting spin valves.[108] Due to an out-of-plane anisotropy, Gd/Co[109] and Gd/Fe[110, 111] multilayers are promising materials for a bubble domain application.[112-114]

Furthermore, due to the lower ordering temperature of Gd compared to many ferromagnetic TM materials, the magnetization in the Gd layers demonstrates a stronger temperature dependence than the magnetization in the TM layers. For certain Gd/TM heterostructures, at a so-called "compensation temperature", the magnetic moment of the Gd layer becomes equal to the magnetic moment of the TM layer. Because of the antiferromagnetic coupling between the layers, this compensation results in a vanishing total magnetization for these Gd/TM multilayers.[115] Therefore, it is of particular interest to determine magnetization configurations and magnetization reversal mechanisms at the compensation temperature, where magnetic moments of the Gd and TM layers become equal. From a fundamental perspective, Camley and Tilley, using mean-field calculations, showed that, a so-called "twisted magnetic state" with a non-collinear configuration of magnetization over the film thickness can appear at the compensation temperature.[116] That is, magnetization of layers located near the top and bottom surfaces of a film begin to cant, forming a well-defined angle with respect to the external magnetic field. As the temperature approaches the compensation temperature, the twists propagate deeper into the multilayer. Camley and Tilley demonstrated that the characteristics of this twisted state strongly depends on the layered structure and its microscopic parameters. The magnetic behavior at the compensation temperature is also interesting due to potential applications. Recently, it was demonstrated that due to a thermally induced excitation, magnetization

of GdFeCo films[117-120] and Gd/Fe[121] artificial ferrimagnets can be switched across the compensation temperature optically, without applying external magnetic field. It is believed that the phenomenon can be used for developing new magnetic recording media.[122] In addition, the antiferromagnetic coupling can result in the formation of interfacial domain-walls, which only form and persist for applied magnetic fields exceeding a critical field.[123, 124]

The anisotropy of polycrystalline Gd and TM causes a hysteretic behavior of magnetization,[125] which drastically complicates analysis of magnetization reversal in the Gd/TM heterostructures. This complication can be minimized by using permalloy (Py = $Ni_{0.81}Fe_{0.19}$), which is a transition metal alloy with very low magnetic anisotropy. Thus, Gd and Py are very promising materials for fabrication of artificial ferrimagnets. Ranchal *et al.* demonstrated that coupling between Gd and Py is antiferromagnetic,[126, 127] and the intermixing of these materials strongly reduces their coupling energy.[7] The motivation for the first part of the project was to characterize quantitatively the coupling of Gd with Py and magnetic order in these layers, as well as to investigate proximity effects in Py/Gd artificial ferrimagnets.[128]

IV.1.2 Microdisks composed of magnetically soft rare earth/transition heterostructures

In order to minimize magnetic stray field and magnetostatic energy associated with it, the magnetization of a macroscopic ferromagnetic object typically develops an inhomogeneous domain structure. For nanosized objects, the cost of exchange energy due to the domain walls makes multi-domain state energetically unfavorable. Hence, for these

objects, uniformly or quasi-uniformly (C-state, S-state) magnetized single-domain states are realized, even in a zero magnetic field. For cylindrical microdisks, which have sizes in between macro- and nano-size regimes, another mechanism of a magnetic-flux elimination can be realized. Namely, in a zero magnetic field, magnetization curls azimuthally around the disk's geometrical center, forming a so-called "magnetic vortex"[129] [Figure 18]. To avoid discontinuity of magnetization in the geometrical center of the vortex, the magnetization lifts up from the disk plane within a narrow area containing the vortex center. The area with a nonzero out-of-plane component of magnetization is usually called a vortex core.[130] An increasing magnetic field causes the vortex to shift away from the geometrical center of the disk in the direction perpendicular to the magnetic field. When the magnetic field exceeds the critical value, which is defined by microscopic parameters of the material (exchange stiffness and magnetization) and geometrical parameters of the disk (diameter and height), the vortex is annihilated. Vice versa, a decreasing magnetic field drives the magnetization from a magnetically saturated state to the vortex nucleation, and the vortex core subsequently moves toward the geometrical center of the disk [Figure 18].

It is argued that the drastically reduced dipole-dipole interaction between disks and the topological nature of the vortex state can be utilized for storing binary information.[131, 132] In order to do this, the static[133] and dynamic[134-136] behavior of magnetic vortices have been studied extensively. Additional fundamental aspects, such as a magnetic structure of the vortex core or microscopic mechanisms of vortex nucleation/annihilation, have also attracted a lot of attention and have been investigated

using a variety of tools.[137-143] Thus, a fabrication of multilayered microdisks in which different layers are either coupled to each other[144, 145] or exchange biased with an antiferromagnet[146] has proved to be an efficient way to control the magnetization reversal.

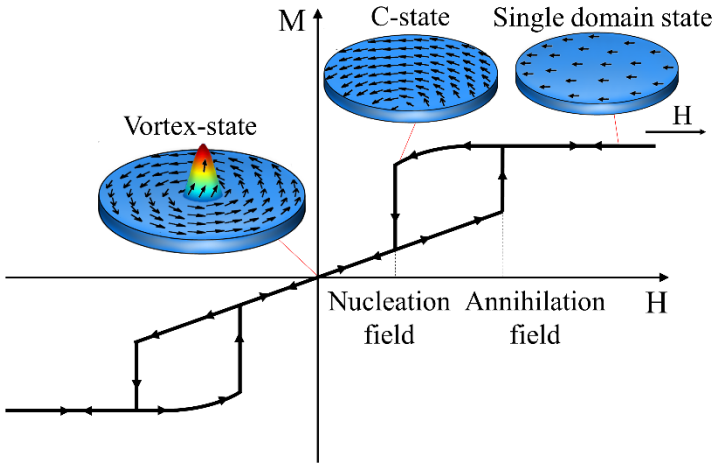

Figure 18 A schematic hysteresis loop for a microdisk composed of a magnetically soft material. Schematics above the curve depict the magnetization configurations realized inside the disk in different magnetic fields.

One of the main requirement for an observation of a vortex state in a magnetic microdisk is that the magnetic materials have very low anisotropy.[147] A typical choice of materials which satisfy this requirement includes magnetically soft permalloy (Py)[148] and polycrystalline Ni[149] and Fe.[143] For microdisks composed of these materials, the conventional approach to switch the magnetization from the vortex to uniformly-magnetized states is to change the amplitude of the externally-applied magnetic field. Since the Curie temperatures for these materials are high, their magnetic parameters (magnetization and exchange stiffness) are almost constant below room temperature. This means that for the microdisks composed of these materials, the nucleation and annihilation

fields demonstrate an insignificant change while the temperature is varied within the 10–300 K range.[142]

If a microdisk is composed of an artificial ferrimagnet with a very low anisotropy, the magnetic vortex can be a stable magnetization configuration for the microdisk. Due to the fact that the magnetization of an artificial ferrimagnet may change significantly when the temperature is swept from 300 to 10 K, the vortex nucleation and annihilation fields for the artificial-ferrimagnet microdisks may also vary significantly within this temperature range. In principle, it is possible that the vortex nucleation/annihilation transitions may occur in a constant magnetic field due to changing the microscopic parameters of the artificial-ferrimagnet for different temperatures. The motivation for the second part of the project was to study vortex nucleation and annihilation in microdisks composed of the Py/Gd multilayer, and thus, to detect the vortex nucleation/annihilation transitions occurring in a constant magnetic field.[150]

IV.2 Experimental Details

IV.2.1 Structures and fabrication details of Py/Gd heterostructures

Magnetron sputtering at ambient temperatures was used to fabricate three groups of films for the study of Py/Gd multilayers. All samples were grown on top of Si/SiO_2 substrates at room temperature. The deposition rates used for the sputter deposition of Gd and Py were 1.4 Å/sec and 0.7 Å/sec, respectively. The deposition rate for Gd was relatively high to prevent rapid oxidation of the material.[151] Besides, because the sputtering process was controlled by a software, the time delay between the end of deposition of one material (Py or Gd) and the beginning of the deposition of the other (Gd

or Py) was less than 15 seconds. 5-nm-thick Ta layers at the bottom and top of all the films were used as seed and capping layers, respectively.

The first group of samples consists of Py(50 nm)/Gd(4 nm) and Py(50 nm)/Au(0.5 nm)/Gd(4 nm) films. These films are designed to determine how proximity with Py influences the magnetization and exchange stiffness of Gd, as well as to evaluate the interlayer coupling between the two metals. The bilayer with a thin Au buffer serves to reveal how interlayer diffusion between Gd and Py affects the strength of the coupling and to show if the coupling can be controlled by placing a thin buffer between Py and Gd. The second group consists of Py/Gd multilayers $[Py(t)/Gd(t)]_{25}$, where t is 1 or 2 nm. The purpose of studying these samples is to determine the mechanism of the magnetization reversal in the vicinity of the compensation temperature. Finally, the third group of samples is designed for estimating the effective exchange stiffness in the Py/Gd multilayers. These samples are composed of a thick Py layer adjacent to a Py/Gd stack, *i.e.*, Py(50 nm)/$[Py(t)/Gd(t)]_{25}$, t =1 or 2 nm.

IV.2.2 Fabrication of Py/Gd microdisks

Two groups of microdisk arrays were prepared for the study. The disks from the first and second groups have $[Py(1\text{ nm})/Gd(1\text{ nm})]_{25}$ and $[Py(2\text{ nm})/Gd(2\text{ nm})]_{25}$ structures, respectively. The nominal diameter of each disk is 1.5 μm. In addition, two different approaches were used for fabrication of each group: etching and lift-off. For fabrication of lift-off disks, Si/SiO_2 wafers were spin-coated with photoresist, and an array of 1.5-μm holes were patterned by means of optical lithography. Then, after magnetron sputtering of multilayers, the lift-off procedure yielded arrays of 1.5-μm disks [Figure

19(a)]. The deposition rates used for the sputtering of Gd and Py coincide with those used for sputtering of the continuous films. For fabrication of the etched disks, the multilayers were sputtered on top of the Si/SiO_2 wafer. After that, the arrays of holes were patterned on top of the films, and then this pattern was transferred into arrays of photoresist disks using the image reversal technique described in II.1.2. The final steps were Ar-ion milling and removal of the photoresist caps on top of the disks by keeping the sample in acetone for 24 hours and then sonicating in acetone for 5 minutes. Additionally, the same array of $[Py(1\ nm)/Gd(1\ nm)]_{25}$ microdisks was fabricated on top of a Si_3N_4 membrane window for Lorentz transmission electron microscopy (TEM). These disks were prepared using the lift-off technique. Lorentz TEM images at different temperatures were taken in Fresnel imaging mode,[152] using a JEOL 2100F TEM microscope.

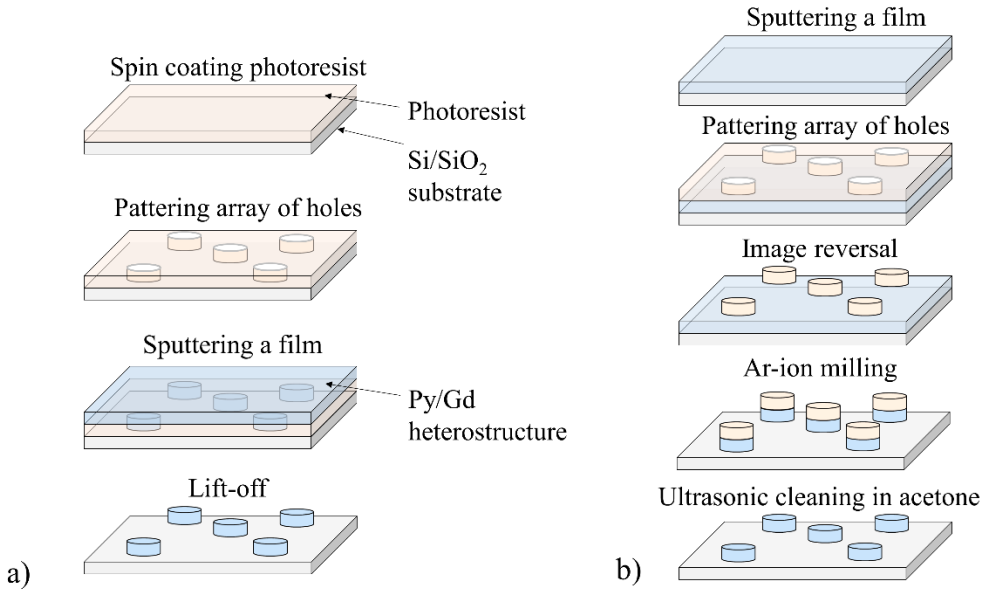

Figure 19 Schematics of the disk-fabrication processes using (a) lift-off and (b) etching.

IV.2.3 Experimental and simulation details on studying Py/Gd bilayer and multilayer films

The magnetic moment of the samples was measured using a SQUID magnetometer. Transport measurements were conducted using a conventional four-probe technique; the films were cut into the shape of 9 × 2 mm × mm stripes. Magnetic field was applied parallel to the films' surfaces.

To determine the magnetization reversal mechanism and quantitatively evaluate parameters of the Py/Gd films (exchange stiffness, magnetization, and interlayer coupling), the experimental data were simulated using the OOMMF micromagnetic simulation software.[153] Essentially, the micromagnetic model mimics a one-dimensional spin chain directed along the thickness of the film. To imitate an infinite plane, the demagnetization energy term was excluded from the calculation, while the magnetization was forced to rotate in plane. Thus, these simulations yield a depth profile of spins in the films, or rephrasing, they model in-plane domain-walls occurring in the films in different magnetic fields. The size of the mesh in the direction perpendicular to the film plane was chosen to be 0.25 nm.

IV.3 Magnetization Reversal of Py/Gd Bilayer Films

To determine the interfacial coupling between Py and Gd and to study how proximity affects magnetic properties of the metals, the Py(50 nm)/Gd(4 nm) and Py(50 nm)/Au(0.5 nm)/Gd(4 nm) films were prepared. The idea behind the design is as follows. Keeping the Gd layer thin allows minimizing the anisotropy energy, which, in turn, enables identifying effects of the interfacial interaction more clearly. At the same

time, the magnetization of a relatively thick Py layer is predominately along the externally applied magnetic field, thus making the Py layer effectively a "magnetic anchor". The temperature and magnetic field dependences of the magnetic moment for the films are compared with those for the reference Py(50 nm) film.

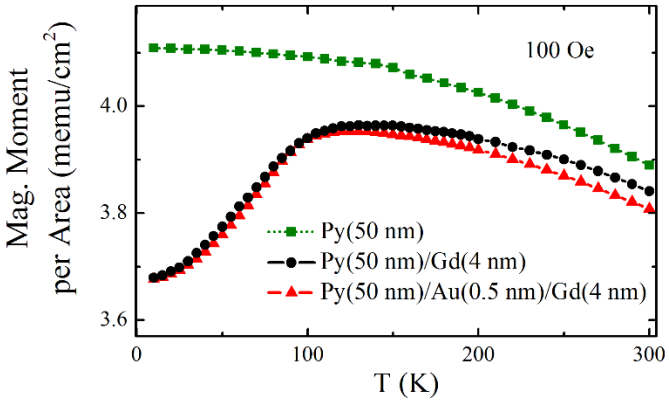

Figure 20 Temperature dependences of the magnetic moment per area measured in 100 Oe for the Py(50 nm) (green rectangles and line), Py(50 nm)/Gd(4 nm) (black dots and line), and Py(50 nm)/Au(0.5 nm)/Gd(4 nm) (red triangles and line) films. (After Ref. [128])

The temperature dependences of the magnetic moment normalized to the film area were measured in a small magnetic field (100 Oe) applied parallel to the surface plane (Figure 20). In contrast to a typical rise of magnetization with decreasing temperature as seen in the reference Py film, the total magnetic moment of the Py/Gd films (with and without Au) begins to decrease at temperatures below 120 K. This proves that the exchange interaction between Py and Gd is antiferromagnetic. Since the Gd magnetic moment developed at low temperature is antiferromagnetically coupled with that in Py, the total magnetic moment decreases. The magnetic moments of the Py/Gd samples are lower than the magnetic moment of the reference Py(50 nm) film even at temperatures

above 120 K. It is possible that due to proximity, a part of the Gd layer immediately adjacent to Py has a Curie temperature higher that the rest of the Gd layer. This part of the Gd layer remains ferromagnetic at higher temperatures, which reduces the magnetic moment of the Py/Gd films in comparison to the reference single-layer Py film even at temperatures above 120 K.

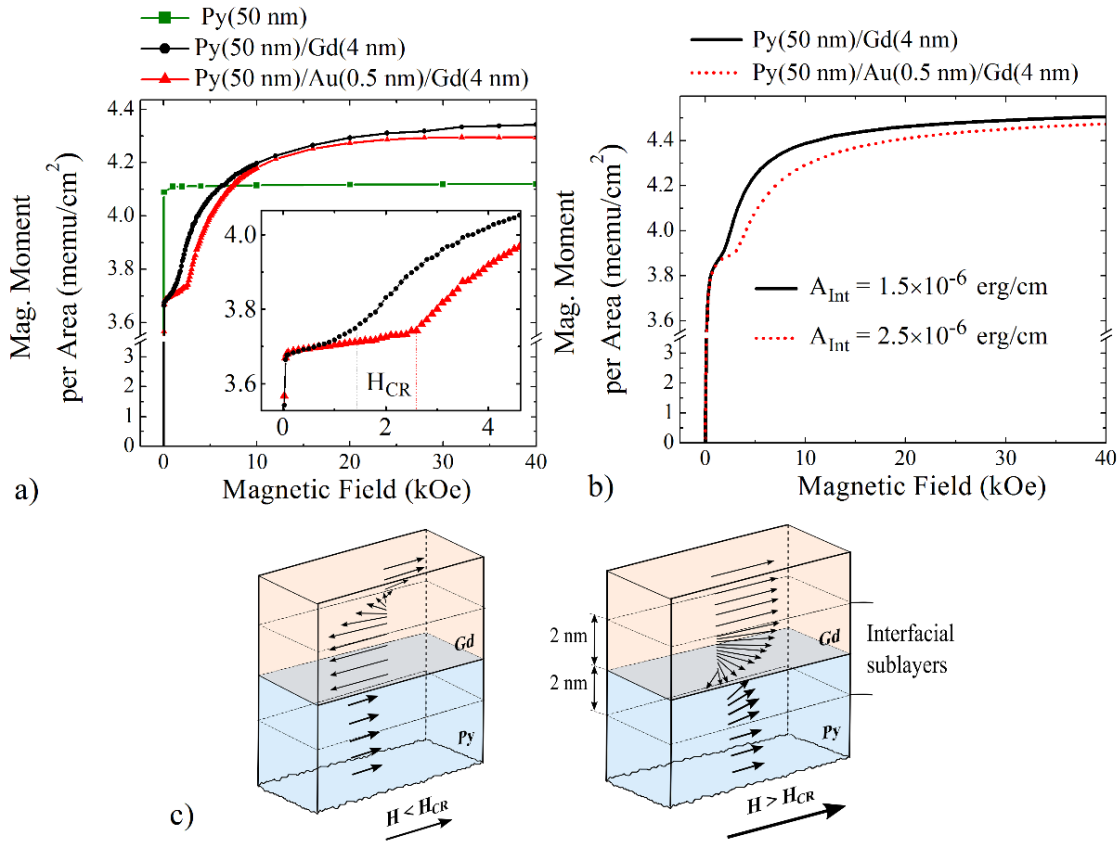

Figure 21 Magnetization curves for the Py(50 nm), Py(50 nm)/Gd(4 nm), and Py(50 nm)/Au(0.5 nm)/Gd(4 nm) films (a) measured at 10 K, (b) simulated. (c) Schematics of the exchange-spring twists in the Py/Gd bilayer above and below H_{CR}. Exchange stiffness (A_{Int}) of the interfacial sublayers was varied to simulate reversals for the Py/Gd bilayers with (A_{Int} = 1.5×10^{-6} erg/cm) and without the Au buffer (A_{Int} = 2.5×10^{-6} erg/cm). (After Ref. [128])

Experimental magnetization curves of the Py(50 nm)/Gd(4 nm) and Py(50 nm)/Au(0.5 nm)/Gd(4 nm) films [Figure 21(a)] demonstrate another interesting effect previously reported for Gd/Fe[154-156], Gd/Ni[105], and Gd/Co[157, 158] films, which is usually called a "spin-flop transition". Namely, at a critical field, H_{CR} = 1.3 kOe for the Py(50 nm)/Gd(4 nm) film, the magnetic moment exhibits a fast non-linear growth. In order to minimize the Zeeman energy, it becomes energetically favorable for the magnetization in the Gd layer to rotate so that it becomes aligned along the magnetic field. The microscopic mechanism of this rotation can be quite complicated, and it strongly depends on the microscopic parameters of the metals.

First, let us assume that the exchange stiffness of Gd and Py is high (rigid-spin approximation) and the interface coupling is weak in comparison to the interatomic coupling of Py and Gd. In this case, the spin-flop is realized by a coherent rotation of the magnetization in the entire Gd layer with respect to the magnetization in Py. Micromagnetic simulations show that, under the assumption of the rigid-spin approximation, the total magnetization would demonstrate a linear rise with the magnetic field above H_{CR}, followed by a saturation. However, the curves in Figure 21(a) demonstrate a different behavior: the magnetization grows nonlinearly, and the full saturation is not achieved even in high magnetic fields (40 kOe). It means that the assumption about the "weak" interface is unjustified for the system, and the switching at H_{CR} does not happen due to the coherent rotation of Py and Gd magnetization with respect to each other. Another important feature of the magnetization curves that the rigid-spin

approximation fails to explain is the almost linear rise of the magnetization with magnetic fields below H_{CR} [inset in Figure 21(a)].

It is clear that finite values of the exchange stiffness of Gd and Py must be taken into account for an adequate modeling of the magnetic reversal in the Py/Gd bilayer. Importantly, microscopic properties of materials at the Py/Gd interface are defined by two counteractive processes. On one hand, because the materials have different Curie temperatures, proximity is responsible for the reduction of the exchange stiffness in a thin Py sublayer adjacent to the interface, A_{Py_Int}, and the enhancement of that in a thin Gd sublayer adjacent to the interface, A_{Gd_Int}. On the other hand, intermixing of Py and Gd[105, 159] results in adding Ni to Gd which strongly reduces the Curie temperature of the latter,[7, 160] hence, A_{Gd_Int} and A_{Py_Int} are suppressed.

Based on the temperature and magnetic field dependences of the magnetization, the following micromagnetic model was proposed to simulate the experimental data for the Py/Gd bilayer. At low temperatures, the exchange stiffness of a 2 nm thick Gd sublayer and a 2 nm thick sublayer of Py adjacent to the interface is relatively low ($A_{Gd\_Int} = A_{Py\_Int} = A_{Int} = 1.5\times10^{-7}$ erg/cm). Due to the low stiffness, the magnetizations in these interfacial Gd and Py sublayers begin to twist along the field above H_{CR} [Figure 21(c)]. A micromagnetic simulation [Figure 21(b)] shows this twist causes a nonlinear rise of the magnetization when the magnetic field is increased above H_{CR}, and the full saturation is not achieved even in high magnetic fields, which is in agreement with the experimental data. The proposed micromagnetic model is also capable of explaining the linear rise of magnetization for the magnetic field below H_{CR} [inset in Figure 21(a)].

Indeed, if the magnetic order in the top part of the Gd layer is extremely reduced, *e.g.*, its exchange stiffness, A_{Gd_Top}, is of the order of 1.5×10^{-9} erg/cm, then the magnetization in the top Gd sublayer aligns with the magnetic field; whereas the magnetization in the bottom interfacial Gd sublayer is directed opposite to the field. The simulation shows that this transition of spins from parallel to antiparallel-to-magnetic-field states is realized through another twist of magnetization within the Gd layer. This twist yields a modest rise of magnetization in low magnetic fields [Figure 21(b)]. The micromagnetic parameters used for the simulation are: M_{Py} = 810 emu/cm^3, A_{Py} = 10×10^{-7} erg/cm; M_{Gd} is 1800 emu/cm^3 and 1000 emu/cm^3 for the bottom (interfacial) and top Gd sublayers, respectively, $A_{Int} = 1.5\times10^{-7}$ erg/cm; $A_{Gd\_Top} = 1.5\times10^{-9}$ erg/cm; exchange stiffness through the Py-Gd interface ($A_{Py\text{-}Gd}$) is 1.5×10^{-7} erg/cm.

It was shown that the interfacial exchange coupling between Py and Gd can be controlled by inserting an ultrathin buffer between Gd and TM which blocks intermixing.[161] To determine how the stiffness of the interfacial exchange spring and, hence, H_{CR} is affected by a buffer layer, a 0.5 nm thick Au buffer was inserted between Py and Gd. The first effect of the buffer is that the total magnetic moment at temperatures above 170 K becomes lower than that for the bilayer without Au [Figure 20]. This means that due to the reduction of the intermixing, a larger part of the Gd layer is ferromagnetic at higher temperatures. Therefore, the drop of the total magnetic moment due to the antiferromagnetic alignment of Gd and Py is more substantial. Second, H_{CR} for the Py(50 nm)/Au(0.5 nm)/Gd(4 nm) trilayer is 2.4 kOe, which is almost twice as large as H_{CR} for the Py/Gd bilayer (1.3 kOe) [Figure 21(a)]. From these observations, three important

conclusions can be drawn. First, the increase of H_{CR} for the bilayer with the Au layer proves that the interface by itself is not a "weak link" of the coupling, otherwise the presence of the Au layer would lead to a reduction of the coupling and H_{CR}. Second, the coupling is defined by the exchange stiffness A_{Int} of the Py and Gd interfacial sublayers, which is strongly affected by the intermixing. Third, the intermixing between Py and Gd and, hence, the effective coupling can be controlled by placing an ultrathin conducting buffer layer between the metals. The proposed micromagnetic model is capable to fit magnetization curves for both samples, with and without the Au buffer. The only parameter that must be adjusted is A_{Int}. $A_{Int} = 2.5\times10^{-7}$ erg/cm provides a good fit of the experimental magnetization curve for the Py(50 nm)/Au(0.5 nm)/Gd(4 nm) film [Figure 21(b)].

IV.4 Magnetization Reversal of Py/Gd Multilayer Films

IV.4.1 Magnetometry data and analysis

In the micromagnetic model for the bilayers, to account for the change in the exchange stiffness of the Py and Gd near the interface due to proximity effect, the 2-nm-thick sublayers were introduced on each side of the Py/Gd interface [Figure 21(c)]. Interdiffusion of Gd and Py was neglected in the model. To determine how the intermixing influences the magnetic properties of an artificial Py/Gd ferrimagnet and to improve the micromagnetic model proposed for explaining the magnetization reversal process in the Py/Gd bilayers, magnetic and magneto-transport properties of the $[Py(1\ nm)/Gd(1\ nm)]_{25}$ and $[Py(2\ nm)/Gd(2\ nm)]_{25}$ multilayers were studied over a wide range of temperatures and magnetic fields.

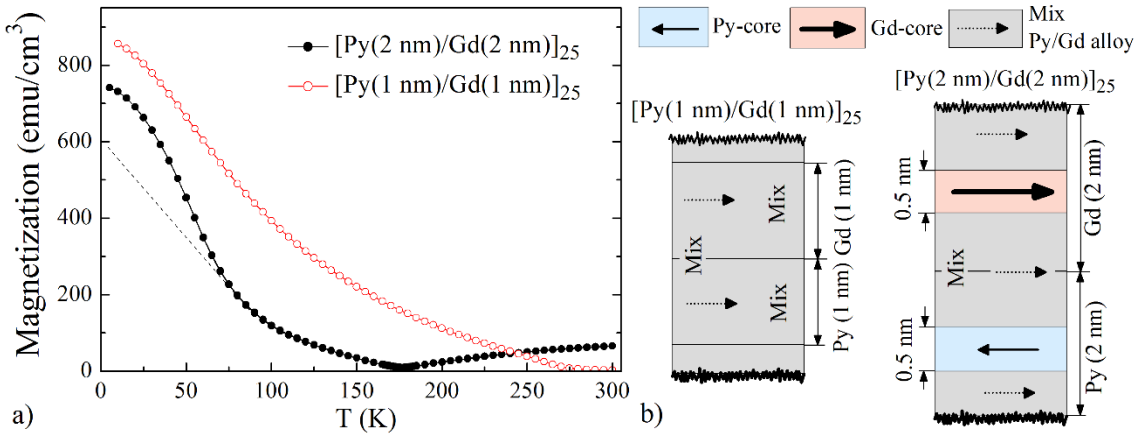

Figure 22 (a) Temperature dependences of the magnetization for the [Py(1 nm)/Gd(1 nm)]$_{25}$ film (open red circles) and [Py(2 nm)/Gd(2 nm)]$_{25}$ (solid black circles) films; a dotted line is drawn to illustrate the contribution of the Gd-core sublayers to the total magnetization; (b) schematics illustrate a material distribution and positions of the Py-core (blue color), Gd-core (red color), and Mix (grey color) magnetic sublayers in the Py/Gd multilayers. (After Ref. [128])

The temperature dependences of the magnetization for these samples measured in a small magnetic field (100 Oe) are shown in Figure 22(a). The [Py(1 nm)/Gd(1 nm)]$_{25}$ film becomes ferromagnetic only at temperatures below 275 K. This temperature is below the Curie temperatures for bulk Py (850 K) and Gd (292 K). The absence of a clear compensation temperature and the reduced ordering temperature for the thinner Py and Gd layers suggest that the intermixing is a substantial issue for this multilayer sample. Basically, the intermixing is so significant that, in the first approximation, it can be assumed that the entire [Py(1 nm)/Gd(1 nm)]$_{25}$ film is composed of a PyGd alloy [Figure 22(b)].

The [Py(2 nm)/Gd(2 nm)]$_{25}$ film demonstrates a more complex, ferrimagnetic-like, temperature dependence of the magnetization [Figure 22(a) solid dots]. The magnetization of this multilayer is low (70 emu/cm^3) at 300 K. Most likely, this magnetization is due to

thin core parts of the Py layers which are not affected by the intermixing of Py and Gd [Figure 22(b)]. At high temperatures, the magnetization in these core sublayers of Py is aligned along the magnetic field. While the film is cooled down the magnetization of the mixed interfacial regions of Py and Gd (denoted "Mix" further in the text) starts to grow. Importantly, the direction of the magnetization in the Mix sublayers is defined by the magnetic moments of the Gd atoms, which tend to align opposite to the magnetization in the Py-core sublayers. This leads to a decrease in the total magnetization. At the compensation temperature of 176 K, the magnetic moment of the Py-core sublayers is equal to the magnetic moment of the mixed sublayers, resulting in almost zero magnetization (8 emu/cm^3) of the multilayer at 176 K. Below the compensation temperature, the magnetic moment of the Mix sublayers becomes higher than the moment of the Py-core sublayers, hence, the magnetization is Gd-aligned at these temperatures. Importantly, in contrast to the [Py(1 nm)/Gd(1 nm)]$_{25}$ multilayer, the magnetization begins to rise strongly at temperatures below 75 K. It is assumed that, similarly to the Py-core sublayers, the core parts of the Gd layers are not affected by the intermixing. The rise of the magnetization in these Gd-core sublayers below 75 K causes the upturn of the total magnetization. By taking into account the values of the magnetization at 300 K and 10 K and assuming that the temperature dependence of the magnetization for the Mix sublayers coincides with that for the [Py(1 nm)/Gd(1 nm)]$_{25}$ film, it was estimated that the effective thicknesses of the Py-core and Gd-core sublayers are about 0.5 nm, wherein the rest of the multilayer is filled with the PyGd alloy [Figure 22(b)].

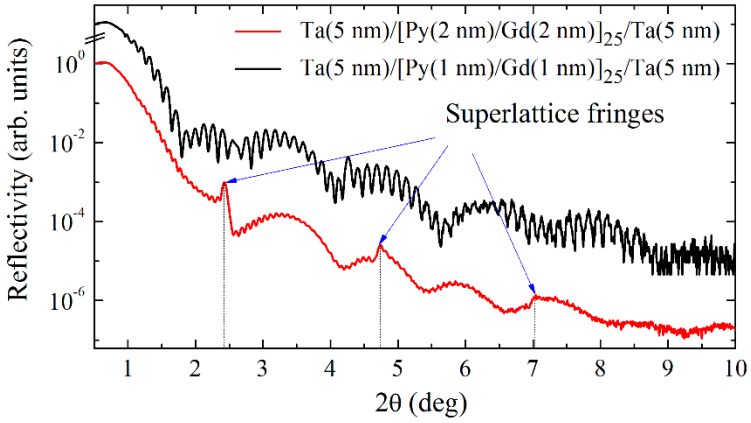

Figure 23 X-ray reflectivity curves for the $[Py(1\ nm)/Gd(1\ nm)]_{25}$ (black line) and $[Py(2\ nm)/Gd(2\ nm)]_{25}$ (blue line) films. Short-dashed lines illustrate the positions of the superlattice fringes for the latter film. Blue arrows point to the positions of the superlattices fringes for the $[Py(2\ nm)/Gd(2\ nm)]_{25}$ film. (After Ref. [128])

The temperature dependences of magnetization for the Py/Gd multilayers show that, for the $[Py(2\ nm)/Gd(2\ nm)]_{25}$ film, only thin core sublayers are not subjected to intermixing, whereas it can be considered that the $[Py(1\ nm)/Gd(1\ nm)]_{25}$ film consists of a homogeneous PyGd alloy. This observation is confirmed by an X-ray reflectivity measurement (Figure 23). For the film with 2-nm thick layers, much stronger superlattice fringes corresponding to the 3.95-nm periodic structure are observed.

The magnetization curves of the $[Py(2\ nm)/Gd(2\ nm)]_{25}$ multilayer measured at 10 K (black dots) and at the compensation temperature (blue dots) are shown in Figure 24(a). Importantly, even at the compensation temperature, the magnetization of the film is not zero. Furthermore, the magnetization curve does not pass through the origin in zero magnetic field. At the compensation temperature, the magnetization rises linearly in magnetic fields up to 70 kOe, whereas at 10 K, a complete saturation of magnetization is achieved already in a very small magnetic field (below 50 Oe). At 10 K, the magnetization

experiences an abrupt rise at a magnetic field of 16 kOe [Figure 24(b)], similarly to the one demonstrated by the PyGd bilayers [Figure 21(a)].

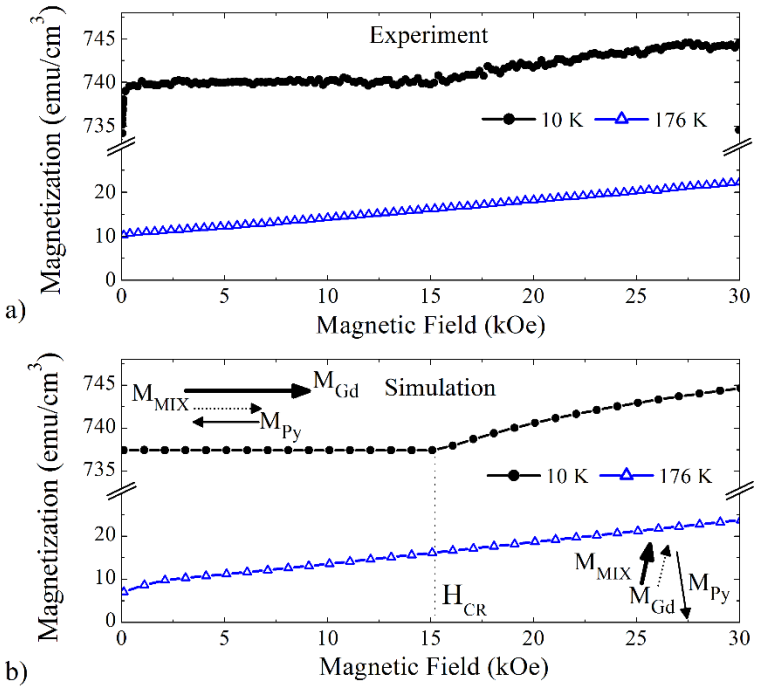

Figure 24 (a) Experimental and (b) simulated magnetization curves for the [Py(2 nm)/Gd(2 nm)]$_{25}$ film measured at 10 K (black dots and lines) and at the compensation temperature (blue open triangles and lines). Arrows illustrate the direction of magnetizations in the Py-core (thin solid arrow), Gd-core (thick solid arrow), and Mix (dashed arrow) sublayers at 10 K and 176 K, respectively, the magnetic field is applied horizontally. (After Ref. [128])

Knowing the estimated thicknesses of the Py-core and Gd-core sublayers [Figure 22(b)], the magnetization curves of the [Py(2 nm)/Gd(2 nm)]$_{25}$ multilayer can be modeled micromagnetically. Figure 24(b) presents simulated the magnetization curves obtained for 10 K (green line) and 176 K (black line). Micromagnetic parameters used for the simulation are $A_{MIX} = A_{Py} = 1.5\times10^{-7}$ erg/cm, $M_{Py} = 810$ emu/cm^3. For $T = 10$ K, $A_{Gd} = 1.5\times10^{-7}$ erg/cm, $M_{MIX} = 861$ emu/cm^3, $M_{Gd} = 1600$ emu/cm^3. Based on the fact that

the Gd-core sublayers gain significant magnetic moment only below 75 K, it is assumed that the exchange stiffness and magnetization of the Gd-core sublayers is highly suppressed at 176 K, *i.e.*, $A_{Gd} = 0.1\times10^{-7}$ erg/cm, $M_{Gd} = M_{MIX} = 116$ emu/cm^3. The simulated 10-K magnetization curve shows that, in a magnetic field below 15.5 kOe, the magnetizations of the Gd-core and Mix sublayers are pointed along the magnetic field, while the magnetization in the Py-core sublayers are opposite to the field. When the magnetic field exceeds $H_{CR} = 15.5$ kOe, the magnetization in the very first Py layer, which is affected the least by intermixing, rotates to align along the magnetic field. This yields an exchange-spring twist of the magnetization near the bottom surface of the film similarly to the one observed in the PyGd bilayers. The rest of the film preserves antiparallel magnetization alignment along the magnetic field. In order to minimize the total energy at 176 K, when the magnetic moment of the Gd-core/Mix sublayers compensates that of the Py-core sublayers, the corresponding magnetizations tend to align perpendicular to the magnetic field, at the same time, being almost antiparallel to each other (non-collinear configuration). Again, as it was mentioned earlier, the magnetic structure of the very top Py and the very bottom Gd layers is different. Namely, the thicknesses of these Py-core and Gd-core sublayers are 1.25 nm instead 0.5 nm. Basically, it breaks the symmetry of the magnetic structure, and consequently, the magnetizations near the surfaces are at smaller angles with respect to the magnetic field than the magnetization inside the multilayer. To some extent, this configuration is similar to the twisted state predicted by Camley.[116, 162-164]

IV.4.2 Magnetotransport data and analysis

Although the simulated and experimental magnetization curves at 176 K demonstrate very similar behavior, they do not allow to determine conclusively the magnetic configuration of the $[Py(2\ nm)/Gd(2\ nm)]_{25}$ film in the vicinity of the compensation temperature. Electronic transport measurements, on the other hand, are more sensitive to the distribution of the magnetization inside the films and its response to the applied magnetic field. Figure 25 and Figure 26 summarize the results of transport measurements for both $[Py(1\ nm)/Gd(1\ nm)]_{25}$ and $[Py(2\ nm)/Gd(2\ nm)]_{25}$ films conducted for different magnetic fields and temperatures. First, Figure 25(a) shows the temperature dependences of the resistance for the $[Py(1\ nm)/Gd(1\ nm)]_{25}$ film measured in the 1-kOe (black line) and 100-kOe (orange line) magnetic fields applied longitudinally. These measurements show that the magnetoresistance changes sign near 40 K. Indeed, Figure 26(a) illustrates that both longitudinal and transverse magnetoresistance are negative at 50 K while they are positive at 10 K. Second, the same temperature [Figure 25(b)] and magnetic-field [Figure 26(b)] dependences for the $[Py(2\ nm)/Gd(2\ nm)]_{25}$ film indicate that the magnetoresistance changes the sign twice: around 20 K and, surprisingly, in the vicinity of the compensation temperature. Again, the magnetoresistance is positive at 200 K. In the vicinity of the compensation temperature, the magnetization rotates with respect to the magnetic film and the current, which leads to a change in the anisotropic magnetoresistance. Within the 150–180 K temperature range, transverse resistance increases while the longitudinal resistance decreases when the amplitude of the magnetic

field is increased. Similarly to the [Py(1 nm)/Gd(1 nm)]$_{25}$ film, the magnetoresistance of the [Py(2 nm)/Gd(2 nm)]$_{25}$ film is negative at 50 K and becomes positive again at 10 K.

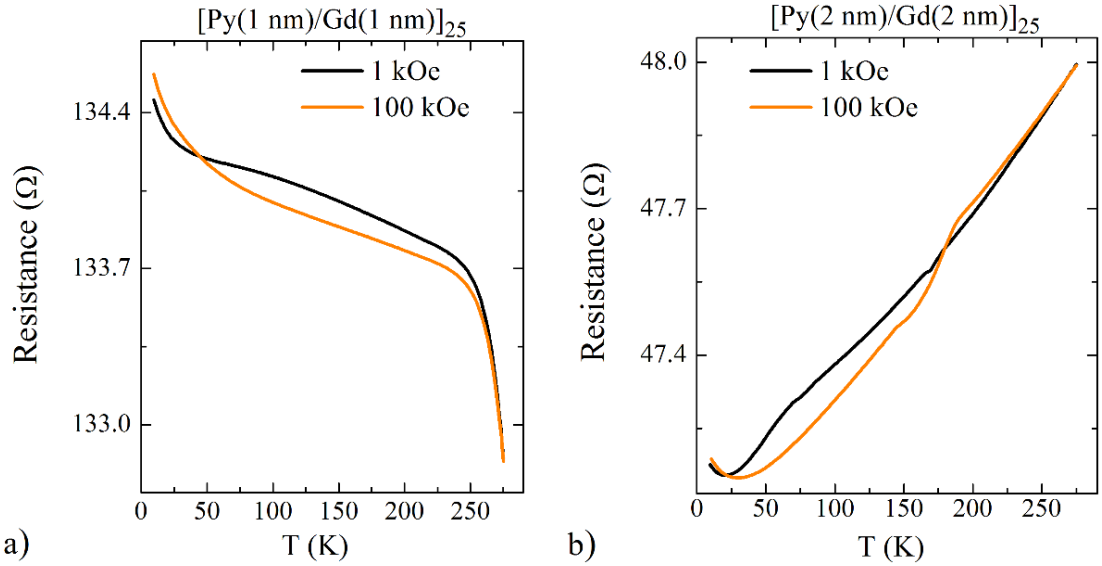

Figure 25 Temperature dependences of the resistance measured in 1 kOe (black line) and 100 kOe (orange line) for the (a) [Py(1 nm)/Gd(1 nm)]$_{25}$ and (b) [Py(2 nm)/Gd(2 nm)]$_{25}$ films. (After Ref. [128])

The anisotropic magnetoresistance is responsible for an interesting step-like change in the resistance observed at 10 K in the 16-kOe magnetic field [Figure 26(b)]. For the longitudinal resistance, it is an increase, and for the transverse resistance, it is a decrease. These steps are an additional evidence that the magnetization of the first Py layer rotates and aligns along the magnetic field. This rotation provides an abrupt rise of the magnetization at 10 K for 16 kOe [Figure 24] as discussed previously. Similar changes of the resistance related to the nucleation of an in-plane domain-wall have been reported previously for Fe/Gd[155, 156] and Co/Gd[157] systems.

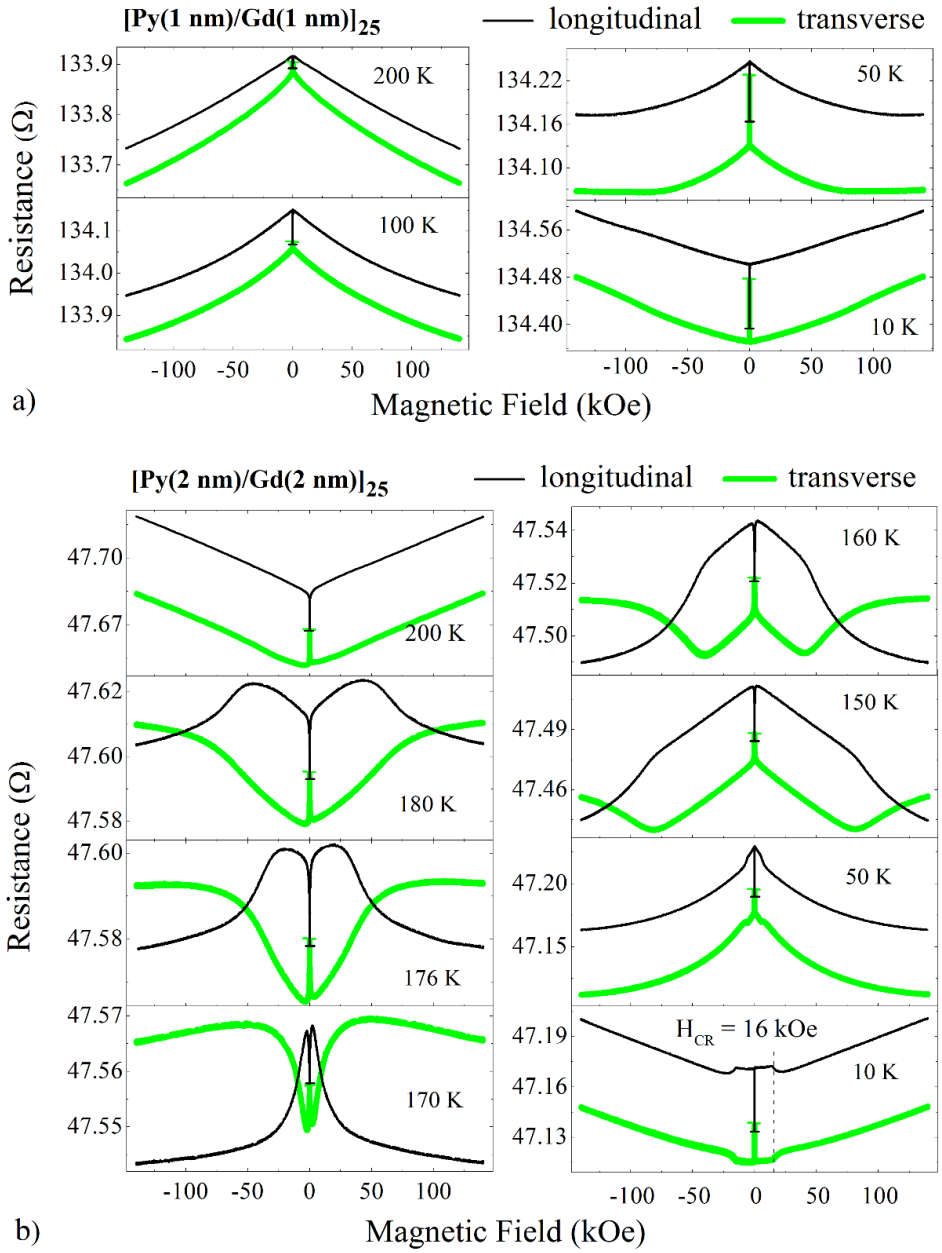

Figure 26 Resistance of the (a) [Py(1 nm)/Gd(1 nm)]$_{25}$ and (b) [Py(2 nm)/Gd(2 nm)]$_{25}$ films as a function of the longitudinal (black lines) and transverse (green lines) magnetic field. (After Ref. [128])

To define the orientation of the magnetizations in the [Py(2 nm)/Gd(2 nm)]$_{25}$ multilayer and to disentangle the contribution of the anisotropic magnetoresistance from

that of the ordinary and giant magnetoresistances, the angular dependences of the resistance were measured in different magnetic fields. Due to the anisotropic magnetoresistance, the resistance of the stripe reaches a minimum when the magnetizations in the layers are perpendicular to the direction of the current flow, and a maximum when the magnetizations are parallel or antiparallel to the current flow. As an example, the angular dependences of the resistance measured in 10 kOe at 174 and 176 K have minima at 90° and 87°, respectively (Figure 27). It means that in these orientations, the magnetizations in the Py/Gd multilayers are perpendicular to the current. Additionally, in these orientations, the magnetic field is perpendicular to the current, hence, the magnetizations are parallel to the 10-kOe magnetic field at 174 and 176 K (collinear configuration). When the magnitude of the magnetic field is increased, the minima begin to shift. This indicates that the magnetizations in the Gd-core/Mix and Py-core sublayers rotate with respect to the applied magnetic field. As an example, in the 30-kOe magnetic field, the minimum is at 52° at 174 K, and at 15° at 176 K. Hence, at 174 K and 176 K, the angles between the magnetization and the 30-kOe magnetic field are 38° and 75°, respectively. The curves measured in the 70-kOe magnetic field have minima at around 0°. This means that the magnetizations are almost perpendicular to the high magnetic field.

It is noteworthy that the shape of some angular dependences is not completely sinusoidal, and the amplitude of the angle-dependent parts of the curves are different at different temperatures. For example, at 174 K, this amplitude is 23 mΩ in 10 kOe, 7 mΩ in 30 kOe, 19 mΩ in 70 kOe. This behavior can be attributed to formation of a domain structure. The magnetizations in different domains can be mirrored with respect to the

magnetic field. The averaging of the resistance produced by different domains may cause the reduction in the anisotropic magnetoresistance.

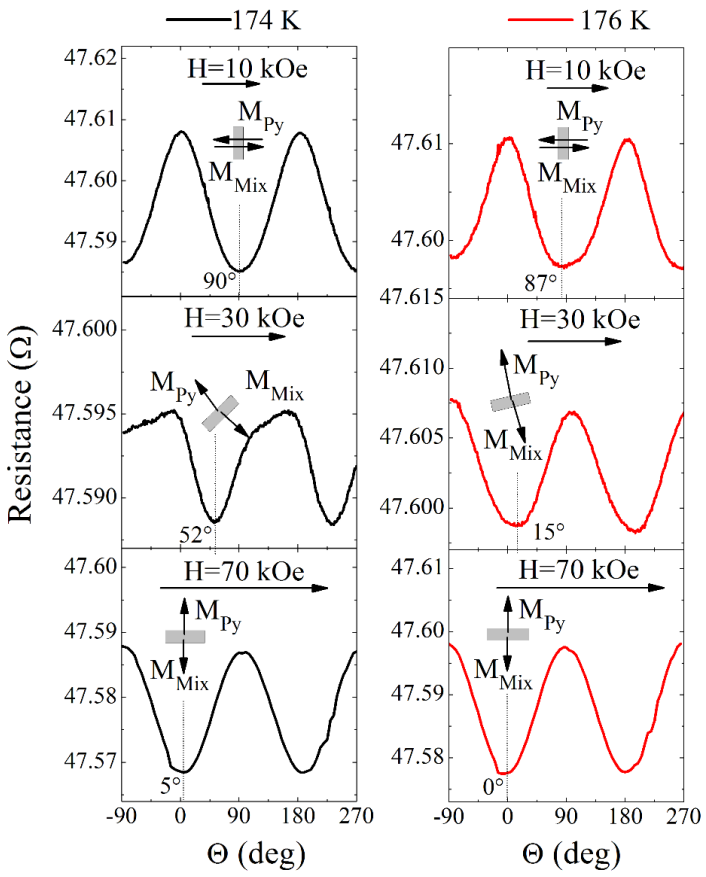

Figure 27 Angular dependences of the resistance for the [Py(2 nm)/Gd(2 nm)]$_{25}$ multilayer measured at 174 K and 176 K in 10 kOe, 30 kOe, and 70-kOe magnetic fields. A zero-angle orientation corresponds to an orientation where the long edge of the stripe is along the magnetic field. The small insets near each curve depict the orientations of the stripe where the resistance reaches minimum. (After Ref. [128])

To map the directions of the magnetizations at different temperatures and magnetic fields the angular dependence of the resistance was measured in 10-, 30-, 50-, 70-kOe magnetic fields in the 160–190 K temperature range. The positions of the resistance minima define the angle α between the magnetic field and the axis along which the

magnetizations in the Gd-core/Mix and Py-core sublayers are aligned. The $\alpha(H, T)$ dependence measured in different magnetic fields, H, and temperatures, T, is shown in Figure 28(a). The same $\alpha(H, T)$ dependence was modeled micromagnetically [Figure 28(b)].

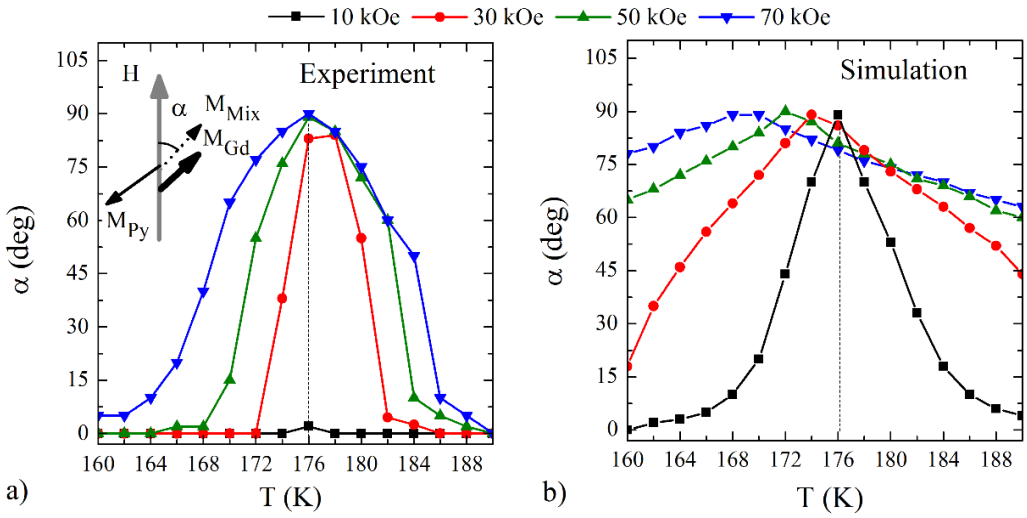

Figure 28 (a) Experimental and (b) simulated temperature dependences of the angle between the magnetic field and the line along which the magnetizations in the [Py(2 nm)/Gd(2 nm)]$_{25}$ film are predominantly aligned. (After Ref. [128])

The most striking and unexpected result provided by the experimental $\alpha(H, T)$ dependence is that, in a 10-kOe magnetic field, the collinear magnetization configuration is stable even at the compensation temperature, and non-collinear magnetization configurations appear only in higher magnetic fields. The occurrence of a transition from the collinear to non-collinear magnetization configurations even at the compensation temperature cannot be explained by the proposed micromagnetic model. It is not clear why the transition does not lead to a horizontal plateau in the magnetization curve at the compensation temperature [Figure 24(a) 176 K curve]. Additionally, the experimental

$\alpha(H, T)$ distribution is very narrow [Figure 28 (a)]. That is, in contrast to the simulations [Figure 28(b)], the experiment does not show a non-collinear configuration for 70 kOe at temperatures 15 K above or below the compensation temperature.

IV.4.3 Discussion of micromagnetic-model validity

The unusual phenomena observed in the vicinity of the compensation temperature for the [Py(2 nm)/Gd(2 nm)]$_{25}$ multilayer, namely, the change in the magnetoresistance sign, the existence of the transition from collinear to non-collinear configurations, and the unexpectedly narrow $\alpha(H, T)$ distribution, can be explained by inhomogeneity of the sample structure. Importantly, the magnetic and atomic structures of the film were modeled as a combination of the Mix, Py-core, Gd-core sublayers, and the thicknesses of these sublayers are the same throughout the film. However, it is possible that the roughness accumulation may very well change the amount of the intermixing over the thickness of the multilayer. This may yield the top layers of the [Py(2 nm)/Gd(2 nm)] multilayer to more resemble the PyGd alloy. In this case, it is conceivable that the magnetization in this top part is Gd-aligned (magnetic moment of Gd exceeds that of Py) even above 176 K, while the magnetization in the bottom part of the film is still Py-aligned (magnetic moment of Py exceeds that of Gd). Then, above 176 K, one can expect an in-plane domain-wall somewhere inside the film. An increase in the external magnetic field makes this domain-wall narrower, which leads to an increase in the scattering, and consequently, a positive magnetoresistance. Second, the compensation observed at 176 K is not due to the equality of magnetic moments of the Mix/Gd-core and Py-core sublayers. The compensation occurs because the Gd-aligned magnetic moment of strongly intermixed top part of the

film becomes equal to the Py-aligned magnetic moment of its bottom part. This yields a narrow $\alpha(H, T)$ distribution as it is observed in the experiment. Additionally, such different thickness-dependent intermixing may result in a thickness-dependent variation of the compensation temperature, which in turn would explain the remaining non-zero magnetization at 176 K.

It is believed that the change in the magnetoresistance sign at low temperatures for both $[Py(2\ nm)/Gd(2\ nm)]_{25}$ and $[Py(1\ nm)/Gd(1\ nm)]_{25}$ films is caused by the same mechanism. It is not expected that this sign change is due to an in-plane domain-wall. Based on the magnetic-field dependence of the resistance for the $[Py(2\ nm)/Gd(2\ nm)]_{25}$ film at 10 K [Figure 26(b)], the magnetoresistance is positive even in magnetic fields lower than the nucleation field of the domain wall attributed to the rotation of the magnetization in the first Py layer. Besides, nucleation of any in-plane domain wall in the $[Py(1\ nm)/Gd(1\ nm)]_{25}$ film is not expected. A similar change in the magnetoresistance sign was observed in a GdNi alloy.[165] The effect was attributed to magnetic polarons induced by Gd.

IV.4.4 Measuring effective exchange stiffness of Py/Gd multilayers

Based on the analysis of the temperature dependence of magnetization, it was concluded that the Gd-core sublayers become ferromagnetic only below 75 K [Figure 22(a)]. It is expected that only a short-range exchange exists in the Gd-core sublayers above this temperature. This assumption is then implicitly used for simulating magnetization curve at the compensation temperature. Namely, it was assumed that $A_{Gd} = 0.1\times10^{-7}$ erg/cm. It is peculiar that the magnetic order inside the Gd layers can

change so significantly on the scale of 2 nm. To investigate this effect more systematically, Py(50 nm)/[Py(t)/Gd(t)]$_{25}$, t = 1 or 2 nm, films were fabricated. The goal was to understand how the effective exchange stiffness of the [Py(t)/Gd(t)]$_{25}$ stacks changes upon temperature increase.

The total magnetic moment of the [Py(t)/Gd(t)]$_{25}$ stacks is Gd-aligned below 275 K for t = 1 nm and below 176 K for t = 2 nm. Due to the antiferromagnetic coupling, this moment tends to be antiparallel to the magnetic moment of the 50-nm thick Py layer adjacent to the stack. Since the effective exchange stiffness of the stack is expected to be much smaller than that for Py, applying magnetic field leads to an exchange-spring-like rotation of the magnetization in the entire stack, and the total magnetic moment of the [Py(t)/Gd(t)]$_{25}$ stack aligns along the magnetic field. Figure 29(a) illustrates the magnetization distribution over the thickness of the Py(50 nm)/[Py(2 nm)/Gd(2 nm)]$_{25}$ film at 10 K in high and low magnetic fields. As a model, the entire [Py(t)/Gd(t)]$_{25}$ stack can be considered as a homogeneous layer with some effective exchange stiffness, A_{GdPy_Eff}. This effective layer is antiferromagnetically coupled to the 50-nm thick Py layer. Applying the model for fitting the experimental magnetization curves of the Py(50 nm)/[Py(t)/Gd(t)]$_{25}$ film enables estimating A_{GdPy_Eff} at different temperatures. As examples, the fits conducted for the magnetization curve measured 10 and 100 K are shown in Figure 29(b) and (c), respectively. Figure 29(d) summarizes A_{GdPy_Eff} at different temperatures obtained from the fitting.

At 10 K, the Py/Gd stacks of both films can be characterized by the same effective exchange stiffness, $A_{GdPy\_Eff} = 1.5\times10^{-7}$ erg/cm. At 100 K, the effective exchange stiffness

of the [Py(1 nm)/Gd(1 nm)]$_{25}$ stack becomes equal to 4×10^{-8} erg/cm, while that for the [Py(2 nm)/Gd(2 nm)]$_{25}$ stack is 5 times smaller (8×10^{-9} erg/cm). This observation once again confirms that the inner portion of the Gd layers has a lower exchange stiffness and the Py layers are responsible for the enhancement of the magnetic order in the Gd layers.

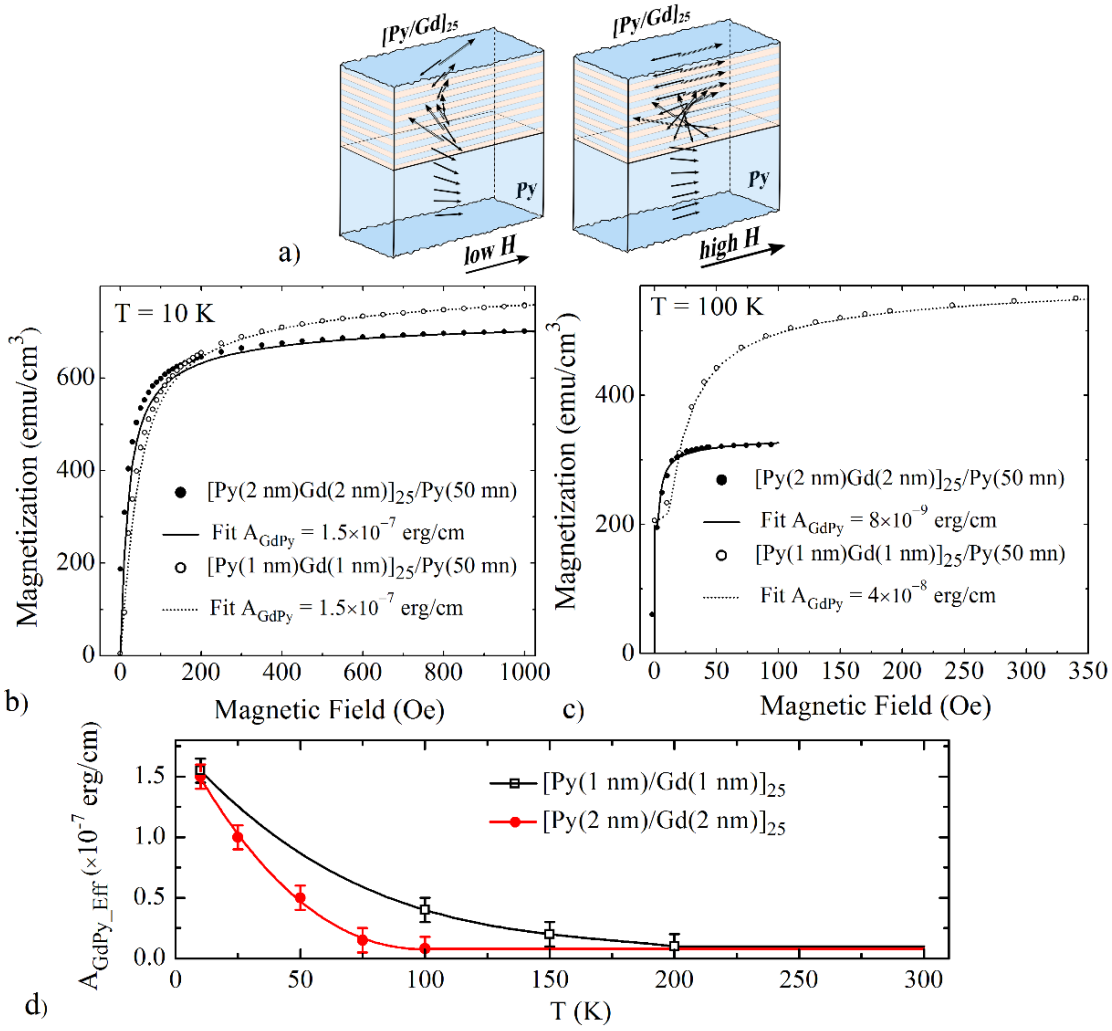

Figure 29 (a) The schematics of the in-plane domain-walls in Py(50 nm)/[Py(2 nm)/Gd(2 nm)]$_{25}$ in high and low magnetic fields. Magnetization curves of the Py(50 nm)/[Py(2 nm)/Gd(2 nm)]$_{25}$ (solid dot – experimental data, solid lines – fits) and the Py(50 nm)/[Py(1 nm)/Gd(1 nm)]$_{25}$ (open dots – experimental data, short-dashed line – fits) at (b) 10 K and (c) 100 K; (d) the effective exchange stiffness, A_{GdPy_Eff}, as a function of temperature for the [Py(1 nm)/Gd(1 nm)]$_{25}$ (black open rectangles) and [Py(2 nm)/Gd(2 nm)]$_{25}$ (red dots) control films. (After Ref. [128])

IV.4.5 Conclusions on magnetization reversal in Py/Gd multilayers

Analysis of the magnetization curves for the Py/Gd bilayers shows that due to proximity with Py, magnetic order of about 1 nm of the Gd layer adjacent to the Py layer is strongly enhanced. Micromagnetic simulations demonstrate that the magnetization reversal observed in the Py(50 nm)/Gd(4 nm) bilayers in 1.3 kOe is due to an exchange-spring-like twisting of the magnetization in the Gd layer. The exchange stiffness of the Gd layer and, hence, parameters of the twist can be controlled by inserting an ultrathin layer of Au between Py and Gd. Using a combination of magnetometry and magnetotransport measurements, the magnetic structures of the Py/Gd multilayers were determined. Based on the reduction in the Curie temperature, it was concluded that the $[Py(1\ nm)/Gd(1\ nm)]_{25}$ film is mostly composed of a PyGd alloy. Most likely, the $[Py(2\ nm)/Gd(2\ nm)]_{25}$ film is inhomogeneous over its thickness. Toward the bottom of the film, about 0.5-nm thick inner sublayers of the Py and Gd layers are not affected by the intermixing, whereas toward the top of the film, the Py and Gd layers are almost completely intermixed. The compensation observed at 176 K is due to equality of the magnetic moments in the majority of the film. The absence of the local compensation leads to a peculiar behavior of magnetization at the compensation temperature. Namely, using the angular dependences of resistance, it was shown that the non-collinear magnetization configuration is stable only in an unexpectedly narrow range of temperatures, and there is a transition from the collinear to non-collinear configurations in the 10-kOe magnetic field even at the compensation temperature. Most likely, the inhomogeneity of the $[Py(2\ nm)/Gd(2\ nm)]_{25}$ film's magnetic structure is responsible for an in-plane domain-

wall in the film at temperatures above 176 K, which leads to the change in the magnetoresistance sign at the compensation temperature. Analysis of the magnetization curves for the Py(50 nm)/[Py(t)/Gd(t)]$_{25}$ multilayers, where t is 1 or 2 nm, demonstrates that above 75 K, the exchange stiffness inside the Gd layers is reduced and the magnetic order changes drastically on the scale of 2 nm.

IV.5 Magnetization behavior of Py/Gd artificial-ferrimagnet microdisks

IV.5.1 Optimized micromagnetic model for simulating magnetizing in Py/Gd artificial-ferrimagnet microdisks

Magnetometry measurements show that for both [Py(2 nm)/Gd(2 nm)]$_{25}$ and [Py(1 nm)/Gd(1 nm)]$_{25}$ films, the coercive field does not exceed 10 Oe in the 10–200 K temperature range. This means that the anisotropy of these films is comparable to that of Py, which makes them a good choice for applications as a soft artificial ferrimagnet. It is noteworthy, the study also showed that the anisotropy becomes significantly higher if the thickness of the Gd layers increases.

The fact that the anisotropy of the [Py(2 nm)/Gd(2 nm)]$_{25}$ and [Py(1 nm)/Gd(1 nm)]$_{25}$ films is low indicates that the magnetic vortex may be a stable magnetization configuration for the microdisks composed of these artificial ferrimagnets. Even though the anisotropy of the [Py(2 nm)/Gd(2 nm)]$_{25}$ and [Py(1 nm)/Gd(1 nm)]$_{25}$ multilayers is non-zero, for the micromagnetic simulations of the microdisks, it was assumed to be exactly zero.

In addition to the low anisotropy, it was also demonstrated that the influence of material intermixing becomes significant for the [Py(2 nm)/Gd(2 nm)]$_{25}$ and

[Py(1 nm)/Gd(1 nm)]$_{25}$ films. Thus, due to the strong intermixing of Py and Gd, the [Py(1 nm)/Gd(1 nm)]$_{25}$ superlattice can be considered as a homogeneous film composed of a PyGd alloy. This model was adopted for micromagnetic simulations of the magnetization for the [Py(1 nm)/Gd(1 nm)]$_{25}$ disks. The study of continuous films using magnetometry showed that the magnetic and atomic structures of the [Py(2 nm)/Gd(2 nm)]$_{25}$ superlattice is more complicated. According to the estimates, only 0.5 nm of each Py and Gd layers is not subjected to intermixing, whereas the rest of the film is the PyGd alloy. Taking into account this magnetization profile over the [Py(2 nm)/Gd(2 nm)]$_{25}$ film thickness would lead to a very complicated micromagnetic model which would require a very small mesh, and hence, long calculation time. To avoid this, similarly to the micromagnetic model used for the [Py(1 nm)/Gd(1 nm)]$_{25}$ disks, it was assumed that the [Py(2 nm)/Gd(2 nm)]$_{25}$ disks are composed of a homogeneous material. Microscopically, the effective magnetization, M_{eff}, of the Py/Gd disks is expected to be equal to the magnetization of the corresponding control films at a given temperature. Once it is assumed that the disks are composed of a homogeneous material, the effective exchange stiffness of this material at different temperatures was considered to be equal to the effective exchange stiffness of the Py/Gd multilayers, A_{GdPy_Eff} [Figure 29(d)].

In summary, for a micromagnetic simulation at a given temperature, T, it was assumed that a disk is composed of an isotropic homogeneous material with magnetization $M_{eff}(T)$ and exchange stiffness $A_{GdPy\_Eff}(T)$. The simulations were conducted using a GPU-accelerated micromagnetic simulation program, mumax3.[166] The size of the mesh is 2.9 nm×2.9 nm in plane of the disk and 12.5 nm over its thickness.

IV.5.2 Magnetic vortices in Py/Gd artificial-ferrimagnet microdisks

For both multilayers compositions, M_{eff} is at a maximum at low temperatures. Magnetization curves for the etched $[Py(t)/Gd(t)]_{25}$ (t=1 or 2 nm) disks measured at 10 K are shown in Figure 30(a). Both curves correspond to the vortex-like behavior[133] (Figure 18) in low magnetic fields, *i.e.* the magnetization changes linearly with the field and the coercivity is negligibly small (the coercive fields are 0.5 and 2.5 Oe for t=1 and 2 nm, respectively). The micromagnetically-simulated curves shown in Figure 30(b), quantitatively and qualitatively resemble the experimental ones. According to the simulations, the vortex configuration is stable in the magnetic fields of up to 340 Oe for the $[Py(1\ nm)/Gd(1\ nm)]_{25}$ disks, and up to 580 Oe for the $[Py(2\ nm)/Gd(2\ nm)]_{25}$ disks. Due to an energy barrier separating the vortex and uniformly-magnetized states, the simulated and experimental loops have hysteretic regions in higher magnetic fields [Figure 30(a, b)].

The micromagnetic simulations show that because the disks' diameter is 1.5 μm and A_{eff} is low, increase or decrease in magnetic field causes the magnetic vortex to deform in addition to shifting. The deformation is significant in the magnetic field close to annihilation. The vortices are moon-shaped in magnetic fields below the annihilation fields [see schematics in Figure 30(b)]. When the magnetic field is ramped down from the saturation, the magnetization does not transform from a uniform state to a vortex state directly, but instead, two vortices appear. These vortices move toward each other and merge into a single vortex in 210 and 360-Oe magnetic fields for t=1 and 2 nm,

respectively [schematics in Figure 30(b)]. Only the vortex annihilation looks like a sharp transition.

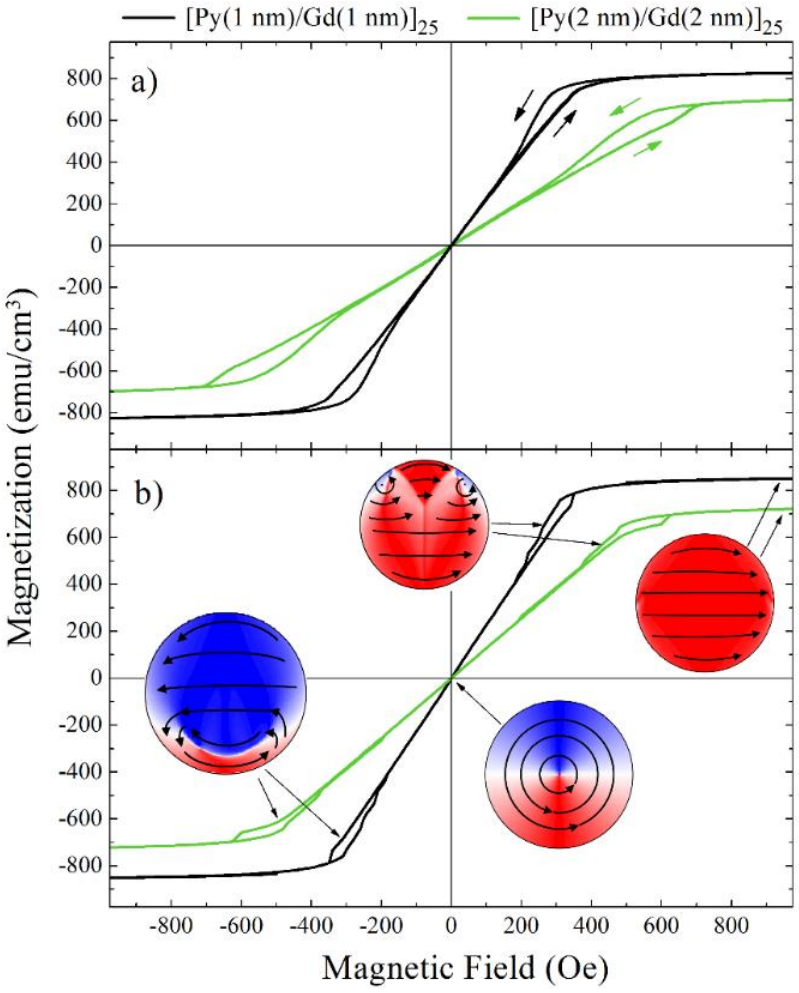

Figure 30 (a) Experimental (b) micromagnetically simulated hysteresis loops (10 K) for the etched $[Py(1\ nm)/Gd(1\ nm)]_{25}$ (black line) and $[Py(2\ nm)/Gd(2\ nm)]_{25}$ (green line) disks; (b) contains the schematics of magnetization configurations realized in the disks at different magnetic fields. (After Ref. [150])

To determine which magnetization configurations are realized at different temperatures, magnetization of the etched disk arrays was measured in a 100-Oe magnetic field while the temperature was slowly (1 K/min) swept from 300 to 10 K and back to

300 K [Figure 31(a)]. At the initial stage of the cooling down, the curves indicate the behavior almost identical to that demonstrated by the control films. Then, at 112 K for t=1 nm and 66 K for t=2 nm, a phase transition occurs and the magnetization begin to decrease when the temperature is decreased. At low temperatures, the magnetization is almost constant. When the temperature is ramped up, the magnetization decreases but not monotonically. For the $[\text{Py(1 nm)/Gd(1 nm)}]_{25}$ disks, the magnetization falls slowly until 143 K, and then the curve merges with the one obtained while cooling down the sample. A very similar decrease in the magnetization is demonstrated by the $[\text{Py(2 nm)/Gd(2 nm)}]_{25}$ disks in the initial stage of the warm-up, but right before the merging with the cool-down curve, the magnetization kinks up. The temperature dependences of the magnetization to demonstrate hysteretic behavior within the 40–160 K and 40–110 K ranges, for t=1 and 2 nm, respectively.

The temperature dependences of the disks' magnetization in the 100-Oe magnetic field were simulated micromagnetically [Figure 31(b)]. It is zero-temperature simulations without thermal field fluctuations, and any dependence on temperature is only introduced by temperature-dependent parameters, $M_{eff}(T)$ and $A_{eff}(T)$. This simplification is reasonable because the energy barrier separating single domain and vortex states, ΔE, is high for the 1.5-μm disks ($\Delta E >> k_B T$, k_B is Boltzmann constant, T is temperature). Hence, any fluctuation effects, such as a thermal excitation over an energy barrier,[167] are expected to be insignificant. The simulated curves demonstrate hysteretic behavior similar to the one observed in the experiment [Figure 31(a, b)]. The simulations reveal that the phase transitions observed in the experiment are due to the vortex nucleation and annihilation.

At the high temperatures, the disks' magnetization is low and the disks are in the uniformly-magnetized state. When the temperature is decreased, the disks' magnetization increases, and at a critical temperature, it becomes energetically favorable to nucleate vortices, thus minimizing the magnetic flux.

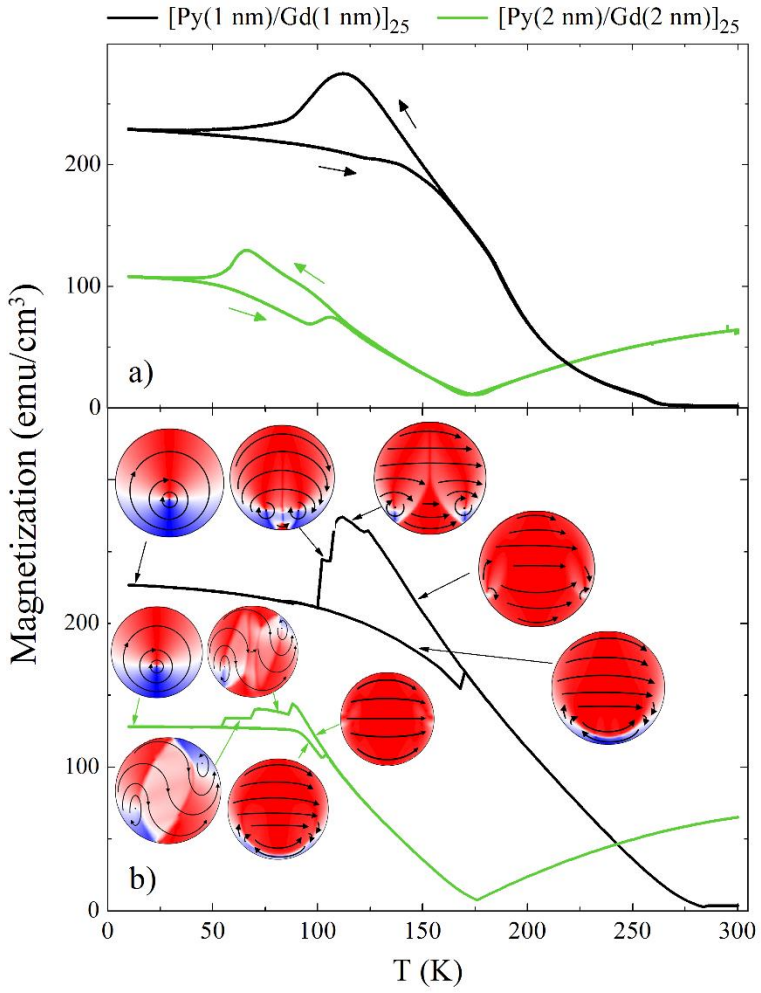

Figure 31 (a) Experimental (b) micromagnetically simulated temperature dependences of magnetization in the 100-Oe magnetic field for the etched $[Py(1\ nm)/Gd(1\ nm)]_{25}$ (black line) and $[Py(2\ nm)/Gd(2\ nm)]_{25}$ (green line) disks; (b) contains the schematics of magnetization configurations realized in the disks at different temperatures. (After Ref. [150])

Again, similarly to the nucleation processes observed at 10 K, the disks' magnetization does not switch from the uniformly-magnetized state to the single-vortex state directly; instead, the magnetization is stabilized in a series of intermediate states, some of which include various double-vortex configurations. Each transition between intermediate states causes an abrupt decrease of magnetization. Since the arrays consist of disks with slightly different diameters, the abrupt transitions observed in the simulations are smeared out for the experimental curves. According to the simulations, increasing the temperature causes the vortex core shifting from the center of the disk and its deformation. Eventually, the disks switch to the quasi-uniformly-magnetized state [see schematics in Figure 31(b)].

It is of a particular interest to investigate the stability of the vortex state at the temperatures which are within the thermal hysteresis ranges, *e.g.* at 115 K for the $[Py(1\ nm)/Gd(1\ nm)]_{25}$ disk array and 75 K for the $[Py(2\ nm)/Gd(2\ nm)]_{25}$ disk array. For this, the disks were cooled down to 10 K, and the magnetic field was set to 0 Oe. This procedure allowed to ensure that the vortex is the initial magnetic state for the disks. Then, the temperature was increased to 115 K and 75 K for the $[Py(1\ nm)/Gd(1\ nm)]_{25}$ and $[Py(2\ nm)/Gd(2\ nm)]_{25}$ disk arrays, respectively, and the array magnetization was measured while the magnetic field was ramped up from 0 Oe to 500 Oe and then cycled between 500 and -500 Oe [Figure 32(a)]. The experiments were simulated micromagnetically [Figure 32(b)]. For the $[Py(1\ nm)/Gd(1\ nm)]_{25}$ disk array, the magnetization shows the behavior identical to that observed for the array at 10 K, *i.e.* the magnetization rises linearly in low magnetic field and the hysteresis is present only in the

high fields. The virgin part of the magnetization curve measured between 0 and 500 Oe coincides with its main part (500 Oe → -500 Oe → 500 Oe) indicating that the vortex state is stable for these disks in low magnetic field. The simulated curve is in qualitative agreement with the experimental one. In contrast, the main part of the magnetization curve for the $[Py(2\ nm)/Gd(2\ nm)]_{25}$ disk array measured at 75 K demonstrates significant hysteretic behavior in low magnetic fields. The corresponding hysteresis curve has a double-waist shape, while its virgin curve demonstrates the typical vortex-like behavior. Moreover, the virgin magnetization curve passes outside the main hysteresis loop. Such an unusual behavior indicates that the vortex is stable at the virgin curve, but after the saturation of the disk magnetization, the magnetization does not switch back to the vortex state while the main hysteresis loop is measured. It was also observed that if the disk is demagnetized after measuring the main hysteresis loop, and after that, the magnetization is measured while the magnetic field is increased, the resulting curve goes within the main hysteresis loop and does not coincide with the virgin curve. It means that the (0,0) point at the M-H plane can correspond to two different magnetization states, one of which is the vortex. These observations can be explained if the vortex state for the $[Py(2\ nm)/Gd(2\ nm)]_{25}$ disk at 75 K is separated by a large energy barrier. That makes it extremely hard, or likely, even impossible to be accessed by changing the external magnetic field isothermally. The magnetic field dependence of magnetization for the $[Py(2\ nm)/Gd(2\ nm)]_{25}$ disk array was not completely reproduced in the simulation [Figure 32(b) green line]. It is possible that the fine magnetic structure within the $[Py(2\ nm)/Gd(2\ nm)]_{25}$ superlattice as well as its very low magnetic anisotropy must be

taken into account for an adequate modeling of the magnetization reversal for the corresponding disks.

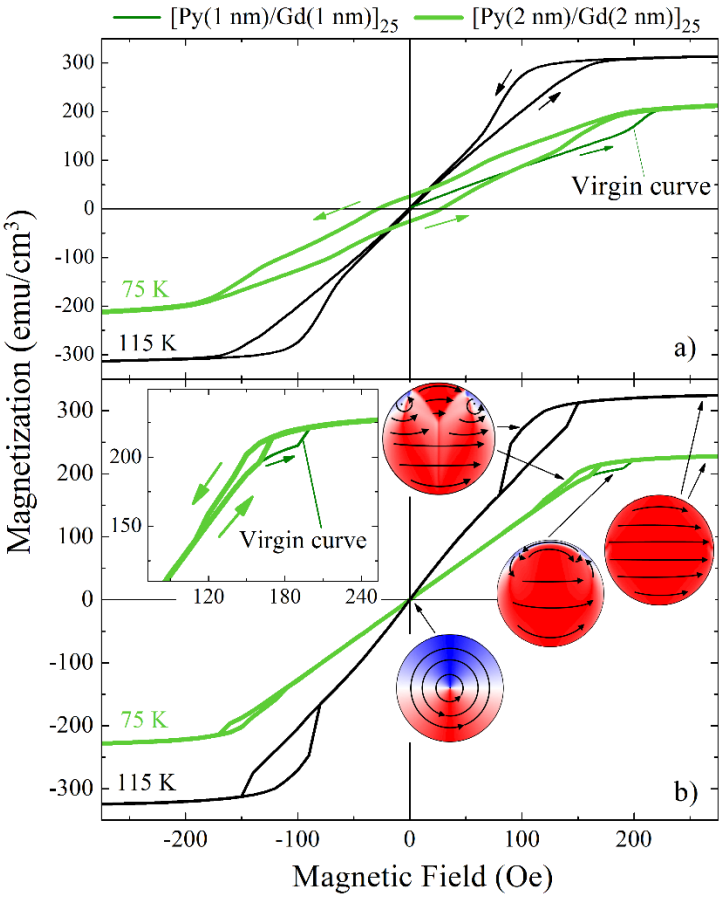

Figure 32 (a) Experimental (b) micromagnetically simulated hysteresis loops for the etched $[Py(1\ nm)/Gd(1\ nm)]_{25}$ disks at 115 K (black lines) and the etched $[Py(2\ nm)/Gd(2\ nm)]_{25}$ disks at 75 K (green lines); the virgin parts of the magnetization curves (from 0 to 500 Oe) are shown with thin lines while the main parts of hysteresis curves (500 Oe → -500 Oe → 500 Oe) with thick lines; (b) contains the schematics of magnetization configurations realized in the disks at different magnetic fields. The inset in the upper-left corner of (b) shows the hysteretic part of the loop for the $[Py(2\ nm)/Gd(2\ nm)]_{25}$ disks. (After Ref. [150])

An important factor that strongly affects magnetic properties of the Py/Gd superlattice disks is the intermixing of Py and Gd. Due to a shadow effect, the intermixing

is much more pronounced for the lift-off disks than that for the etched disks. Since the intermixing is almost complete for the $[Py(1\ nm)/Gd(1\ nm)]_{25}$ superlattice, the lift-off and etched $[Py(1\ nm)/Gd(1\ nm)]_{25}$ disks demonstrate almost identical temperature and field dependences. At the same time, due to the intermixing, the compensation temperature of the lift-off $[Py(2\ nm)/Gd(2\ nm)]_{25}$ disks is about 50 K higher than that for the etched disks and the corresponding control films. Although the same physical phenomena are observed in the lift-off $[Py(2\ nm)/Gd(2\ nm)]_{25}$ disks as that observed in the etched ones (vortex nucleation and annihilation), some quantitative parameters, such as the nucleation/annihilation fields and temperatures, are different for the $[Py(2\ nm)/Gd(2\ nm)]_{25}$ disks prepared using different fabrication techniques.

To get a direct confirmation that vortices nucleate in the Py/Gd superlattice disks at low temperatures, a series of underfocused Lorentz TEM images of the lift-off $[Py(1\ nm)/Gd(1\ nm)]_{25}$ disk on a Si_3N_4 membrane were acquired at different temperatures. The Lorentz TEM obtained at 152 and 98 K are shown in Figure 33(a) and (b), respectively. A white dot at the center of the disk in Figure 33(b), which appears when the temperature drops below 129 K, indicates the presence of a magnetic vortex. Figure 33(c) shows a temperature dependence of the magnetization measured in very low magnetic field (10 Oe), according to which the magnetization of the $[Py(1\ nm)/Gd(1\ nm)]_{25}$ disks switches to the vortex state below 180 K in the low magnetic field. Importantly, during the TEM imaging the temperature was swept continuously. The real temperature of the disk on the Si_3N_4 membrane can be very different from the readings of the microscope's

stage thermometer. This yields slightly different vortex nucleation temperatures detected by using Lorentz TEM and using magnetometry.

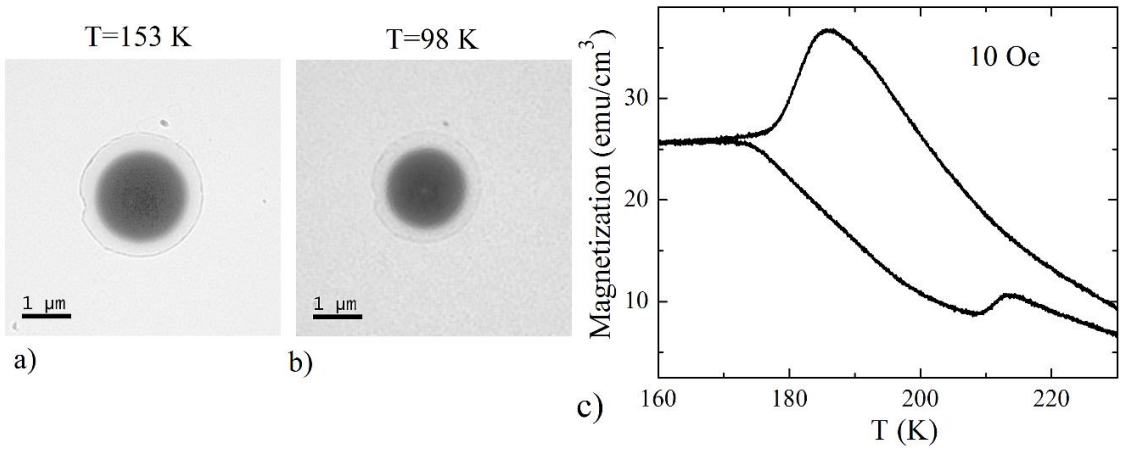

Figure 33 Underfocused Lorentz transition electron microscopy (TEM) images of a lift-off $[Py(1\ nm)/Gd(1\ nm)]_{25}$ disk on a Si_3N_4 membrane window acquired at 153 K (a) and 98 K (b). The image (b) noise was reduced by using averaging over 17-pixels-diameter circle. The white dot at the center of the disk at 98 K indicates the presence of magnetic vortex; (c) magnetization of the etched $[Py(1\ nm)/Gd(1\ nm)]_{25}$ disk array as a function of temperature measured in a small magnetic field (10 Oe). (After Ref. [150])

IV.5.3 Conclusions on magnetization behavior in Py/Gd artificial-ferrimagnet microdisks

It was observed that the 1.5-μm disks composed of the $[Py(t)/Gd(t)]_{25}$ (t=1 or 2 nm) artificial ferrimagnets experience a phase transition. The resulting temperature dependences of the magnetization of these disks measured in the 100-Oe magnetic field are hysteretic in narrow temperature ranges. Micromagnetic simulations revealed that these phase transitions are due to nucleation and annihilation of magnetic vortices which happen because the magnetic properties of the artificial ferrimagnet change significantly within the 10–300 K temperature range. It was shown that, at temperatures within the

hysteretic regions, the vortex state is stable only for the $[Py(1\ nm)/Gd(1\ nm)]_{25}$ disks, while for the $[Py(2\ nm)/Gd(2\ nm)]_{25}$ disks, the vortex is separated by an energy barrier and is unreachable from a non-vortex state. That is, at 75 K, it is impossible to nucleate the vortex in a $[Py(2\ nm)/Gd(2\ nm)]_{25}$ disk by changing external magnetic field isothermally, at the same time, if the disk with a magnetic vortex is brought to 75 K, the vortex does not annihilate until the disk magnetization is saturated.

CHAPTER V

PROBING FOR ODD-TRIPLET SUPERCONDUCTIVITY IN SUPERCONDUCTOR/FERROMAGNET HETEROSTRUCTURES

V.1 Introduction to Odd-triplet Superconductivity

V.1.1 Literature review of odd-triplet superconductivity

Developing new types of superconductors suitable for technological applications is one of the main challenges for modern physics. It could solve energy storage and transmission problems,[168, 169] create new memory devices and sensors,[170, 171] and give rise to a new era of electronics.[153, 172] Certainly, the main property expected from these superconductors is a high critical temperature, T_C. Ideally, they should remain superconducting even at room temperature. A discovery of superconductivity in compounds of copper and oxygen,[173] so-called "cuprates", was a tremendous breakthrough which has begun a new scientific direction, so-called, high-T_C superconductivity. Interestingly, early efforts to use the Bardeen-Cooper-Schrieffer (BCS) theory for an explanation of the cuprates high critical temperature showed that the electron-phonon coupling energy required for creating s-wave pairing[174] would be too high to be real. This unexpected disagreement with theory prompted researchers to consider other non-traditional mechanisms of superconductivity, that, in particular, triggered the insight that a d-wave pairing is realized in the cuprates.[175] As of today, many unconventional superconducting systems have been discovered (heavy-fermion, cuprates, organic, and iron-based superconductors).[176]

On one hand, a non-conventional pairing mechanism gives rise to a number of unique properties. These properties stimulate studies of unconventional superconductors. On the other hand, it is much easier to fabricate and work with well-studied conventional BCS superconductors[‡]. The question arises: is it possible to enrich the physics of these conventional superconductors? Since new physical effects can occur at the interface with materials possessing radically different properties, a lot of attention today is attracted to heterostructures containing traditional low-T_C superconductors and non-superconducting materials. In particular, it has been shown that new, non-conventional, mechanisms of superconductivity and new superconducting states may be realized in these heterostructures. Besides, a non-superconducting layer enables controlling the intrinsic properties of a superconductor, which can be used for developing new types of transistors and switches.[177, 178]

Historically, the study of superconducting heterostructures has begun with pioneer works done by Andreev[179] and de Gennes[180, 181] in which they considered proximity effects occurring at the interface between a superconducting (S) and a normal metal (N) layers. It was shown that the singlet Cooper pairs can penetrate into the N layer, which leads to two effects. First, the drain of the Cooper pairs affects the superconductor properties. In particular, it causes the reduction of the superconductor's T_C. The reduction of T_C becomes stronger with increasing the thickness of the N layer.[182] Second, the penetration of the Cooper pairs into the N layer results in propagation of the superconducting condensate

[‡] Conventional BCS superconductors are spin-singlet s-wave superconductors mediated by isotropic attractive interaction.

inside this layer, and hence, the normal metal start demonstrating superconducting properties. For the normal metal with a high concentration of non-magnetic impurities, the penetration depth of the Cooper pairs is of the order of $\sqrt{\upsilon_F^2 \tau \hbar / 3 k_B T}$, where τ is the relaxation time, k_B is Boltzmann constant, $\hbar$ is reduced Plank constant, υ_F is the Fermi velocity, and T is temperature.[183] This value can reach thousands of nanometers. In particular, the long penetration length is responsible for appearance of the Josephson current in S/N/S junctions.[184-186]

Surprisingly, if a normal layer (N) is substituted by a ferromagnetic (F) one in a superconducting heterostructure, it gives origin to a series of unique phenomena. First of all, since the electrons of a spin-singlet Cooper pair have oppositely-aligned spins, they belong to different energy bands in the F layer. Microscopically, it can be interpreted as emergence of an effective exchange field trying to align the spins, which breaks the Cooper pairs. Consequently, the penetration length of the singlet pairs into the F layer is much shorter than that for a non-magnetic layer. For a F layer with high density of impurities, the penetration length is $\sqrt{\upsilon_F^2 \tau \hbar / 3 H_{ex}}$, where H_{ex} is the exchange energy. That is the penetration length into a ferromagnet is a factor of $\sqrt{H_{ex}/k_B T_C}$ smaller than that for a normal metal. Since for an F layer with high Curie temperature, H_{ex} exceeds $k_B T_C$ by several orders of magnitude, the penetration length of a singlet Cooper pair into the F layer is of the order of a few nanometers only.

The destruction of a Cooper pair by an effective exchange field causes a moderate suppression of the critical temperature of a S layer adjacent to a F layer.[187] The manifestation of this suppression, *i.e.*, the dependence of T_C on the thickness of the non-

superconducting layer, is very different from the one observed for the S/N heterostructures. As it was mentioned previously, due to the exchange interaction, electrons of a Cooper pair belong to different energy bands, which means that, in the momentum space, the pair's net *k*-vector, Δk, is non-zero. That causes the superconducting condensate function to oscillate in space. As a consequence of this, T_C of the S/F heterostructure as well as critical current in the S/F/S Josephson junction demonstrate a non-monotonic, oscillatory dependence on the thickness of the F layer.[187-195]

Another interesting effect of the exchange interaction on superconductivity is a formation of non-singlet Cooper pairs at the S/F interface. Bergeret, Volkov and Efetov[196, 197] considered the pairing in the S/F heterostructure theoretically and showed that the exchange interaction should lead to an additional term in the Hamiltonian of the system written in the spin space. This additional term yields extra components in the condensate wave function which describe triplet pairing. Thus, under the condition that magnetization is uniform in the F layer, in addition to a singlet pairing, a triplet pairing with $S_F = 0$ arises, where S_F is a projection of the total spin of a Cooper pair on the direction of the magnetic field. Furthermore, if the magnetization is not homogeneous in the F layer, the triplet components with non-zero $S_F = \pm 1$ appear. Basically, in this case, a triplet pair cannot have a zero projection of the total spin on multiple directions simultaneously, which results in the excitation of spin-triplet pairing with non-zero S_F.

Remarkably, the triplet pairs formed at the S/F interface are very different from the p-wave pairs observed in other unconventional superconductors, for example, a layered perovskite oxide Sr_2RuO_4. According to the Pauli exclusion principle, the equal-

time correlation function must be odd under the exchange of the electrons composing a pair. For the triplet pairs, the spin part of the function is even, and hence, the space part must be odd. Consequently, the triplet pairs generated at the S/F interface must have a p-wave symmetry. However, the presence of nonmagnetic impurities would strongly suppress the p-wave condensate, which means the amplitude of the triplet component would be extremely low. Bergeret, Volkov and Efetov[196, 197] showed that another, so called, "Berezinskii" pairing mechanism[198] can be realized in the system. Namely, if the condensate wave function is odd in frequency, the equal-time correlation function is zero even if the orbital angular momentum of the pair is zero, hence, there is no contradiction with the Pauli exclusion principle. Thus, the odd-triplet pairs have s-wave symmetry, and hence, their scattering on nonmagnetic impurities does not break the superconductivity. Moreover, the odd-triplet pairs with $S_F = \pm 1$ can penetrate the F layer to much longer distances than singlet and triplet pairs with $S_F = 0$. For this reason, superconductivity with odd-triplet electron pairing with $S_F = \pm 1$ is also called long-range spin-triplet superconductivity.

Different types of heterostructures have been used for experimental studies of the long-range triplet superconductivity. Helical ferromagnets, mostly Ho, are used for creating non-collinear magnetization in the heterostructures consisting of a single F layer.[199-201] Along with the S/F heterostructures, so-called "superconducting spin valves (SV)", which consist of two different ferromagnetic layers, have gained popularity among experimentalists. The ferromagnetic layers can be located on one side from the S layer, *i.e.*, S/F1/F2, or on both, symmetrically with respect to the S layer, *i.e.*, F1/S/F2. The spin

mixing in these SVs is achieved by creating non-collinear magnetization configuration in the F1 and F2 layers.

Along with a variety of heterostructures, different experimental techniques have been applied for studying the odd-triplet superconductivity.[202] First of all, since odd-triplet pairs can penetrate excessive distance in the ferromagnetic layers, it must give rise to non-vanishing Josephson current in the S1/F1/F2/S2 junctions.[203-205] Robinson *et al.*[205] studied a Josephson effect in a junction which contained a homogeneous ferromagnetic Co barrier symmetrically coupled to Ho layers. The conical spin structure in Ho layers provides a spin-active interface which is responsible for generation of long-range triplet pairs. Based on the dependence of the critical current on the thickness of the Co layer, it was shown that the coherence length of the triplet pairs in the Co layer is larger than 10 nm, which is comparable with the coherence length in non-magnetic metals. In a work by Khaire *et al.*,[204] magnetic inhomogeneity responsible for generation of triplet pairs was provided by a thin layers of weakly-ferromagnetic PdNi and CoNi. Again, they showed that for a junction in which these active layers are inserted between the superconductor and another ferromagnetic (Co) layer, a maximum supercurrent decreases much slower with increasing the thickness of the Co layer than that for a junction without these spin-active layers. In both works a conventional BCS superconductor (Nb) was used as the S layer.

Second, it was shown that proximity with a ferromagnet strongly affects the density of states (DOS) of electrons in a superconducting heterostructure.[206-210] Kontos *et al.*,[211] using tunneling spectroscopy, measured the DOS in the heterostructure with a single, homogeneously magnetized F layer. Their tunneling junctions consist of two

stripes deposited using shadow masks; the bottom stripe is Al which was quickly-oxidized for creating a tunnel barrier, and the top stripe is a PdNi layer attached to a thick Nb reservoir. It was shown that the shape of tunneling spectra changes significantly with the increase in the thickness of the PdNi layer. This indicates that the superconducting condensate experiences transition from a 0-state to a π-state. That is, in a superconducting SV, the superconducting order parameter oscillates in the ferromagnetic layer and can take any values depending on the ferromagnet properties (exchange stiffness, magnetization, and thicknesses of the F and S layers). In some sense, Kontos' experiment demonstrated the full power of S/F heterostructures, namely, proximity with a ferromagnet brings an additional degree for controlling the superconductivity.

In addition, the measurement of the electronic DOS can be used for a clear-cut detection of the long-range pairing occurring in the superconducting SVs with inhomogeneous magnetization. Specifically, theory predicts that the generation of the pairing should lead to a zero-energy peak in the dependence of the DOS on energy near the Fermi surface.[212, 213] Bernardo *et al.*[199] performed scanning tunneling spectroscopy of the Nb/Ho/Nb multilayer. In contrast to the work by Kontos *et al.*,[211] in which the object of study was a heterostructure with a nominally uniformly-magnetized ferromagnetic layer, the spin structure of Ho is intrinsically inhomogeneous. This gives rise to a generation of odd-triplet pairs with $S_F = \pm 1$ at the Nb/Ho interface, which, in turn, causes the dependence of tunneling conductance versus bias voltage to demonstrate double-peak spectra predicted by theory. The inhomogeneity of magnetization in the Ho layer is controlled by applying relatively high magnetic field (1 kOe), which complicates the

interpretation of the spectra. Unfortunately, as of today, there are no reports about successful tunneling spectroscopy performed on a superconducting SV in which the non-collinearity of the magnetization is controlled by a relatively low magnetic field.

Finally, one of the manifestations of the interaction between a superconductor and a ferromagnet is that the critical temperature of a superconducting SV (S/F1/F2 or F1/S/F2) depends on the mutual orientation of the magnetizations in the F1 and F2 layers. Theoretical investigation of this phenomenon was performed for F1/S/F2[214, 215] and S/F1/F2[216, 217] SVs based on the analysis of a linearized Usadel equation for the case when the thickness of the superconducting layer is smaller than or comparable to the coherence length of the superconductor. First, it was shown that the critical temperature of the SV with the parallel magnetizations in the F1 and F2 ($T_{\uparrow\uparrow}$) is lower than the critical temperature of the SV with the antiparallel configuration of the magnetizations ($T_{\uparrow\downarrow}$), *i.e.*, $T_{\uparrow\uparrow} < T_{\uparrow\downarrow}$. This phenomenon is called a "standard superconducting SV effect", and it was observed in many experiments.[218, 219] Physical interpretation of this effect is straightforward: because singlet Cooper pairs have antiparallel spins, the parallel alignment of magnetization makes the superconducting condensate less stable, and hence, the superconductivity is suppressed. The second important prediction of the theory is less intuitive: For some ratios of the superconducting and ferromagnetic layers' thicknesses, the absolute minimum of T_C is achieved when the magnetizations in the F layers are perpendicular to each other, *i.e.*, $T_{\uparrow\rightarrow} < T_{\uparrow\uparrow}$ and $T_{\uparrow\rightarrow} < T_{\uparrow\downarrow}$. The explanation of the phenomenon is as follows. Due to the non-collinearity of the magnetizations, long-range triplet pairs are excited at the S/F interface. They penetrate the ferromagnets over a much

longer distance than singlet or triplet pairs with $S_F = 0$. This, in turn, causes a depletion of the carriers in the S layer which leads to a suppression of T_C. Basically, this phenomenon is similar to the one observed in S/N heterostructures,[182] where an increase of the N layer thickness yields a decrease of the T_C. In case of the superconducting SVs, the phenomenon is often interpreted as a drainage of carriers caused by the generation of long-range triplet pairing. According to the theory, manipulation of the magnetization in a superconducting SV can cause a complete suppression of the superconductivity, *i.e.*, with certain non-collinearity of the magnetizations, the SV is not superconducting even at zero temperature.

V.1.2 Challenges of studying odd-triplet superconductivity

In theory, the dependence of T_C on the mutual orientation of the magnetizations in a superconducting SV enables complete suppression of the supercurrent in a wide range of temperatures.[188, 217] However, numerous experimental studies of the superconducting SV effect revealed that a value of ΔT_C caused by this switching is usually of the order of few millikelvins,[201, 220-238] which is much smaller than the T_C-spread of superconducting transitions for the valves under studies. A legitimate question arises: is this tiny ΔT_C due to the superconducting SV effect, or are there some other phenomena occurring in a superconducting SV that can provide the same magnitude of ΔT_C?

It is necessary to take a close look at how the non-collinearity of magnetization is controlled in typical superconducting SVs. There are two standard approaches. First, many researchers use well-studied magnetic heterostructures in which the mutual orientation of the magnetizations in the F layers strongly depends on the amplitude of the applied magnetic field and its history. With these SVs, the angle between the magnetizations in

the F layers can be controlled by changing the external magnetic field in a certain sequence.[201, 220-233] For example, Gu *et al.*[233] used a sandwich consisting of a Nb layer placed between two Ho layers which have different thicknesses. Because of the thickness-dependent anisotropy of the Ho layers, these layers undergo magnetization reversal in different magnetic fields which provides step-like features in the SV hysteresis loop. The authors claimed that applying and then removing magnetic field enables establishing any magnetization configuration in the valve: parallel, antiparallel or spin-spiral. They showed that T_C for the spin-spiral and antiparallel states are respectively 700 and 400 mK higher than T_C for the parallel state. Another example demonstrating that the magnetizations can be controlled by the amplitude of externally-applied magnetic field is a work by Leksin *et al.*[227] Their CoO_X/Fe/Cu/Fe/In valve consisted of two ferromagnetic Fe layers, the magnetization in one of these layers was pinned by the antiferromagnetic CoO_X. It was assumed that the magnetization in the other, free Fe layer is rotated coherently by magnetic field. Consequently, tuning the field between 100 and -100 Oe provides control over the angle between the magnetizations. The authors discovered that depending on the thickness of the free Fe layer, direct ($T_{\uparrow\downarrow} > T_{\uparrow\uparrow}$) or inverse ($T_{\uparrow\downarrow} < T_{\uparrow\uparrow}$) standard SV effects occurs.

Another widely used approach for controlling the angle between the magnetizations in the superconducting SVs consists of pinning magnetization of one the ferromagnetic layers by biasing it with an antiferromagnet (AF), whereas the magnetization in the other, free F layer is controlled by rotating the valve in a small in-plane magnetic field.[234, 236-238] The amplitude of the field must be sufficiently high to reverse the magnetization in the free layer but low enough not to brake the pinning of

magnetization in the fixed layer. For example, Flokstra *et al.*[237] measured angular dependences of resistance for the Co/Nb/Co/IrMn/Co SV at different temperatures within the T_C-spread of the $R(T)$ curve by rotating the SV in 200-Oe magnetic field. They observed that the resistance increases when the magnetizations in the Co layers are perpendicular to each other. The authors attributed this increase to the carrier drainage from the S layer caused by the formation of the long-triplet pairs at the Nb/Co interfaces.

Both approaches, with and without rotation of the SVs, have advantages and disadvantages. For example, controlling magnetization by changing the amplitude of the field is required for experimental set-ups that are not compatible with a rotator (mK-temperature transport measurements, low temperature Kerr effect, SQUID magnetometry). Since the SV position is fixed with respect to the thermometer and dewar walls, more reliable readings of temperature can be obtained. The main disadvantage of controlling the SV with magnetic field is that the superconductivity and magnetic field are antagonistic to each other, and even for a superconducting layer, which is not in proximity to a ferromagnet, T_C is strongly suppressed by the magnetic field. In principle, using this technique, it is impossible to disentangle the T_C-suppression caused by a proximity with a ferromagnet from that caused by the magnetic field.

Undoubtedly, using a SV in which one of the ferromagnetic layers (F1) is pinned by an AF layer and the magnetization in the free layer (Ff) can be controlled by a constant-amplitude magnetic field, provides a more accurate control of the non-collinearity. At the first glance, it even seems that rotating the AF/F1/N/Ff/S or AF/F1/S/Ff valves in a constant magnetic field allows setting any non-collinear configuration in the SVs while

keeping the magnetic field in the S layer unchanged. Unfortunately, there is always a misalignment between the valve's plane and the plane of rotation. This misalignment results in appearance of a small component of the magnetic field perpendicular to the valve's plane in the S layer [Figure 34(a)]. The absolute value of this out-of-plane component changes when the sample is rotated, which results in a small change in T_C. Another important factor affecting the operation of the AF/F1/N/Ff/S or AF/F1/S/Ff valves, which is usually unjustifiably excluded from the consideration, is that biasing the AF layer provides only a finite pinning of the F1 layer. Hence, even a relatively low magnetic field tilts the F1 magnetization from the pinned direction.

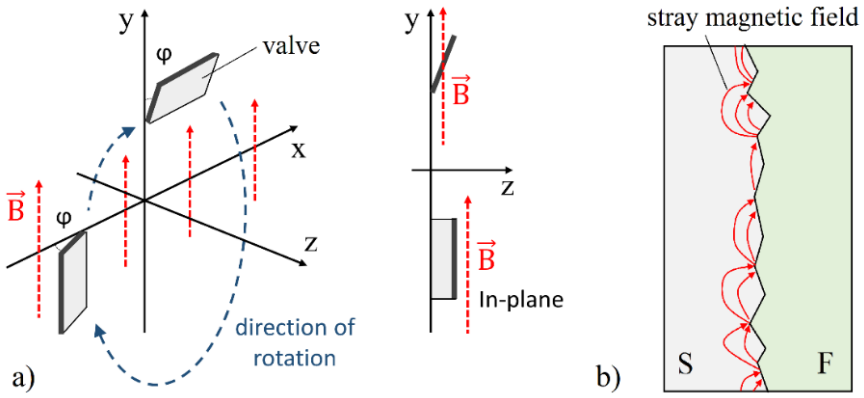

Figure 34 Schematics illustrating the origin of (a) out-of-plane magnetic field in the valve due to misalignment ($\varphi \neq 0°$) of the valve's plane and the plain of rotation (x-y), (b) stray magnetic field at the S/F interface.

Additionally, there are problems that are common for both experimental techniques (with and without rotation of SVs). First, the theory[183, 196, 197, 210] of superconducting SV effect was based on the assumption that both ferromagnetic (F1 and F2) layers are monodomain. For real SVs, this assumption is not valid, because a domain

structure of the F layers can be very complex. Moreover, the domain structure changes depending on the magnetization configuration in the SVs. Second, different magnetization configurations produce inherently different demagnetizing fields. Indeed, if a perfect thin ferromagnetic layer is magnetized in-plane, the stray field near its surface is negligible. But if the surface of the layer is not perfectly smooth, *i.e.*, there is some roughness, the stray field produced by surface defects appears [Figure 34(b)]. Typically, the field required for controlling the magnetization is low (50–1000 Oe). As a rough approximation, the value of demagnetization field caused by the roughness right near the F layer is of the order of M, where M is the magnetization of the F layers. It means that the effective magnetic field right above or below a rough F layer can considerably exceed the external magnetic field. The aggravating factor is that both F layers are in close proximity with each other, and, if the roughness of the layers is high, the stray field produced by one F layer can interact with the other F layer. Hence, the distribution of the stray field inside the SV can be very complex, furthermore, it depends on the magnetization configuration in the SV.[239] Along with the change in the magnetic field perpendicular to the SV surface, the stray field and complex domain structure inside the F layers can yield different T_C for different magnetic configurations.

V.1.3 Proposed approach to study odd-triplet superconductivity

The primary motivation for this project was to measure ΔT_C caused only by the superconducting SV effect, while all artifacts pertaining to conventional measurements must be excluded or minimized. Certainly, this implies designing a new type of superconducting SVs and developing new approach to the measurements of T_C. There are

three main requirements applied to the new SVs and T_C measurements in general. First, the new SVs must enable controlling the magnetization with and without using a rotator. Second, the out-of-plane component of the external magnetic field, which is inevitably present due to misalignment between the valve's plane and the plane of rotation, must be the same for different $R(T)$ dependences. Third, the stray magnetic field produced by the surface roughness of the F layers must be minimized.

The design of a conventional AF/F1/N/Ff/S valve was taken as a basis for developing the new SV. The idea was to substitute the single pinned ferromagnetic layer (F1) with a synthetic antiferromagnet (SAF) [Figure 35(a)]. The SAF consists of two ferromagnetic layers (F1 and F2) separated by a thin non-magnetic buffer.[240] Due to the Ruderman–Kittel–Kasuya–Yosida (RKKY) interaction,[241, 242] the sign of the coupling between the F1 and F2 layers depends on the thickness of the buffer. At some thicknesses, the coupling is antiferromagnetic. For such a case, in the absence of magnetic field, the magnetizations of the SAF layers are antiparallel and pointed along the easy axis of anisotropy.

Use of the SAF makes it possible to "imprint" any predefined non-collinear magnetization in the SV by cooling down the SV in an external magnetic field. Importantly, no rotation of the SF is required for this. The operation principle of the SV with the SAF is as follows. In-plane external magnetic field applied at a temperature above the blocking temperature (T_B) of the AF/F1 changes the angle η between the magnetizations in the F1 and F2 layers, whereas the net magnetic moment of the SAF is directed along the field [Figure 35(b)]. The value of the angle η can be controlled by tuning

the amplitude of the magnetic field. After cooling down the valve in a magnetic field H_{COOL} through T_B, the F1 layer adjacent to the AF gets pinned due to the exchange bias effect. The F2 layer does not interact with the antiferromagnet, hence, when the external field is ramped down, its magnetization sets antiparallel to the pinned magnetization of the F1 layer. The Ff layer adjacent to the S layer is free, and its magnetization is always aligned along the small magnetic field applied during the measurements (H_{MEAS}). Hence, after cooling down the SV in a magnetic field, the magnetizations in the SAF become pinned at an angle η with respect to the magnetic field direction, and hence, magnetization in the Ff. Importantly, the dependence of η on H_{COOL} can be determined empirically or theoretically, based on the properties of the SAF, and later used for controlling the non-collinearity in the SV.

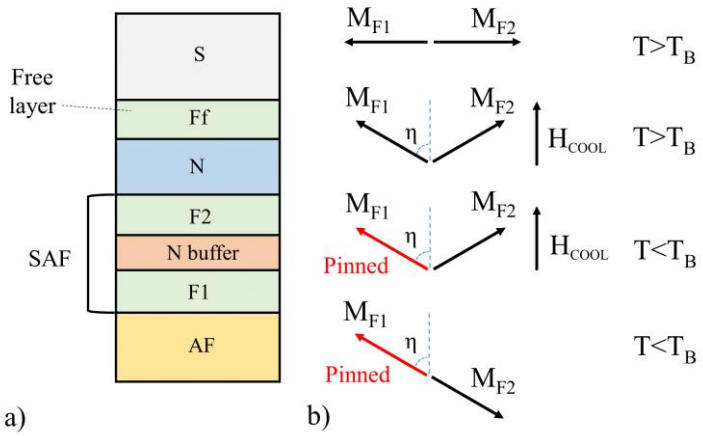

Figure 35 (a) Schematic illustrating a structure of the AF/SAF/N/Ff/S valve, (b) schematic illustrating principle of magnetizations pinning in the SAF by cooling down the SV in magnetic field (H_{COOL}) below the blocking temperature (T_B) of the AF layer. (After Ref. [244])

There are multiple advantages of the SV with the SAF. First, applying a magnetic field and subsequent cooling below the blocking temperature allow controlling the magnetizations in the SV without using a rotator. At the same time, the valve can be cooled down in a high magnetic field once, and then, η can be set by rotating the SV at low temperatures in H_{MEAS}. Using these two independent measurements, it is possible to get two sets of $T_C(\eta)$ dependences (obtained with and without rotation of the SV), which later can be compared. Importantly, for the measurement conducted without rotation, the out-of-plane component of the external magnetic field due to the misalignment of the SV's plane is constant. Second, since the net magnetization in the SAF is nominally compensated, this magnetization can withstand much higher magnetic fields without significant deflection from the pinned direction than a single pinned F layer. In particular, this provides that the magnetization configurations in the SVs with the SAF are more stable in a high magnetic field, in comparison to the SVs without a SAF. Third, the stray field produced by the F1 and F2 layers is mostly localized within the SAF,[243] and hence, the magnetic flux though the S layer is minimized. It is expected that the unique features of the SV with SAF allow eliminating the "side-effects" accompanied T_C measurement conducted using conventional superconducting SVs without a SAF, and thus, it yields ΔT_C due to the superconducting SV effect only.[244]

Intuitively, the essence of the superconducting SV effect consists in an increase or decrease of the number of Cooper pairs in the S layer depending on the magnetizations in the F layers. That, in turn, yields the change in T_C. The question arises: "is it possible, using some experimental techniques, to detect the depletion of the Cooper pairs directly?"

It is known that measuring the kinetic inductance (KI) is one of the ways to do it. From London phenomenological theory, KI of a superconductor wire, L_K, and the density of Cooper pairs in this wire, $n_{S,}$ are related as

$$L_k = \frac{m}{2n_S e^2}\frac{l}{wd}, \quad \text{(V-1)}$$

where *l*, *w*, and *d* are the length, width, and thickness of the wire, respectively; *m* is the electron mass, and *e* is the electron charge. There are two different methods that can be applied for measuring KI. The first method implies fabricating a lumped-element resonant circuit using a superconductor. Due to the KI and distributed capacitance, this circuit exhibits a resonance at a frequency f_0 which is related to L_K as

$$f_0 = 1/(2\pi\sqrt{L_K C_0}), \quad \text{(V-2)}$$

where C_0 is the capacitance of the circuit.[245, 246] Measuring the resonant frequency enables determining the KI of a superconductor. The other method for determining L_K of the superconducting wire is to measure the imaginary part of the complex impedance using a four-terminal AC technique.[247] The latter method is easier to implement. Besides, the operational frequencies for the complex impedance measurement is 0–100 kHz, while for the lumped-resonant circuit, the resonance usually occurs at much higher frequencies (100 MHz–10 GHz). Standing spin waves excited in the F layer by high-frequency signal can influence the magnetizations in the superconducting SV as well as the resonant frequency of the circuit.

In addition to the measurement of T_C, the depletion of Cooper pairs caused by the superconducting SV effect is studied by measuring KI of a superconducting SV. For this, the SV is shaped in the form of a very long wire, and the AC complex impedance of this

wire is measured using a four-terminal method. The KI measurement demonstrates how n_S depends on the magnetization configuration in the SV. In contrast to the T_C measurements which provide information on the system behavior around the critical temperature only, the KI measurements may reveal the behavior of the superconducting condensate in a wide range of temperatures.

V.2 Experimental and Simulation Details of Odd-triplet-superconductivity Study

V.2.1 Fabrication of superconducting spin valves with synthetic antiferromagnet

Two sets of superconducting SVs with SAF were prepared for the study: Py-based and Co-based. The only Py-based valve has Ta(4 nm)/Cu(5 nm)/FeMn(1 nm)/Py(2.5 nm)/Ru(0.7 nm)/Py(2.5 nm)/Cu(6 nm)/Py(2.5 nm)/Nb(30 nm)/Au(2 nm) (short: FeMn/Py/Ru/Py/Cu/Py/Nb) structure, whereas the Co-based valves structures are Ta(5 nm)/Cu(5 nm)/FeMn(1 nm)/Co(2 nm)/Ru(0.8 nm)/Co(2 nm)/Cu(6 nm)/Co(2 nm)/Nb(30 nm)/Cu(5 nm) and Ta(5 nm)/Cu(5 nm)/FeMn(1 nm)/Co(2 nm)/Ru(0.8 nm)/Co(2 nm)/Nb(30 nm)/Co(2 nm)/Cu(5 nm) (short: FeMn/Co/Ru/Co/Cu/Co/Nb and FeMn/Co/Ru/Co/Nb/Co, respectively). The multilayers were deposited using DC magnetron sputtering on top of Si/SiO_2 substrates. Prior to the deposition, the sputtering chamber was pumped to the base pressure of 1×10^{-8} Torr. The Ar pressure was 2 mTorr during the deposition. The substrates were moved over the guns during the deposition to achieve high uniformity of the layer thickness. Prior to the fabrication of the multilayers, the deposition rates for all materials were calibrated using small-angle X-ray reflectivity.

The deposition rates were: Ta and Cu–1 Å/s, FeMn–0.96 Å/s, Py, Co–0.88 Å/s, Ru–0.68 Å/s, Nb–1.26 Å/s.

A small in-plane magnetic field (about 50 Oe) was applied during sputtering of the Py-based SV to induce a uniaxial anisotropy in the Py layers. This anisotropy assists coherent rotation of magnetization rather than magnetization reversal through growth of domains in the SAF,[248] and also defines the preferred orientation of the Py magnetizations. The Co-based SVs were deposited without applying the external magnetic field. The thickness of the FeMn was chosen to be 1 nm to achieve relatively low blocking temperature, T_B, for the FeMn/Py and FeMn/Co stacks. That allowed us to minimize temperature ramping, and hence, time required for each cooling procedure.

In addition, the SAF stacks, Py(2.5 nm)/Ru(0.7 nm)/Py(2.5 nm) (short Py/Ru/Py) and Co(2 nm)/Ru(0.8 nm)/Co(2 nm) (short Co/Ru/Co), were fabricated for the characterization of the SAF properties.

V.2.2 Fabrication of wire for kinetic inductance measurements

According to Equation (V-1), in order to maximize KI of the wire, L_K, the wire must be narrow and long. The density of the electrons in Nb is of the order of 10^{22} cm^{-3}. To a first approximation, this value can be used for estimating the Cooper pair density, n_S.[249] The complex part of the wire impedance R_W is

$$R_W = 2\pi\nu L_K, \qquad \text{(V-3)}$$

where ν is the frequency of the AC current. The maximum AC frequency that can be analyzed using an SR830 DSP Lock-in Amplifier is 100 kHz. Consequently, to have an impedance of 1 mΩ at 100 kHz for a 10 μm-wide wire, its length must be around 2 m.

A Ta(5 nm)/Cu(5 nm)/FeMn(1 nm)/Co(2 nm)/Cu(6 nm)/Co(2 nm)/Nb(30 nm)/Cu(5 nm) (short FeMn/Co/Cu/Co/Nb) SV was prepared for the KI study. The film was covered by a S1813 positive photoresist and baked on a hot plate at 115 °C for 5 min. A meandering wire was patterned on the film using a laser writer. The written pattern was developed by immersing the sample to CD-26 developer and gentle stirring for 40 sec. The final step of the fabrication was ion-beam milling. To prevent possible damage of the film due to the heat produced by the ion beam, liquid N_2 was circulated through the copper stage to which the sample was attached during the milling. The leftover of the photoresist was removed by keeping the sample in acetone for 30 hours and an ultrasonic bath for 30 seconds. An image of the fabricated FeMn/Co/Cu/Co/Nb wire is shown in Figure 36. The dimensions of the meander are 10.58 mm×4.13 mm. The wire is 10 μm-wide and 2 m-long. The wire was installed on a PPMS rotator-holder for the measurements.

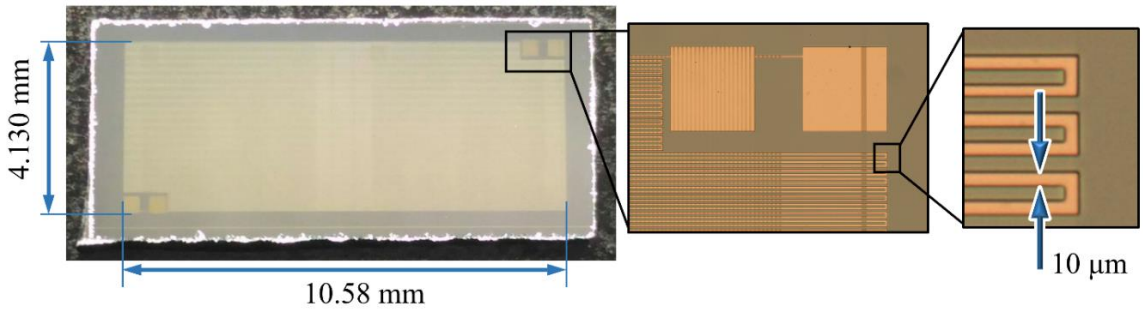

Figure 36 An image of the FeMn/Co/Cu/Co/Nb meandering wire.

V.2.3 Simulations of spin valves magnetizations

An analytical single-domain coherent rotation (SDCR) model was applied for simulating the experimental magnetometry and transport measurements. Fitting of experimental dependences using the simulated curves allows determining which magnetic

configurations are realized in the SVs and how these configurations are affected by the external magnetic field. The model is based on the assumptions that first, the magnetizations of the SAF layers and the free layer are uniform (single-domain approximation), and second, magnetic field causes the magnetizations to rotate coherently in plane (coherent-rotation approximation).

The total energy, E_{Total}, of the system can be represented as

$$E_{Total} = E_{Zeeman} + E_{AF} + E_{Paras} + E_{Uniaxial} + E_{Unidirect}, \quad \text{(V-4)}$$

where E_{Zeeman} is the Zeeman energy of the ferromagnets, E_{AF} is the energy of antiferromagnetic coupling in the SAF, E_{Paras} is the energy responsible for a weak parasitic coupling between the free layer and the SAF, $E_{Uniaxial}$ is the energy of the uniaxial anisotropy, $E_{Unidirect}$ is the energy of the unidirectional anisotropy induced in the F layer due to the proximity with the AF. E_{Total} depends on the mutual angles between the magnetic moments in the ferromagnetic layers as well as their angles with respect to the external magnetic field. Numeric minimization of E_{Total} by varying the magnetization orientation in the free layer and the SAF layers enables determining the stable magnetization configuration in the SV in different external magnetic fields. (see Appendix A)

V.2.4 Characterization of synthetic antiferromagnets

It is clear that for a controllable operation of the SVs with SAF, it is essential to know the behavior of magnetizations in the F1 and F2 layers at different temperatures and magnetic fields. First, it is necessary to make sure that the antiparallel alignment of the magnetizations is realized at remanence. Second, to understand if the magnetizations

rotate coherently, the response of the SAF to magnetic field needs to be analyzed. To do this, the hysteresis loops of the Py- and Co-based SAFs stacks were measured at 300 and 10 K (Figure 37 black dots). For the Py-based SAF, the magnetic field was applied perpendicular to the uniaxial anisotropy in the Py layers. At 300 K, the net magnetization of the SAF stacks demonstrate a linear rise with increasing magnetic field and subsequent saturation in 1.8 and 6.5 kOe for the Py- and Co-based SAFs, respectively. In contrast, the magnetization of the stacks rise non-linearly at low temperatures. At 10 K, the complete saturation of the magnetization is achieved in 3.5 and 7.8 kOe for the Py- and Co-based SAFs, respectively. The magnetizations of Py and Co vary insignificantly in the 10–300 K temperature range, hence, the enhancement of the saturation fields at low temperatures is due to strengthening of bilinear exchange coupling between the F1 and F2 layers. It is expected that, the non-linear dependence of the SAFs magnetizations on magnetic field is due to a biquadratic exchange coupling between the F1 and F2 layers at low temperatures.

The fits of the hysteresis loops for the Py-based SAF using SDCR simulations (Figure 37 red lines) show that at 300 K, the coefficients of bilinear, J_1, and biquadratic, J_2, couplings are -0.175 erg/cm^2 and 0 erg/cm^2, respectively, whereas at 10 K, J_1 = -0.24 erg/cm^2 and J_2 = 0.06 erg/cm^2. The fitting of the loops for the Co-based SAF provides that the bilinear coupling does not change with temperature, *i.e.*, J_1 = -0.8 erg/cm^2 at 300 and 10 K; while J_2 increases from 0.06 erg/cm^2 0.13 erg/cm^2 at 10 K. Interestingly, the rise of the biquadratic coupling is either due to a change in a band structure of Ru with temperature,[250] or, as shown by Slonczewski,[251] due to an increase of F layers magnetic roughness (defects on the F surfaces become ferromagnetic at low temperatures).[252] If the

latter mechanism is realized it means that a stray field produced by the surface defects is highly enhanced at low temperatures. Prior to the fabrication of the SVs, a series of Py and Co-based SAF stacks with different thicknesses of the Ru layer were prepared. The SAF with 0.7 and 0.8 nm-thick Ru layers were chosen for the implementation in the SVs, because they provide relatively-low biquadratic and, simultaneously, relatively-high bilinear couplings.

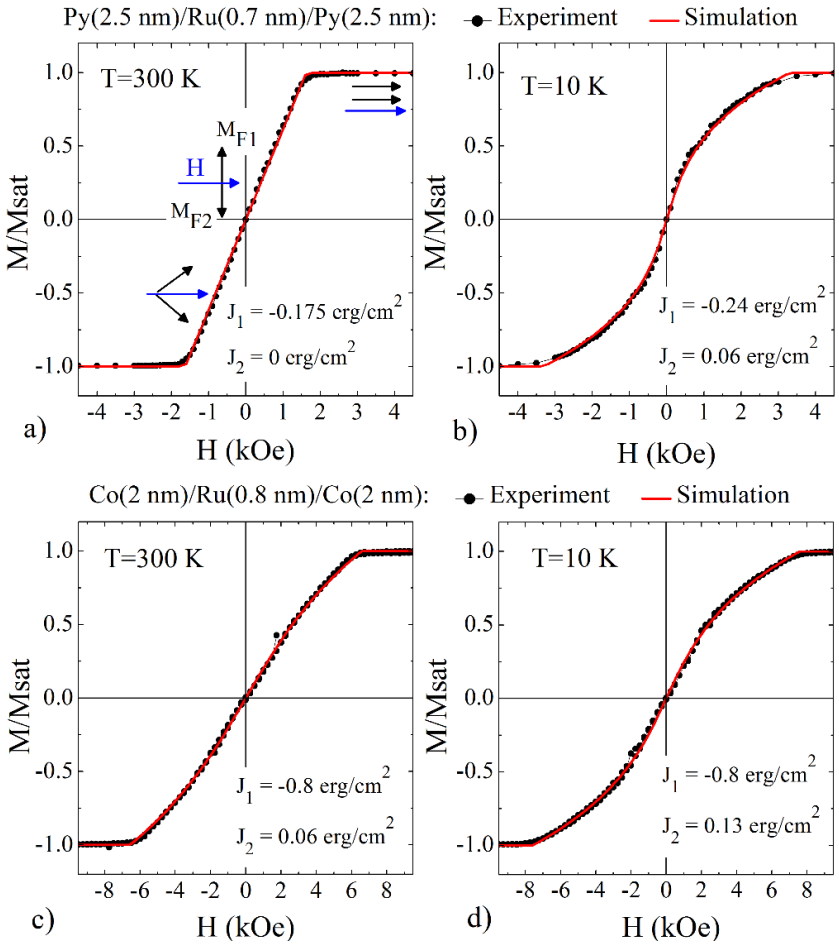

Figure 37 The magnetization curves of the Py/Ru/Py SAF stack at 300 K (a), 10 K (b), and the Co/Ru/Co SAF stack at 300 K (c), 10 K (d). Black thin lines and dots are experimental data, red solid lines are SDCR fit. J_1 and J_2 are the bilinear and biquadratic exchange couplings, respectively, determined from the fits. The arrows in (a) depict the orientation of magnetizations with respect to the magnetic field. (After Ref. [244])

An absence of the net SAFs magnetization in a zero-magnetic field indicates that the magnetizations of the F1 and F2 layers are antiparallel at remanence. Remarkably, the SDCR simulations show that the magnetizations tend to align perpendicular to the field-direction at remanence, despite the fact that the uniaxial anisotropy perpendicular to the field exists only in the Py layers. Increase in the magnetic field decreases the angle between the magnetizations while their net magnetization aligns along the field until the full saturation is achieved.

V.2.5 Calibration of superconducting spin valves with synthetic antiferromagnet

The experimental magnetization curves for both SAFs do not demonstrate hysteresis (Figure 37). With respect to the SV with the SAF, it means that the amplitude of cooling field uniquely defines the angle, η, between the imprinted magnetization in the SAF and magnetic field direction (Figure 35). Meanwhile, since the interlayer exchange coupling between the F1 and F2 layers changes significantly with temperature, it is impossible to determine which magnetization configuration is imprinted in the SV after cooling in a particular magnetic field based only on the magnetization curves for the corresponding SAFs. That is, for a controllable operation of a SV with SAF, the dependence of η on the amplitude of cooling magnetic field the SV (H_{COOL}) needs to be obtained empirically.

Due to a spin-dependent scattering, the resistance of the 6-nm-thick Cu layer between the SAF and the free F layer of the SV is very sensitive to the mutual magnetization orientation in these layers, which gives rise to the GMR effect. SV resistance reaches maximum and minimum values when the magnetization in the F2 layer

of SAF is antiparallel and parallel, respectively, to the magnetization in the Ff layer. Hence, measuring angular dependences of the SVs resistance in low magnetic field at a temperature slightly above T_C enables determining the angle η at which magnetizations of the SAF were imprinted.

The measurement protocol was as follows. At a temperature above T_B (T_B is around 100 K for the Py- and Co-based SVs), a SV was set to Θ = 0° orientation. Θ is the angle between the long edge of the SV stripe and the external magnetic field. Then, the valve was cooled down to 10 K in H_{COOL}, and an angular dependence of the SV resistance was measured in a 200-Oe magnetic field. The Py-based SV stripe was cut in such a way that the long edge and, hence, the magnetic field direction are perpendicular to the uniaxial anisotropy in the Py layers.

Figure 38(a, c, and d) displays the angular dependences of the FeMn/Py/Ru/Py/Cu/Py/Nb SV measured after it was cooled down in 5 kOe, 0 Oe, and 1.5 kOe. It is expected that if the SV is cooled down in a magnetic field which is high enough to align the magnetizations of the SAF parallel, these magnetizations will become pinned along the field direction. Angular dependence of the resistance measured after the SV was cooled down in 5 kOe [Figure 38(a)] has a maximum at 0°. This confirms that the SAF magnetizations are imprinted along the field direction (Θ = 0°). At the same time, when the valve is cooled down in a zero magnetic field, it is expected that the magnetizations in the F1 and F2 layers are directed along the easy axis of the anisotropy in Py, and hence, the GMR is maximal at -90° or 90°. However, the angular dependence of the resistance measured after the SV is cooled in a zero-magnetic field [Figure 38(c)],

reaches its maximum at -80°. A possible reason for this deviation is the misalignment of the cut, *i.e.*, the angle between the stripe's long edge and the easy axis of the anisotropy in Py was not 90°.

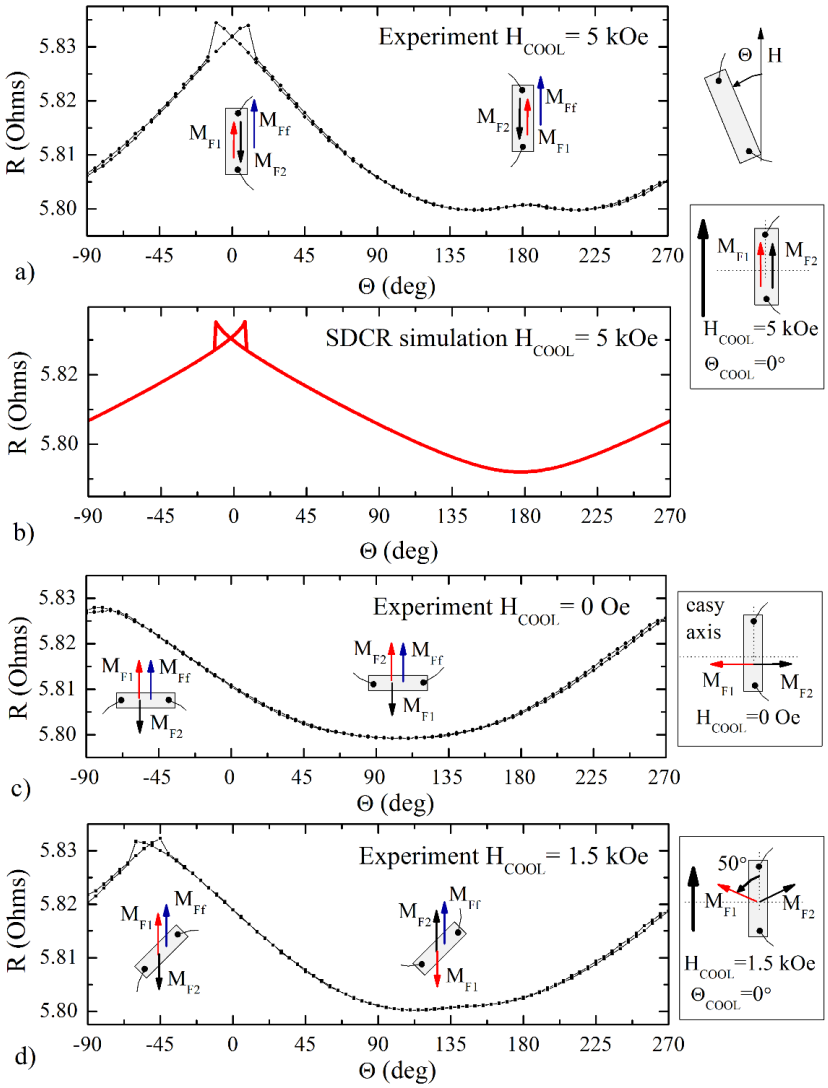

Figure 38 The experimental angular dependences of resistance for the FeMn/Py/Ru/Py/Cu/Py/Nb SV measured at 10 K in a 200-Oe magnetic field after the SV was cooled down to 10 K in (a) 5-kOe, (c) 0-Oe, (d) 1.5-kOe magnetic fields. (b) a SDCR simulation of the (a) curve. The top-right inset depicts how the angular orientation (Θ) of the SV is defined. The insets in front of each curve demonstrate the orientation of the SV and the orientation of the magnetizations in each layer during the magnetic-field-cooling procedure. (After Ref. [244])

Figure 38(d) shows the dependence obtained when the valve is cooled down in an intermediate field, 1.5 kOe. In this case, the GMR maximum is at -50° and, hence, the magnetizations in the SAF are imprinted at 50° with respect to the magnetic field direction.

Since the antiferromagnetic coupling between the F1 and F2 layers and the unidirectional anisotropy in the F1 layer are finite, the magnetic field causes a distortion of the imprinted magnetization configuration. SDCR simulations were performed to understand how a relatively-low magnetic field of 200 Oe applied for controlling the magnetization in the Ff layer, affects the pinned SAF. For this, magnetization configurations for different orientations of the SV with respect to the magnetic field were determined in the simulations. Then, the resistance of the SV for each configuration was estimated assuming that the resistance R of a SV[253] is

$$R = R_0 + \Delta R \sin^2(\eta/2), \qquad \text{(V-5)}$$

where R_0 is the angular-independent part of the resistance, ΔR is the amplitude of the angular-dependent part of the resistance due to the GMR effect, η is the angle between the magnetizations in the F2 and Ff layers.

The simulated $R(\Theta)$ curve corresponding to the case when the magnetizations in the SAF are pinned along the magnetic-field direction is shown in Figure 38(b). The experimental and simulated curves agree [Figure 38(a and b)], except for a minor peak at Θ = 180° observed in the experiment. This bump is caused by the anisotropic magnetoresistance of Py,[79] which was excluded from the consideration in the simulations. The parameters of the SDCR model providing the best fit of the $R(\Theta)$ curves for the Py-

based SV are: J_1 = -0.24 erg/cm^2, J_2 = 0.06 erg/cm^2, K_{EB} = 0.037 erg/cm^2, J_{PAR} = 0.01 erg/cm^2, K_U = 2000 emu/cm^3.

Importantly, the SDCR simulations show that when the Py-based SV is rotated in a 200-Oe magnetic field the angle between the magnetizations of F1 and F2 of the SAF changes from 160° to 200°. Besides, the simulations reveal that the F1 moment of the SAF can be deflected by the field from the pinned direction only to 35°. In contrast, if the SV contained a single fixed F1 layer instead of the SAF stack, the deflection would have reached 90°.

Remarkably, the SDCR simulations also allowed us to explain the abrupt drops of the resistance observed in the vicinity of the $R(\Theta)$ curves maxima for the Py-based SV(Figure 38(a and d)). The mechanism responsible for the phenomenon is as follows. The 200-Oe magnetic field tends to align the F1 and F2 magnetizations along the field. Consequently, the SAF gains a small uncompensated magnetic moment. When the SV is rotated in the field, the direction of the uncompensated magnetic moment does not coincide with the direction of the field because of the unidirectional anisotropy in the F1 layer. As a result, a backlash between the field and the uncompensated magnetic moment of the SAF appears. When the field passes the pinning direction, the system turns to a metastable state: the vectors of the uncompensated moment of the SAF and the field are in the opposite semiplanes defined by the pinning direction. Further rotation results in a significant increase in the backlash, and hence, the Zeeman energy. At some critical angle, it becomes energetically favorable for the system to reconfigure the magnetizations of the SAF. This reconfiguration results in the abrupt change in the GMR.

The angular dependences of resistance measured at 10 K for the FeMn/Co/Ru/Co/Cu/Co/Nb SV also demonstrate that depending on the amplitude of the magnetic field in which the SV was cooled down, different magnetization configurations can be imprinted in the SV. However, the shape of the dependences for the Co-based SV is different from that for the Py-based SV. For example, a $R(\theta)$ curve obtained after cooling down the FeMn/Co/Ru/Co/Cu/Co/Nb SV in 4-kOe magnetic field is shown in Figure 39. It is easy to see that the peak is wider for this SV; also, there are no abrupt drops of the resistance observed for the FeMn/Py/Ru/Py/Cu/Py/Nb SV. It is expected that, in contrast to the Py-based SV, different grains of the Co layers do not have preferable orientation of anisotropy as only the Py-based SV was grown in magnetic field. It means that a complicated domain structure can emerge in these Co layers at 300 K. When the SV is cooled down to 10 K, different domains become pinned at slightly different angles with respect to the field direction, which results in broadening of the $R(\theta)$ curve for the Co-based SV. To assist establishing a preferable direction for the Co grains magnetization, a high magnetic field was applied perpendicular to the cooling-field direction prior to cooling the Co-based SVs.

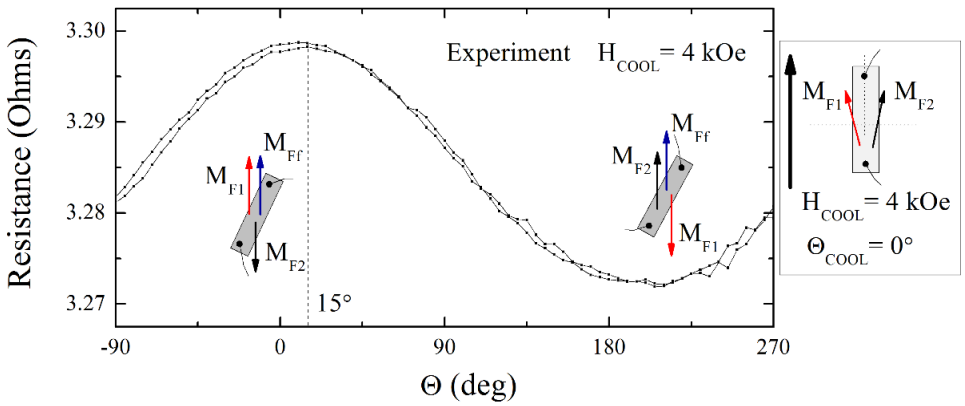

Figure 39 The experimental angular dependence of resistance for the FeMn/Co/Ru/Co/Cu/Co/Nb SV measured at 10 K in a 200-Oe magnetic field after SV was cooled down to 10 K in 4-kOe magnetic field.

GMR curves measured after cooling the Py and Co-based SVs in different magnetic fields provide the angle η between the magnetization imprinted in the SAF and the field that depends on the magnitude of the cooling field (Figure 40). These curves can be used for setting any predefined noncollinear magnetization configuration in the SVs without using a rotator. Unfortunately, it is impossible to get a $\eta(H_{COOL})$ curve by measuring the angular dependences of resistance for the FeMn/Co/Ru/Co/Nb/Co SV, since the change in its resistance due to the spin-dependent scattering of carriers in the 30 nm-thick Nb layer is very small. It was assumed that the $\eta(H_{COOL})$ dependence obtained for the FeMn/Co/Ru/Co/Cu/Co/Nb SV is applicable for a controllable imprinting of magnetizations in the FeMn/Co/Ru/Co/Nb/Co SV.

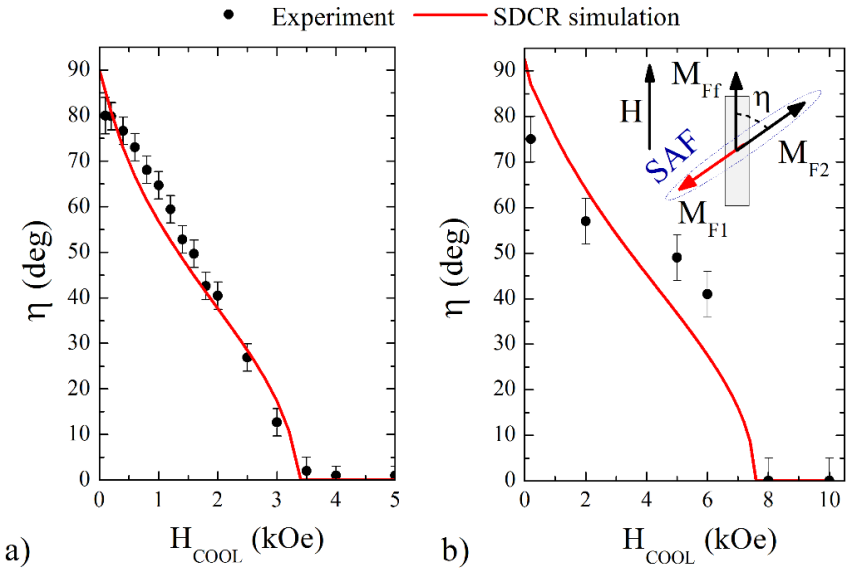

Figure 40 The angle between magnetizations in the SAFs and the magnetic field direction, η, as a function of the cooling magnetic field, H_{COOL}, for (a) the FeMn/Py/Ru/Py/Cu/Py/Nb SV and (b) the FeMn/Co/Ru/Co/Cu/Co/Nb and FeMn/Co/Ru/Co/Nb/Co SVs (black squares are the experimental data, red lines are the SDCR fits). The inset in the top-right corner of (b) demonstrates the orientation of magnetizations with respect to the external magnetic field at low temperatures. (After Ref. [244])

V.3 Experimental Results on T_C and Kinetic Inductance Measurements

V.3.1 Approach to T_C measurements of superconducting spin valve with synthetic antiferromagnet

It was demonstrated that using the Py- and Co-based SVs with SAF, it is possible to imprint different magnetization configurations without using a rotator. The next step was to study the superconducting SV effect using these SVs. For this, the dependence of the Nb layer T_C on the angle between the magnetizations in the free layer and the SAF must be measured. The intention was to understand how the rotation of the SV during the measurement affects the T_C. To do this, two independent experiments must be performed with each of the SVs:

1) T_C measurement with rotation of the SV (conventional technique). It implies using the superconducting SV with SAF in a conventional regime, *i.e.*, when the magnetization of the fixed layer is pinned and the non-collinearity between the free layer and the SAF is controlled by rotating the SV. The experimental procedure for this measurement is as follows: At 300 K, the SV is installed in such a way that its long edge is set at an angle Θ_{COOL} with respect to the field direction. Then, the SV is cooled down to 10 K in a magnetic field that is high enough to saturate the SAF. After this, the SV is operated only at low temperatures. The $R(T)$ dependences are obtained by slowly (0.02 K/min) sweeping down the temperature bellow T_C and then back up in a small magnetic field (H_{MEAS}). To change the magnetization configuration in the SV, the angle between the SV and magnetic field must be changed by rotating the SV at 10 K.

2) T_C measurement without rotation of the SV, by using the properties of the SAF instead (cooling-field-imprinting technique). The essence of this technique is that to obtain an angle η between the magnetizations in the SAF and the free layer, the SV must be cooled down in a magnetic field H_{COOL} defined by the $\eta(H_{COOL})$ dependences shown in Figure 40. No SV rotation is required for this. The following procedure is used: The long edge of the SV is set along the field direction, thus $\Theta = 0°$. Then, the SV is cooled to 10 K in H_{COOL}, and $R(T)$ dependence is obtained in a low magnetic field (H_{MEAS}), while $\Theta = 0°$ all the time. Then, to get another magnetization configuration in the SV the procedure is repeated by cooling the valve in a different H_{COOL}.

V.3.2 T_C measurements of FeMn/Py/Ru/Py/Cu/Py/Nb valve

The dependences of the FeMn/Py/Ru/Py/Cu/Py/Nb SV resistance on temperature measured using the conventional method (with the SV rotation) is shown in Figure 41. The SV was cooled down in a 5-kOe magnetic field applied parallel (Θ_{COOL} = 0°) [Figure 41(a and b)] and perpendicular (Θ_{COOL} = 90°) [Figure 41(c and d)] to the SV's long edge. $R(T)$ dependences were obtained for orientations of the SV providing parallel, perpendicular, and antiparallel configurations between magnetizations of the Ff layer and SAF using a 1-μA excitation current (I_{MEAS}) [Figure 41(a and c)]. In addition, another set of $R(T)$ dependences was obtained with I_{MEAS} = 1 mA [Figure 41(b and d)]. Due to a percolative nature of the Nb-layer conductivity, the SV resistance decreases non-monotonically. The spread of the superconducting transition temperature is around 0.4 K. For the FeMn/Py/Ru/Py/Cu/Py/Nb SV, T_C was defined as a temperature at which the resistance is 0.5 Ω.

The curves corresponding to the different magnetization configurations demonstrate slightly different T_C. Although the resistance noise is relatively high at temperatures within the T_C-spread of the transition, statistically, the curve corresponding to the parallel configuration (black line/dots) passes above the curve corresponding to the antiparallel configuration (blue line/dots). This behavior indicates the occurrence of the standard superconducting SV effect. Moreover, T_C of the SV with perpendicular magnetization configuration ($T_{\uparrow\rightarrow}$) measured with I_{MEAS} = 1 μA is 4 mK smaller than that for the parallel or antiparallel configurations ($T_{\uparrow\uparrow}$, $T_{\uparrow\downarrow}$). For I_{MEAS} = 1 mA, the difference between $T_{\uparrow\uparrow}$ and $T_{\uparrow\rightarrow}$ becomes even larger (ΔT_C = 7 mK).

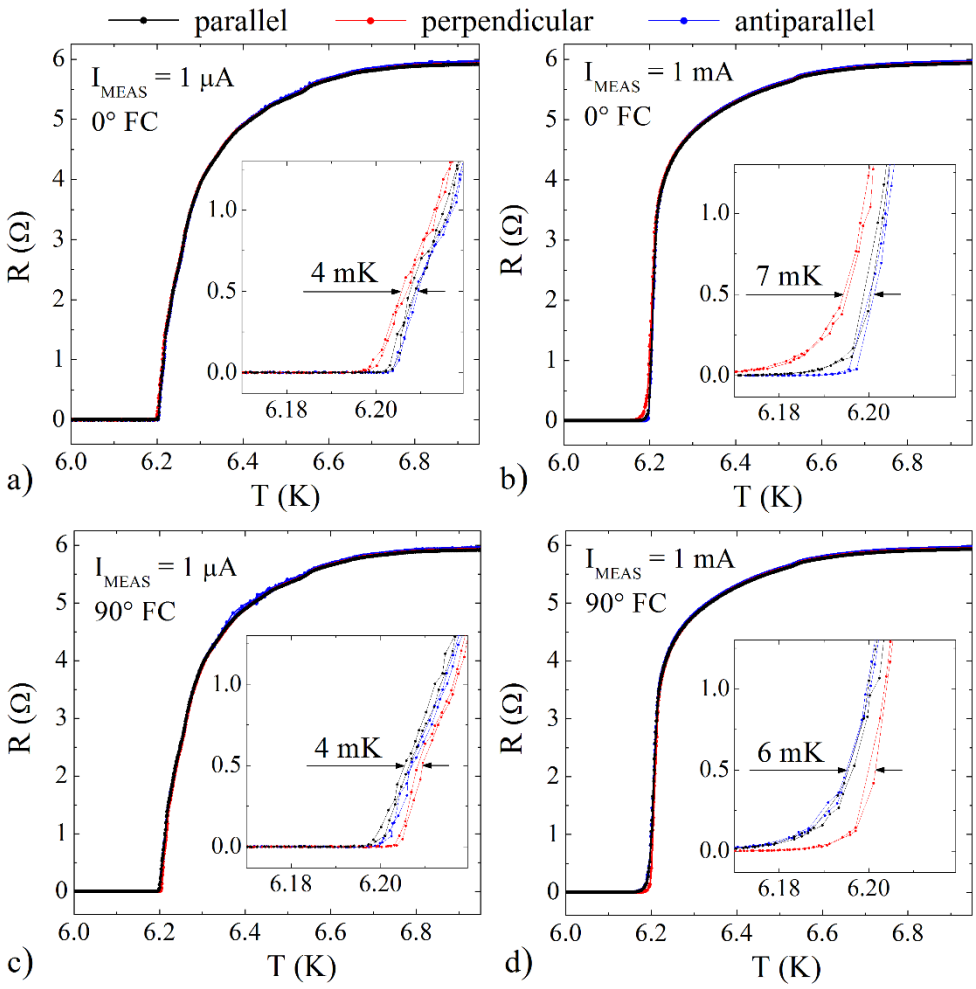

Figure 41 The $R(T)$ dependences for the FeMn/Py/Ru/Py/Cu/Py/Nb SV measured in a 200-Oe magnetic field using 1-μA and 1-mA excitation current after the SV was cooled in a 5-kOe magnetic field applied parallel (Θ_{COOL} = 0°) (a and b) and perpendicular (Θ_{COOL} = 90°) (c and d) to the SV's long edge. The SV was rotated for obtaining parallel, antiparallel, and perpendicular magnetization configurations.

At the first glance, the suppression of T_C for the perpendicular orientation could be interpreted as the superconducting SV effect caused by the generation of the odd-triplet pairing in the SV. To verify this assumption, the same conventional measurements (with the SV rotation) were conducted, but at this time, the valve was cooled down in a 5-kOe magnetic field which was applied perpendicular to the SV's long edge, *i.e.*, Θ_{COOL} = 90°

[Figure 41(c and d)]. Although the statistical decrease in resistance for the antiparallel configuration in comparison to that for the parallel one is still observed in these measurements, T_C for the perpendicular orientation is now higher than the T_C for the parallel and antiparallel configurations. Moreover, the difference between $T_{\uparrow\uparrow}$ and $T_{\uparrow\rightarrow}$ has the same absolute value for both Θ_{COOL} = 0° and Θ_{COOL} = 90° measurements. This means that T_C does not depend on the magnetization configurations in the SV, but rather depends on the orientation of the SV with respect to the magnetic field. T_C is smaller when the SV is parallel or antiparallel to the field (Θ = 0° or 180°).

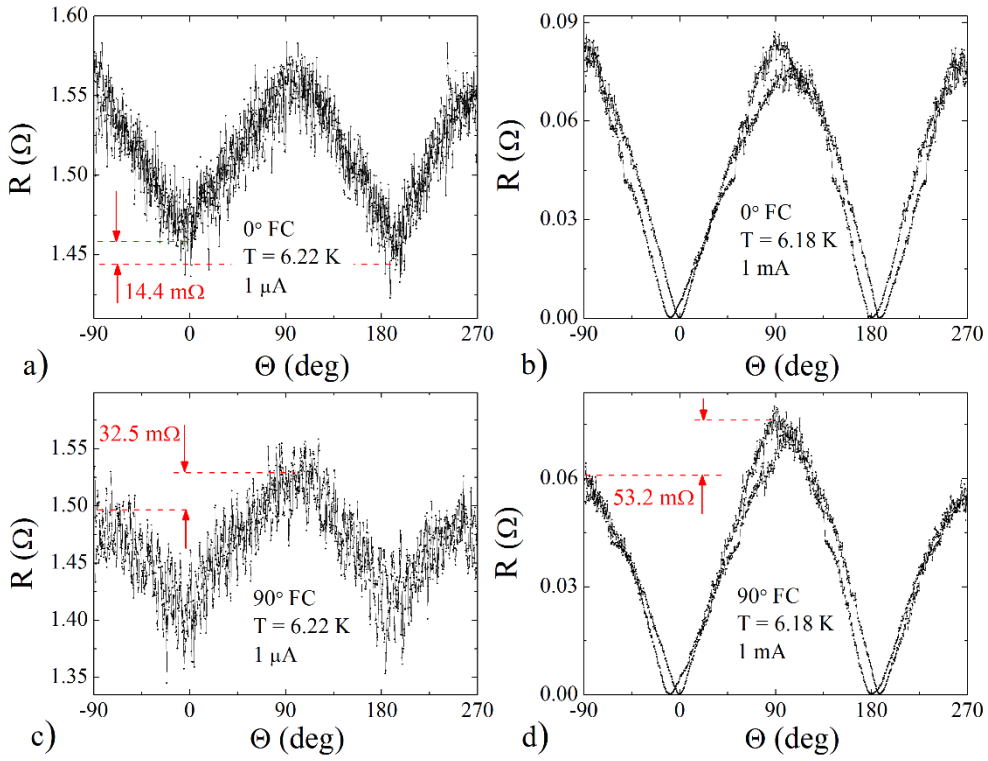

Figure 42 The angular dependences of resistance for the FeMn/Py/Ru/Py/Cu/Py/Nb SV measured at 6.22 K with 1-μA excitation current (a and c) and 6.18 K with 1-mA excitation current (b and d) in a 200-Oe magnetic field after the SV was cooled in a 5-kOe magnetic field applied parallel (Θ_{COOL} = 0°) (a and b) and perpendicular (Θ_{COOL} = 90°) (c and d) to the SV's long edge.

To analyze the effect of the SV orientation on the suppression of the superconductivity, an experiment similar to the one done by Flokstra *et al.*[237] was conducted for the FeMn/Py/Ru/Py/Cu/Py/Nb SV. The idea was to measure the angular dependence of the SV resistance in the 200-Oe magnetic field at a temperature which is within the T_C-spread of the $R(T)$ curve. In contrast to the experiment performed by Flokstra *et al.*, our experiment consisted of two sets of measurements: $R(\Theta)$ dependences after cooling down the SV in a 5-kOe magnetic field applied parallel ($\Theta_{COOL} = 0°$) [Figure 42(a and b)] and perpendicular ($\Theta_{COOL} = 90°$) [Figure 42(c and d)] to the SV's long edge. It was observed that, while the SV was rotated, its resistance oscillated. When the SV was cooled down in a magnetic field parallel to its long edge ($\Theta_{COOL} = 0°$) the minima of resistance were at 0° and 180°, *i.e.*, at the orientations in which the magnetizations in the free layer and the SAF were perpendicular to each other. This result is identical to the one obtained by Flokstra. Again, the suppression of the resistance for the perpendicular magnetization configurations could be explained by the generation of the long-range triplet pairing. But if this were the case, the minima must shift 90° when the SV was cooled down in the field perpendicular to its long edge ($\Theta_{COOL} = 90°$). As can be seen from Figure 42(c and d), that did not happen in the experiment: the shapes of the $R(\Theta)$ curves change insignificantly, but the positions of the minima remain unchanged.

It can be concluded that the variation of the SV orientation with respect to the magnetic field results in a larger ΔT_C than the suppression of T_C expected from the generation of the long-range triplet pairing. Hence, the measurements with SV rotation are not suitable for studying the effect.

The T_C measurements for the FeMn/Py/Ru/Py/Cu/Py/Nb SV conducted using a cooling-field-imprinting technique are shown in Figure 43. The SV stripe was kept parallel to the magnetic field during all cooling-field procedures (Θ = 0°). The $R(T)$ dependences were performed using 1-μA excitation current in a 200-Oe magnetic field. We observed that T_C were the same for all magnetization configurations. There is some insignificant increase of T_C (2 mK) when a non-collinear magnetization configuration is imprinted in the SV.

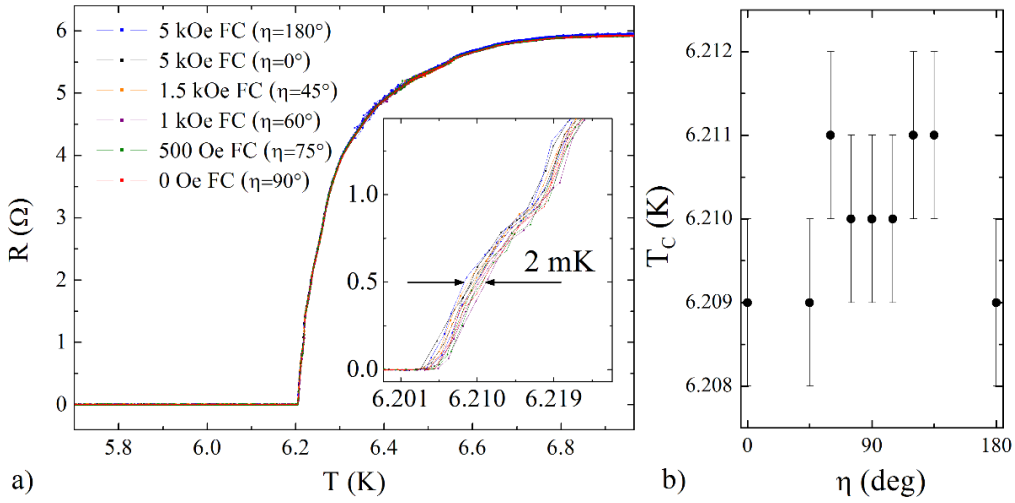

Figure 43 (a) $R(T)$ dependences for the FeMn/Py/Ru/Py/Cu/Py/Nb SV measured in a 200-Oe magnetic field, using 1-μA excitation current. The SV was cooled down in different magnetic fields for obtaining different magnetization configurations (without the SV rotation), (b) T_C of the FeMn/Py/Ru/Py/Cu/Py/Nb SV depending on the angle between the magnetizations in the SAF and the free layer, η.

V.3.3 Discussion of T_C measurements of FeMn/Py/Ru/Py/Cu/Py/Nb valve

How can the obtained experimental results be interpreted? First, there is no evidence that the odd-triplet pairing is generated in this SV. It was shown that for the conventional measurements, the difference in the $R(T)$ curves is not due to the

magnetization configuration in the SV but rather due to the orientation of the valve with respect to the magnetic field. It is assumed that the misalignment between the plane of rotation and magnetic field yields the magnetic flux through the SV's surface changes when the SV rotates. This flux breaks the pinning of the superconducting vortices, and their dissipative flow results in the small change in T_C. Presumably, the vortex flow at temperatures close to T_C is significantly enhanced when the excitation current is ramped from 1 μA to 1 mA. This explains why the absolute value of ($T_{\uparrow\uparrow}$ - $T_{\uparrow\rightarrow}$) almost doubles from 4 mK to 7 mK (Figure 41).

It is clear that the rotation of the SV cannot influence the ($T_{\uparrow\uparrow}$ - $T_{\uparrow\downarrow}$) because the flux of the magnetic field is the same for parallel and antiparallel magnetization configurations. Unexpectedly, the $R(T)$ measurements with the SV rotation shows that $T_{\uparrow\downarrow}$ is only about 0.5 mK higher than $T_{\uparrow\uparrow}$ (Figure 41), and no difference between $T_{\uparrow\downarrow}$ and $T_{\uparrow\uparrow}$ is detected for the $R(T)$ measurements without the SV rotation. At the same time, according to the $R(\Theta)$ curves shown in Figure 42, the resistance of the SV with antiparallel magnetization configuration is lower than the resistance with the parallel configuration. This means that for this particular SV, the standard superconducting SV effect is very weak, but the $R(\Theta)$ measurements at a temperature which is within the T_C-spread, enable detecting this effect with high accuracy.

V.3.4 T_C measurements of FeMn/Co/Ru/Co/Cu/Co/Nb and FeMn/Co/Ru/Co/Nb/Co valves

The dependences of the FeMn/Co/Ru/Co/Cu/Co/Nb and FeMn/Co/Ru/Co/Nb/Co SVs resistance on temperature measured using the conventional method (with the SV

rotation) is shown in Figure 44 (only parts of the curves containing the superconducting transitions are shown). Similarly to the FeMn/Py/Ru/Py/Cu/Py/Nb SV (Figure 41), the Co-based SVs were cooled down in a 10-kOe magnetic field applied parallel (Θ_{COOL} = 0°) [Figure 44(a and b)] and perpendicular (Θ_{COOL} = 90°) [Figure 44(c and d)] to the SVs' long edges. $R(T)$ dependences were obtained for the orientations of the SV providing parallel, perpendicular, and antiparallel configurations between magnetizations of the Ff layer and the SAF using a 1-μA excitation current (I_{MEAS}) [Figure 44]. T_C was defined as a temperature at which the resistance is 0.5 Ω.

Similarly to the FeMn/Py/Ru/Py/Cu/Py/Nb SV (Figure 41), the curves for different magnetization configurations do not coincide. According to these measurements, $T_{\uparrow\downarrow}$ is about 2 and 1 mK higher than $T_{\uparrow\uparrow}$ for the FeMn/Co/Ru/Co/Cu/Co/Nb and FeMn/Co/Ru/Co/Nb/Co SVs, respectively. In contrast to the FeMn/Py/Ru/Py/Cu/Py/Nb SV, the curve corresponding to the perpendicular configuration passes between those corresponding to the parallel and antiparallel configurations, *i.e.*, $T_{\uparrow\uparrow} < T_{\uparrow\rightarrow} < T_{\uparrow\downarrow}$.

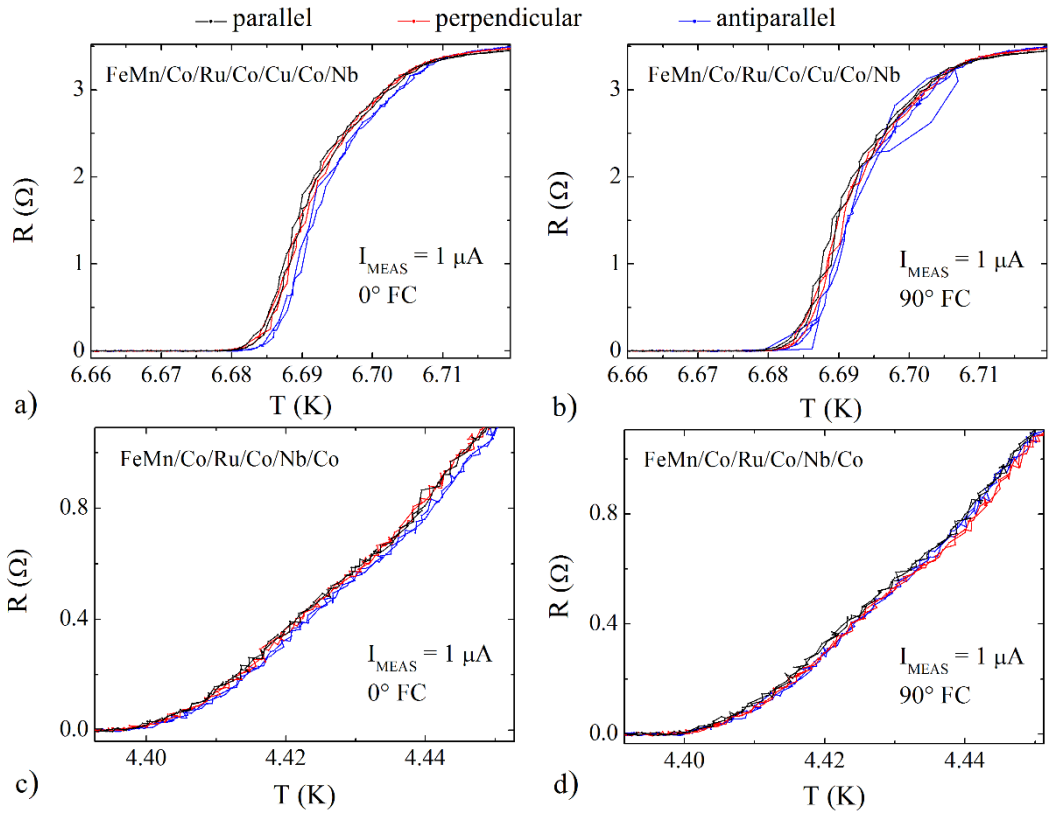

Figure 44 The $R(T)$ dependences for the FeMn/Co/Ru/Co/Cu/Co/Nb (a and b) and FeMn/Co/Ru/Co/Nb/Co (c and d) SVs measured in a 200-Oe magnetic field using a 1-μA excitation current after the SV was cooled in a 10-kOe magnetic field applied parallel (Θ_{COOL} = 0°) (a and c) and perpendicular (Θ_{COOL} = 90°) (b and d) to the SVs' long edges. The SV was rotated for obtaining parallel, antiparallel, and perpendicular magnetization configurations.

The angular dependences of the resistance for the FeMn/Co/Ru/Co/Cu/Co/Nb Figure 45(a and b) and FeMn/Co/Ru/Co/Nb/Co Figure 45(c and d) SVs were measured in a 200-Oe magnetic field using a 1-μA excitation current after the SV was cooled in a 10-kOe magnetic field applied parallel (Θ_{COOL} = 0°) (a and c) and perpendicular (Θ_{COOL} = 90°) (b and d) to the SVs' long edges. For the FeMn/Co/Ru/Co/Cu/Co/Nb SV, the $R(\Theta)$ curves look alike: the resistance demonstrates oscillation with minima at -50°

and 155°. At the same time, for the FeMn/Co/Ru/Co/Nb/Co SV, the $R(\Theta)$ curves look differently.

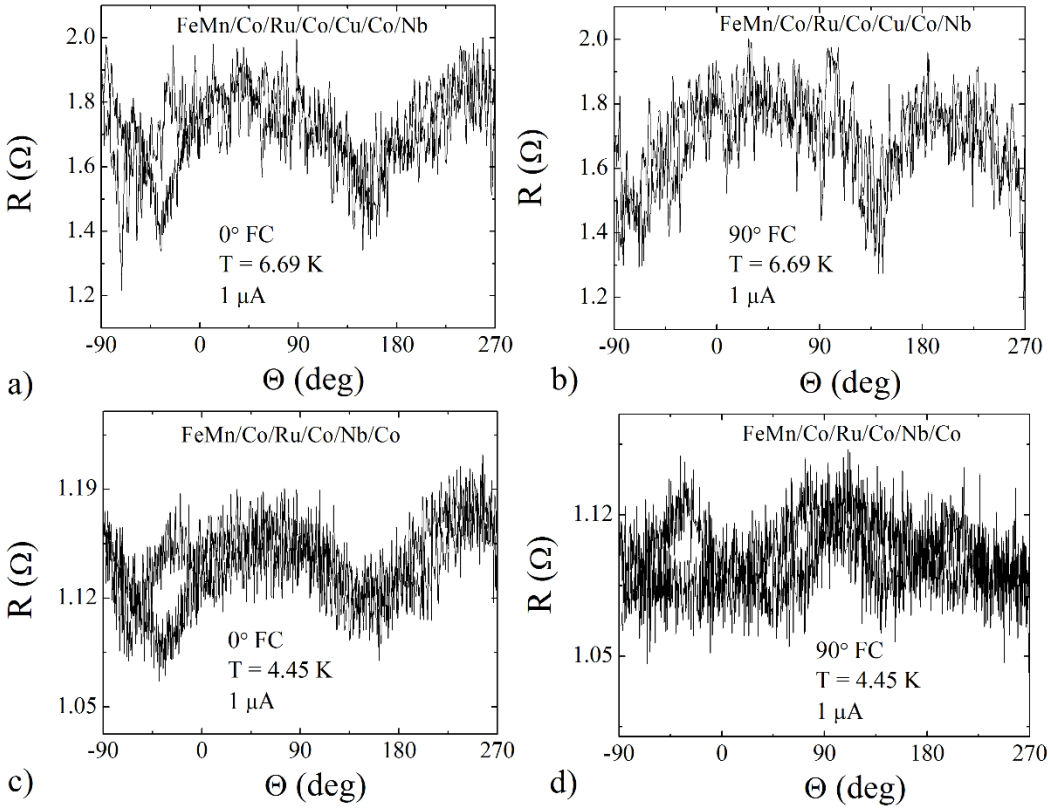

Figure 45 The angular dependences of resistance for the FeMn/Co/Ru/Co/Cu/Co/Nb (a and b) and FeMn/Co/Ru/Co/Nb/Co (c and d) SVs measured in a 200-Oe magnetic field using a 1-μA excitation current after the SV was cooled in a 10-kOe magnetic field applied parallel (Θ_{COOL} = 0°) (a and c) and perpendicular (Θ_{COOL} = 90°) (b and d) to the SVs' long edges.

The results of the T_C measurements for the Co-based SVs conducted using a cooling-field-imprinting technique are shown in Figure 46. The $R(T)$ dependences were measured using 1-μA excitation current in a 200-Oe magnetic field. In contrast to the FeMn/Py/Ru/Py/Cu/Py/Nb SV (Figure 43), here, T_C strongly depends on the angle η. Unexpectedly, $T_{\uparrow\rightarrow} > T_{\uparrow\uparrow}$, $T_{\uparrow\downarrow}$ for the FeMn/Co/Ru/Co/Cu/Co/Nb SV, and $T_{\uparrow\rightarrow} < T_{\uparrow\uparrow}$, $T_{\uparrow\downarrow}$

for the FeMn/Co/Ru/Co/Cu/Co/Nb SV. Remarkably, $T_C(180°) > T_C(0°)$ and $T_C(135°) > T_C(45°)$, which is attributed to the standard superconducting SV effect.

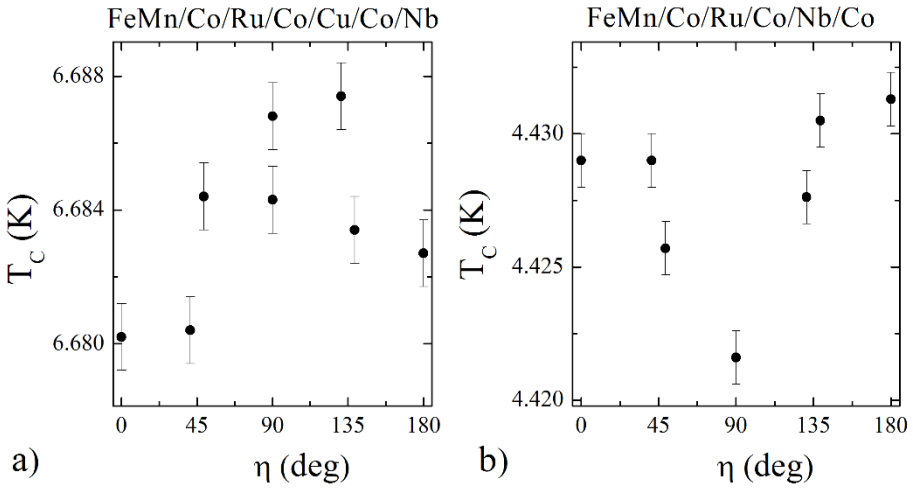

Figure 46 T_C of the (a) FeMn/Co/Ru/Co/Cu/Co/Nb and (b) FeMn/Co/Ru/Co/Nb/Co SVs as a function of the angle, η, between the magnetizations in the SAF and the Ff layer.

V.3.5 Discussion of T_C measurements of FeMn/Co/Ru/Co/Cu/Co/Nb and FeMn/Co/Ru/Co/Nb/Co valves

To some extent, the results for the Co-based SVs are contrary to those for the Py-based SV. Namely, for the Co-based SVs, the $R(T)$ measurements (with and without rotation) reveal the standard superconducting SV effect. At the same time, no signature of the effect is detected using $R(\Theta)$ measurements (Figure 45). Even more surprisingly, according to Figure 46(b), the T_C of the FeMn/Co/Ru/Co/Nb/Co SV is significantly suppressed when $\eta = 90°$. However, it is doubtful that this observation can be regarded as a clear-cut evidence of the odd-triplet pairs generation since no suppression is observed for the measurements performed with the rotation of the SV [Figure 44(c and d)]. Most likely, for the Co-based SVs, the superconducting vortices flow and T_C of the SVs are

strongly affected by the domain structure in the SAF. Cooling the SVs in different cooling fields provides different degree of non-collinearity as well as different domain structure in the SAF. The latter seems to affect T_C more than the possible generation of the odd-triplet pairing.

V.3.6 Measurements of kinetic inductance of FeMn/Co/Cu/Co/Nb valve

The superconducting vortices flow and the percolative nature of resistance complicate the analysis of T_C measurements. Hence, it is beneficial to probe the Cooper pairs depletion at temperatures significantly below T_C using KI measurements. As it was discussed previously, the most suitable way to do it is to shape the SV in the form of a wire and to measure AC complex impedance of this wire using a four-terminal technique.

KI yields a reactive impedance even though the wire is in the superconducting state. It is expected that, at 100 kHz, a 1 mA current would produce about a 1 μV-voltage drop across the wire. A series of tests was performed in order to make sure that this small voltage drop is due to the inductance impedance. First of all, according to Equation (V-3), R_W, and therefore, the voltage drop, V, must be linearly dependent on the frequency of the AC current, ν. That was confirmed by the $V(\nu)$ measurements conducted at 2 K and 5.7 K with 1-mA excitation current [Figure 47(a)]. Second, it was determined that V is also proportional to the amplitude of the AC current, I, and the voltage noise is about 0.1 μV. At 2 K, when the excitation frequency is 100 kHz, V is 533 μV. This value is much higher than 1 μV expected initially based on the assumption that all electrons are involved into the formation of Cooper pairs. However, for a real superconductor, only a small fraction of electrons is forming Cooper pairs, *i.e.*, n_S is much smaller than 10^{22} cm^{-3} assumed for

the estimate of L_K. According to Equation (V-1), the decrease in n_S leads to increase in L_k by the same factor. This explains the enhanced value of the kinetic inductance of the superconducting wire under the study.

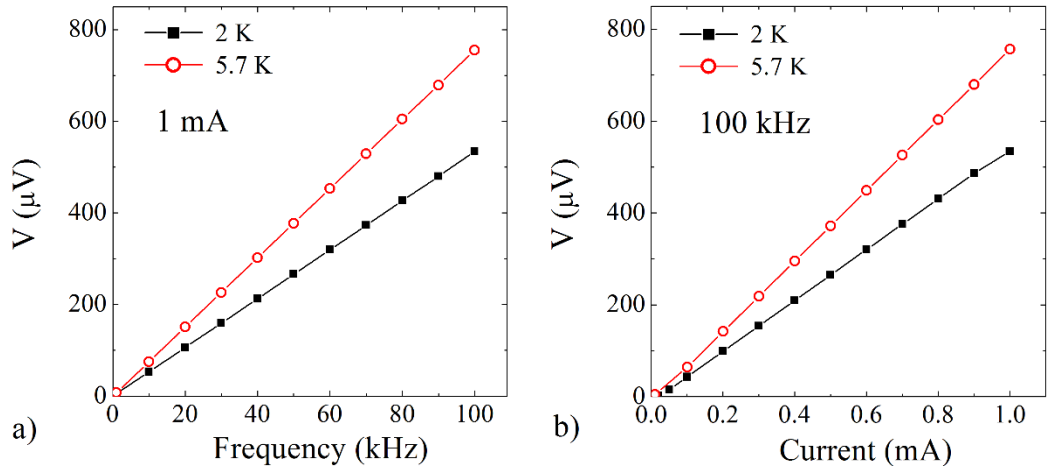

Figure 47 The voltage drop V across the FeMn/Co/Cu/Co/Nb meandering wire as (a) a function of AC current frequency when the current amplitude is 1 mA, (b) a function of the AC current amplitude when the current frequency is 100 kHz. The measurements were conducted at 2 K (black line/squares) and 5.7 K (red line/open dots).

To analyze the effect of magnetization configuration in the SV on KI, a set of the $L_K(T)$ dependences corresponding to different magnetization configurations [Figure 48(a)] as well as a set of $L_K(\Theta)$ dependences at different temperatures [Figure 48(c)] were measured after cooling down the wire in a 10-kOe magnetic field applied parallel (Θ_{COOL} = 0°) to the wire. After that, the same measurements were repeated after cooling down the wire in a 10-kOe magnetic field applied perpendicular (Θ_{COOL} = 90°) to the wire [Figure 48(b and d)].

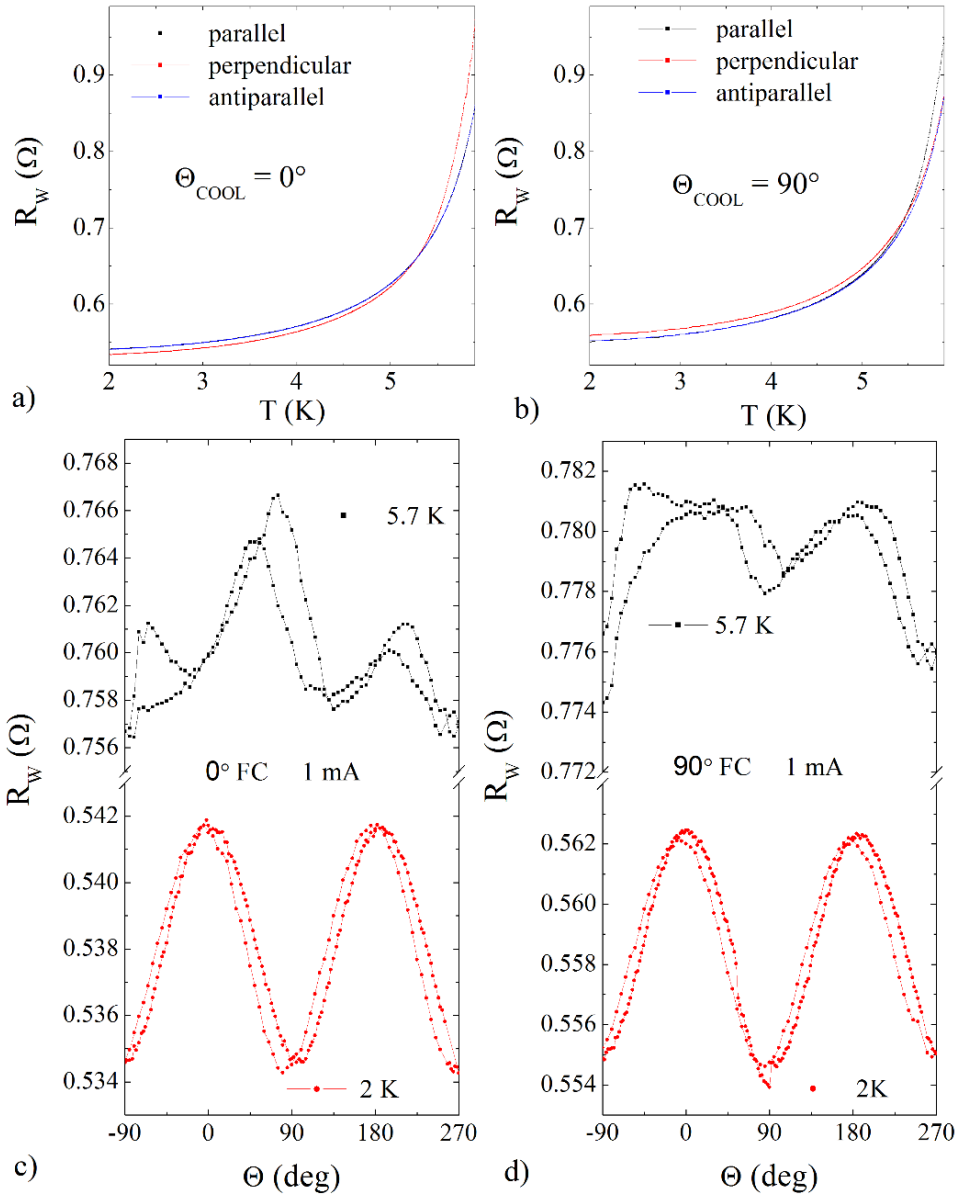

Figure 48 The KI of the FeMn/Co/Cu/Co/Nb meandering wire, L_K, as a function of temperature measured for different magnetic configurations in the SV (a and b). Angular dependences of L_K measured at different temperatures (c and d). The measurements were conducted in a 200-Oe magnetic field using a 1-mA excitation current after the wire was cooled down in a 10-kOe magnetic field applied parallel (Θ_{COOL} = 0°) (a and c) and perpendicular (Θ_{COOL} = 90°) (b and d) to the wire.

Figure 48(a and b) demonstrates that L_K rises when temperature increases. This behavior agrees with Equation (V-1): n_S goes to 0 cm^{-3} when the temperature is

approaching T_C, and hence, L_K must diverge at T_C.[245, 247] Although for the FeMn/Co/Cu/Co/Nb wire under the study, T_C at 1 mA is around 6.2 K, it was observed that when the temperature is above 5.8 K, the real component of the impedance appears. This component is most likely due to the dissipative flow of superconducting vortices in the wire. An interesting observation is that this real component does not depend on the magnetization configuration in the valve, but rather, depends on the direction of the magnetic field and the magnetizations with respect to the wire. When the magnetic field and current are perpendicular, the dissipative component of the resistance is higher than that when they are parallel or antiparallel. All subsequent KI measurements were conducted at temperatures below 5.8 K.

From Figure 48, one can see that the trend that $L_K(T)$ curves demonstrate at low temperatures (2–5.5 K) is very different from that demonstrated in the vicinity of the superconducting transition (5.5–5.8 K). Thus, at 2 K, for $\Theta_{COOL} = 0°$, L_K is maximal when the magnetizations are antiparallel, and minimal when they are perpendicular to each other [Figure 48(a, c)]. Again, this behavior could be explained by the generation of the odd-triplet pairing in the SV, but if this were the case, the same trend would be preserved when the SV was cooled down in the field perpendicular to the wire long edge ($\Theta_{COOL} = 90°$). As seen from Figure 48(b and d), it does not happen: L_K is maximal for the perpendicular configuration. At 2 K, the $L_K(\Theta)$ curves for the $\Theta_{COOL} = 0°$ and $\Theta_{COOL} = 90°$ measurements are identical. This means that at low temperatures, L_K is defined by the orientation of the sample with respect to the magnetic field direction rather than by the magnetization

configuration in the SV. In contrast, the $L_K(\Theta)$ curves measured at 5.7 K after the two cooling procedures (Θ_{COOL} = 0° and Θ_{COOL} = 90°) are very different.

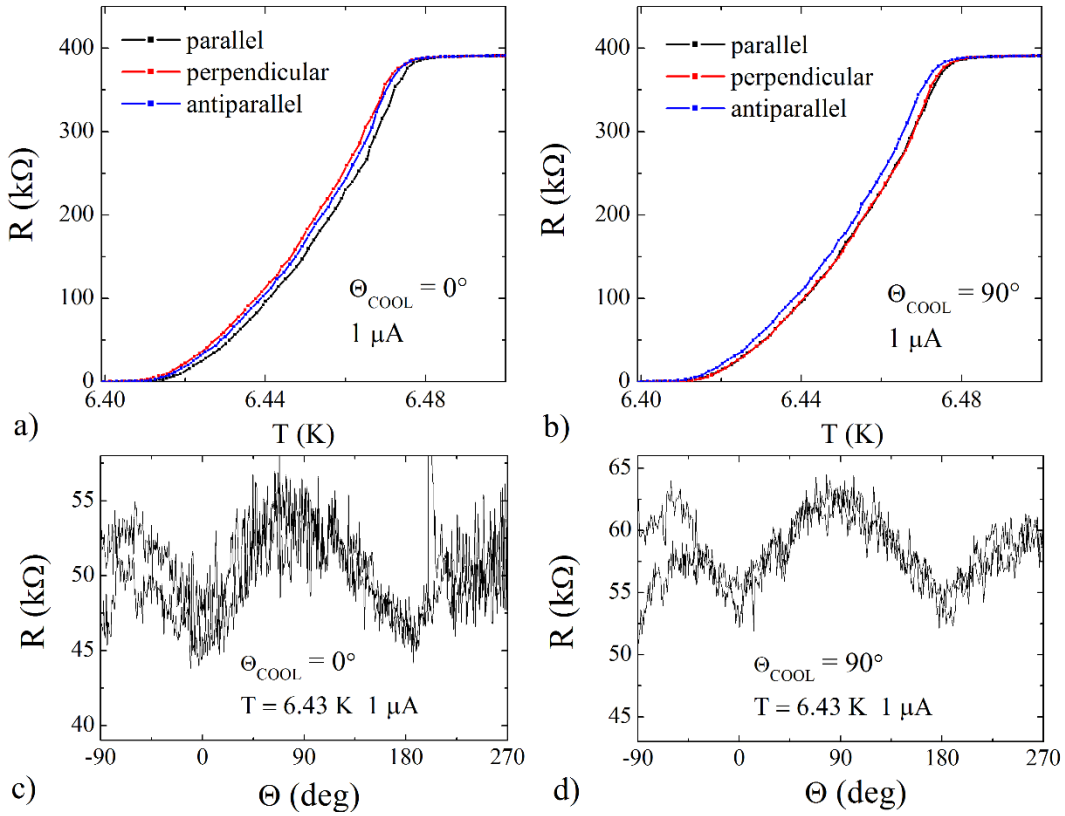

Figure 49 The $R(T)$ dependences for different magnetization configurations in the SV (a and b) and the $R(\Theta)$ dependences measured at 6.43 K (c and d) for the FeMn/Co/Cu/Co/Nb meandering wire. The measurements were conducted in a 200-Oe magnetic field using a 1-μA excitation current after the sample was cooled in a 10-kOe magnetic field applied parallel (Θ_{COOL} = 0°) (a and c) and perpendicular (Θ_{COOL} = 90°) (b and d) to the wire.

In order to understand how the magnetization configuration in the SV and the sample orientation affect T_C, $R(T)$ curves were measured in a 200-Oe magnetic field using a 1-μA excitation current for different orientations after the sample was cooled in a 10-kOe magnetic field applied parallel (Θ_{COOL} = 0°) [Figure 49(a)] and perpendicular (Θ_{COOL} = 90°) [Figure 49(b)] to the wire. A suppression of T_C for the perpendicular

magnetization configuration is observed only for Θ_{COOL} = 0°. Moreover, $R(\Theta)$ curves measured with the 1 μA current at 6.43 K (within ΔT_C-spread) [Figure 49(c and d)] demonstrate that the resistance and, therefore, T_C do not depend on the magnetization configuration. T_C is minimal when the magnetic field is perpendicular to the current in the wire.

V.3.7 Discussion of kinetic inductance measurements of FeMn/Co/Cu/Co/Nb valve

There is a correlation between $R(\Theta)$ curves measured at 6.43 K [Figure 49(c and d)] and the $L_K(\Theta)$ curves measured at 2 K (c and d). It is not surprising if one recalls that T_C and L_K are governed by the same microscopic mechanisms: the increase and decrease in n_S depending on the orientation of the SV with respect to the magnetic field or magnetization configuration in it. One can see that at 2 K, when the magnetic field is perpendicular to the wire (90°), the KI is minimal, and hence, the density of the superconducting condensate is suppressed [Figure 48(c and d)]. This, in turn, means that T_C is also suppressed in this orientation, as confirmed by the $R(\Theta)$ dependences in Figure 49(c and d).

The most important results are that the $R(\Theta)$ dependences at 6.43 K, and the $L_K(\Theta)$ curves at 2 K measured when the Co layer is pinned along the wire (Θ_{COOL} = 0°), are identical to the same curves measured when the Co layer is pinned perpendicular to the wire (Θ_{COOL} = 90°). Hence, the suppression of the superconducting condensate does not depend on the magnetization configuration in the SV. Rather, it depends on the orientation of the SV with respect to the magnetic field. This signifies that the generation of the long-

range triplet pairing either does not happen in the SV or the generation affects the condensate much less than other effects related to the sample rotation: a change in the effective magnetic field, or a redistribution of superconducting vortices.

It is noteworthy that the KI depends on the magnetization configuration for the measurements conducted at 6.43 K. However, the $L_K(\Theta)$ curves are not harmonic. Most likely, the observed change in KI is due to inhomogeneity of the samples. Since 6.43 K is very close to the critical temperature, a part of the Nb grains switch to the normal state and back when the sample rotates in the magnetic field. This switching leads to a change in the effective cross-section of the wire, which results in the angular dependence of KI observed in the experiment.

V.4 Conclusions on Odd-triplet Superconductivity

The theory predicts that a non-collinear magnetization in a superconducting SV gives rise to an emergence of the odd-triplet pairing. One of the manifestations of the effect is the suppression of the superconducting SV T_C. However, the experimental confirmation of this suppression can be very convoluted. In the "motivation" section of the chapter, the operational principles of typical superconducting SVs which consist of the fixed and free F layers were considered. It was concluded that the rotation of the SV in a permanent magnetic field can lead to the appearance of the magnetic flux through the SV's surface. This flux strongly affects the measured T_C. Hence, for detecting the change in T_C caused by the generation of the odd-triplet pairing, the SV needs to be in a fixed orientation during the measurements. New Py- and Co-based superconducting SVs with SAF which allow imprinting any predefined non-collinear magnetization configurations without

rotating the sample were designed and fabricated. Study of the superconducting SV effect using these SVs revealed that the change in T_C is due to the magnetic flux through the SV surface and the change in the domain structure is the SAF. In fact, no clear-cut evidence of odd-triplet-pairing generation in these SVs was obtained.

It was also demonstrated that the measurements of KI is a powerful tool for studying the superconducting SV effect. In particular, it enables analyzing the depletion of the superconducting condensate at different temperatures. KI measurements can be used for analyzing the T_C behavior in a superconducting SV. Generally, the T_C measurements are more time-consuming and less accurate than the measurements of the KI. The KI measurements have confirmed the results and conclusions obtained using T_C measurements: there is no evidence of the odd-triplet pairing generation in the SVs.

CHAPTER VI

SUMMARY

Inhomogeneous magnetic states occurring at the interface with magnets can lead to the emergence of new fascinating phenomena. Three different magnetic heterostructures in which different inhomogeneous magnetic states are realized, have been investigated in this dissertation.

First, it was demonstrated that for the FeMn/Cu multilayers, a strongly pinned uncompensated magnetization appears in FeMn near the bottom Cu layers, when the multilayers are cooled down in a magnetic field. This magnetization is responsible for the exchange-bias shift of the hysteresis loop. Specially designed magnetotransport measurements allowed us to demonstrate that this pinned magnetization does not reverse even in a 110 kOe magnetic field. This observation suggests that the pinned magnetization is a part of the AF spin structure of FeMn. The experimental results indicate that the pinning can be produced by the internal stress in FeMn induced by the adjacent Cu layer. This interplay between structural and magnetic properties can be used in future magneto-electronic and spintronic devices for controlling magnetization and exchange bias.

Second, the study of artificial-ferrimagnet multilayers composed of rare earth Gd and a transition-metal alloy $Ni_{81}Fe_{19}$ (Py) revealed that the antiferromagnetic coupling between the adjacent magnetic layers yields peculiar in-plane domain walls in these multilayers. These domain walls were quantitatively characterized in different temperature and magnetic fields using a combination of magnetometry, magnetotransport measurements, and micromagnetic simulations. It was concluded that the magnetization

reversal in the vicinity of the compensation temperature strongly depends on structural parameters of the multilayers. These results can be of great use for developing artificial-ferrimagnet-based memory devices with thermally assisted magnetization switching. Additionally, a significant change in magnetization and exchange stiffness with temperature, and the low magnetic anisotropy of the Py/Gd-multilayer microdisks yield different remanent states obtained upon isothermal magnetization reversal: a vortex state at low temperatures and a non-vortex (single domain) state at high temperatures.

Usually, studying inhomogeneous magnetic states implies taking into account a combination of complex phenomena related to the formation of these states. Thus, according to theory, proximity of a superconductor with an inhomogeneously magnetized ferromagnetic layer results in generation of odd-triplet Cooper pairs with a non-zero projection of total spin; this excitation, in turn, must be accompanied by a suppression of the critical temperature. However, our experimental results indicate that controlling magnetization inhomogeneity gives rise to a number of artifacts such as a change in the effective magnetic field in the superconducting layer and a modification of the domain structure of the ferromagnetic layer. In the third part of this dissertation, it was demonstrated that these artifacts affect the critical temperature much stronger than the previously proposed generation of the odd-triplet pairing would. Additionally, no sign of the odd-triplet generation was revealed using sensitive kinetic-inductance measurements. We expect that the presented experimental results will stimulate more rigorous experiments in this field, and may require some revisions of the odd-triplet-pairing theory.

REFERENCES

1. A. Hoffmann and S. D. Bader, Physical Review Applied **4**, 047001 (2015).

2. F. Hellman, A. Hoffmann, Y. Tserkovnyak, G. S. D. Beach, E. E. Fullerton, C. Leighton, A. H. MacDonald, D. C. Ralph, D. A. Arena, H. A. Dürr, P. Fischer, J. Grollier, J. P. Heremans, T. Jungwirth, A. V. Kimel, B. Koopmans, I. N. Krivorotov, S. J. May, A. K. Petford-Long, J. M. Rondinelli, N. Samarth, I. K. Schuller, A. N. Slavin, M. D. Stiles, O. Tchernyshyov, A. Thiaville, and B. L. Zink, Reviews of Modern Physics **89**, 025006 (2017).

3. L. H. Bennett and R. Watson, *Magnetic Multilayers*. (World Scientific, 1994).

4. F. Mezei, Communications on Physics (London) **1**, 81-85 (1976).

5. M. Sining, C. Yonghua, L. Feng, C. Xingfu, X. Bin, L. Puling, M. Patwari, X. Haiwen, C. Clif, B. Miller, D. Menard, B. Pant, J. Loven, K. Duxstad, L. Shaoping, Z. Zhengyong, A. Johnston, R. Lamberton, M. Gubbins, T. McLaughlin, J. Gadbois, D. Juren, B. Cross, X. Song, and P. Ryan, IEEE Transactions on Magnetics **42**, 97-102 (2006).

6. R. E. Camley and R. L. Stamps, Journal of Physics: Condensed Matter **5**, 3727 (1993).

7. R. Ranchal, Y. Choi, M. Romera, J. W. Freeland, J. L. Prieto, and D. Haskel, Physical Review B **85**, 024403 (2012).

8. M. Sawicki, W. Stefanowicz, and A. Ney, Semiconductor Science and Technology **26**, 064006 (2011).

9. J. Clarke and A. I. Braginski, *The SQUID handbook: Applications of SQUIDs and SQUID systems*. (John Wiley & Sons, 2006).

10. J. F. Ankner and G. P. Felcher, Journal of Magnetism and Magnetic Materials **200**, 741-754 (1999).

11. M. R. Fitzsimmons, B. J. Kirby, S. Roy, Z.-P. Li, I. V. Roshchin, S. K. Sinha, and I. K. Schuller, Physical Review B **75**, 214412 (2007).

12. S. Roy, M. R. Fitzsimmons, S. Park, M. Dorn, O. Petracic, I. V. Roshchin, Z.-P. Li, X. Batlle, R. Morales, A. Misra, X. Zhang, K. Chesnel, J. B. Kortright, S. K. Sinha, and I. K. Schuller, Physical Review Letters **95**, 047201 (2005).

13. A. Hoffmann, J. W. Seo, M. R. Fitzsimmons, H. Siegwart, J. Fompeyrine, J. P. Locquet, J. A. Dura, and C. F. Majkrzak, Physical Review B **66**, 220406 (2002).

14. H. Fritzsche, Z. Yamani, R. Cowley, and R. C. C. Ward, La Physique au Canada **62**, 265 (2006).

15. L. G. Parratt, Physical Review **95**, 359-369 (1954).

16. J. D. Hoffman, B. J. Kirby, J. Kwon, G. Fabbris, D. Meyers, J. W. Freeland, I. Martin, O. G. Heinonen, P. Steadman, H. Zhou, C. M. Schlepütz, M. P. M. Dean, S. G. E. te Velthuis, J.-M. Zuo, and A. Bhattacharya, Physical Review X **6**, 041038 (2016).

17. K. V. O'Donovan, J. A. Borchers, C. F. Majkrzak, O. Hellwig, and E. E. Fullerton, Physical Review Letters **88**, 067201 (2002).

18. W. H. Meiklejohn and C. P. Bean, Physical Review **105**, 904-913 (1957).

19. C. Tsang, N. Heiman, and K. Lee, Journal of Applied Physics **52**, 2471-2473 (1981).

20. S. Gangopadhyay, G. C. Hadjipanayis, C. M. Sorensen, and K. J. Klabunde, Journal of Applied Physics **73**, 6964-6966 (1993).

21. A. K. Nayak, M. Nicklas, S. Chadov, P. Khuntia, C. Shekhar, A. Kalache, M. Baenitz, Y. Skourski, V. K. Guduru, A. Puri, U. Zeitler, J. M. D. Coey, and C. Felser, Nature Materials **14**, 679-684 (2015).

22. S. S. P. Parkin, K. P. Roche, M. G. Samant, P. M. Rice, R. B. Beyers, R. E. Scheuerlein, E. J. O'Sullivan, S. L. Brown, J. Bucchigano, D. W. Abraham, Y. Lu, M. Rooks, P. L. Trouilloud, R. A. Wanner, and W. J. Gallagher, Journal of Applied Physics **85**, 5828-5833 (1999).

23. R. L. Stamps, Journal of Physics D: Applied Physics **33**, R247 (2000).

24. J. Nogués, V. Skumryev, J. Sort, S. Stoyanov, and D. Givord, Physical Review Letters **97**, 157203 (2006).

25. R. Skomski, Journal of Applied Physics **101**, 09B104 (2007).

26. V. Skumryev, S. Stoyanov, Y. Zhang, G. Hadjipanayis, D. Givord, and J. Nogues, Nature **423**, 850-853 (2003).

27. J. M. Riveiro, J. A. D. Toro, J. P. Andrés, J. A. González, T. Muñoz, and J. P. Goff, Applied Physics Letters **86**, 172503 (2005).

28. S. Maat, K. Takano, S. S. P. Parkin, and E. E. Fullerton, Physical Review Letters **87**, 087202 (2001).

29. S. Wiebel, J.-P. Jamet, N. Vernier, A. Mougin, J. Ferré, V. Baltz, B. Rodmacq, and B. Dieny, Journal of Applied Physics **100**, 043912 (2006).

30. P. Nordblad, Nature Materials **14**, 655-656 (2015).

31. E. Stoner and E. Wohlfarth, Nature **160**, 98-99 (1947).

32. F. Radu and H. Zabel, in *Magnetic Heterostructures: Advances and Perspectives in Spinstructures and Spintransport*, edited by H. Zabel and S. D. Bader (Springer Berlin Heidelberg, Berlin, Heidelberg, 2008), pp. 97-184.

33. L. Néel, Annales de physique (Paris) **2**, 61 (1967).

34. D. Mauri, H. C. Siegmann, P. S. Bagus, and E. Kay, Journal of Applied Physics **62**, 3047-3049 (1987).

35. J.-V. Kim and R. L. Stamps, Applied Physics Letters **79**, 2785-2787 (2001).

36. A. P. Malozemoff, Physical Review B **35**, 3679-3682 (1987).

37. U. Nowak, K. D. Usadel, J. Keller, P. Miltényi, B. Beschoten, and G. Güntherodt, Physical Review B **66**, 014430 (2002).

38. P. Miltényi, M. Gierlings, J. Keller, B. Beschoten, G. Güntherodt, U. Nowak, and K. D. Usadel, Physical Review Letters **84**, 4224-4227 (2000).

39. J. Keller, P. Miltényi, B. Beschoten, G. Güntherodt, U. Nowak, and K. D. Usadel, Physical Review B **66**, 014431 (2002).

40. B. Beschoten, J. Keller, P. Miltényi, and G. Güntherodt, Journal of Magnetism and Magnetic Materials **240**, 248-250 (2002).

41. N. C. Koon, Physical Review Letters **78**, 4865-4868 (1997).

42. T. C. Schulthess and W. H. Butler, Physical Review Letters **81**, 4516-4519 (1998).

43. T. Gredig, I. N. Krivorotov, P. Eames, and E. D. Dahlberg, Applied Physics Letters **81**, 1270-1272 (2002).

44. D. Paccard, C. Schlenker, O. Massenet, R. Montmory, and A. Yelon, Physica Status Solidi (b) **16**, 301-311 (1966).

45. S. G. E. te Velthuis, A. Berger, G. P. Felcher, B. K. Hill, and E. Dan Dahlberg, Journal of Applied Physics **87**, 5046-5048 (2000).

46. K. Zhang, T. Zhao, and H. Fujiwara, Journal of Applied Physics **89**, 6910-6912 (2001).

47. A. Hoffmann, Physical Review Letters **93**, 097203 (2004).

48. S. Chandra, H. Khurshid, M.-H. Phan, and H. Srikanth, Applied Physics Letters **101**, 232405 (2012).

49. R. Florin, W. Andreas, T.-B. Katharina, and Z. Hartmut, Journal of Physics: Condensed Matter **18**, L29 (2006).

50. M. Ali, P. Adie, C. H. Marrows, D. Greig, B. J. Hickey, and R. L. Stamps, Nature Materials **6**, 70-75 (2007).

51. M. Kiwi, Journal of Magnetism and Magnetic Materials **234**, 584-595 (2001).

52. A. E. Berkowitz and K. Takano, Journal of Magnetism and Magnetic Materials **200**, 552-570 (1999).

53. J. Nogués and I. K. Schuller, Journal of Magnetism and Magnetic Materials **192**, 203-232 (1999).

54. W. Zhang and K. M. Krishnan, Materials Science and Engineering: R: Reports **105**, 1-20 (2016).

55. J. Nogués, J. Sort, V. Langlais, V. Skumryev, S. Suriñach, J. S. Muñoz, and M. D. Baró, Physics Reports **422**, 65-117 (2005).

56. M. Charilaou and F. Hellman, Journal of Applied Physics **117**, 083907 (2015).

57. K. D. Belashchenko, Physical Review Letters **105**, 147204 (2010).

58. S. Javadi, M. Habibi, M. Ghoranneviss, S. Lee, S. H. Saw, and R. A. Behbahani, Physica Scripta **86**, 025801 (2012).

59. H. F. Kirby, T. M. Eggers, P. B. Jayathilaka, S. M. Campbell, and C. W. Miller, Journal of Magnetism and Magnetic Materials **324**, 4151-4154 (2012).

60. A. L. Patterson, Physical Review **56**, 978-982 (1939).

61. L. Ritchie, X. Liu, S. Ingvarsson, G. Xiao, J. Du, and J. Q. Xiao, Journal of Magnetism and Magnetic Materials **247**, 187-190 (2002).

62. D. Kaya, P. N. Lapa, P. Jayathilaka, H. Kirby, C. W. Miller, and I. V. Roshchin, Journal of Applied Physics **113**, 17D717 (2013).

63. P. N. Lapa, I. V. Roshchin, J. Ding, J. E. Pearson, V. Novosad, J. S. Jiang, and A. Hoffmann, Physical Review B **95**, 020409 (2017).

64. H. Ohno and M. Mekata, Journal of the Physical Society of Japan **31**, 102-108 (1971).

65. A. M. Van der Kraan and K. H. J. Buschow, Physica B+C **138**, 55-62 (1986).

66. G. Longworth and R. Jain, Journal of Physics F: Metal Physics **8**, 351 (1978).

67. J. Restrepo, J. M. Grenèche, A. Hernando, P. Crespo, M. A. García, F. J. Palomares, and J. M. González, Journal of Magnetism and Magnetic Materials **290–291**, 602-605 (2005).

68. K. Sumiyama, T. Yoshitake, and Y. Nakamura, Transactions of the Japan Institute of Metals **26**, 217-224 (1985).

69. P. N. Lapa, A. Glavic, H. Ambaye, V. Lauter, K. D. Belashchenko, T. Eggers, C. W. Miller, and I. V. Roshchin, IEEE Magnetics Letters (unpublished).

70. R. Coehoorn, in *Handbook of Magnetic Materials* (Elsevier, 2003), Vol. 15, pp. 73-77.

71. R. W. Schmitt and I. S. Jacobs, Journal of Physics and Chemistry of Solids **3**, 324-337 (1957).

72. P. Gibbs, T. M. Harders, and J. H. Smith, Journal of Physics F: Metal Physics **15**, 213 (1985).

73. D. Meneghetti and S. S. Sidhu, Physical Review **105**, 130-135 (1957).

74. H. Ohldag, A. Scholl, F. Nolting, E. Arenholz, S. Maat, A. T. Young, M. Carey, and J. Stöhr, Physical Review Letters **91**, 017203 (2003).

75. J. B. Tracy, D. N. Weiss, D. P. Dinega, and M. G. Bawendi, Physical Review B **72**, 064404 (2005).

76. M. P. Proenca, C. T. Sousa, A. M. Pereira, P. B. Tavares, J. Ventura, M. Vazquez, and J. P. Araujo, Physical Chemistry Chemical Physics **13**, 9561-9567 (2011).

77. P. Lv, Y. Zhang, R. Xu, J.-C. Nie, and L. He, Journal of Applied Physics **111**, 013910 (2012).

78. J. Geshev, Journal of Magnetism and Magnetic Materials **320**, 600-602 (2008).

79. R. M. Bozorth, Physical Review **70**, 923-932 (1946).

80. W. Zhang, M. B. Jungfleisch, W. Jiang, J. E. Pearson, A. Hoffmann, F. Freimuth, and Y. Mokrousov, Physical Review Letters **113**, 196602 (2014).

81. J. K. Kim, S. W. Kim, K. A. Lee, B. K. Kim, J. H. Kim, S. S. Lee, D. G. Hwang, C. G. Kim, and C. O. Kim, Journal of Applied Physics **93**, 7714-7716 (2003).

82. L. Wang, S. G. Wang, S. Rizwan, Q. H. Qin, and X. F. Han, Applied Physics Letters **95**, 152512 (2009).

83. B. G. Park, J. Wunderlich, X. Martí, V. Holý, Y. Kurosaki, M. Yamada, H. Yamamoto, A. Nishide, J. Hayakawa, H. Takahashi, A. B. Shick, and T. Jungwirth, Nature Materials **10**, 347-351 (2011).

84. I. I. Lifanov and N. G. Sherstyukov, Measurement Techniques **11**, 1653-1659 (1968).

85. K. E. Petersen, Proceedings of the IEEE **70**, 420-457 (1982).

86. J. C. Cooper and B. Yates, Cryogenics **10**, 442 (1970).

87. G. K. White, Proceedings of the Physical Society **86**, 159 (1965).

88. G. K. White, Cryogenics **2**, 292-296 (1962).

89. K. G. Lyon, G. L. Salinger, C. A. Swenson, and G. K. White, Journal of Applied Physics **48**, 865-868 (1977).

90. H. Tada, A. E. Kumpel, R. E. Lathrop, J. B. Slanina, P. Nieva, P. Zavracky, I. N. Miaoulis, and P. Y. Wong, Journal of Applied Physics **87**, 4189-4193 (2000).

91. E. Linville, D. Han, J. Judy, J. Sivertson, and S. Mao, IEEE Transactions on Magnetics **34**, 894-896 (1998).

92. W. Lin, B. Wang, T. Chen, L. Lin, Y. Liao, W. Pan, N. Jih, K. Song, and M. Lin, Applied Physics Letters **90**, 052502 (2007).

93. W. Pan, D. Sander, M. Lin, and J. Kirschner, Physical Review B **68**, 224419 (2003).

94. K. Nakamura, T. Ito, A. J. Freeman, L. Zhong, and J. Fernandez-de-Castro, Physical Review B **67**, 014405 (2003).

95. G. M. Stocks, W. A. Shelton, T. C. Schulthess, B. Újfalussy, W. H. Butler, and A. Canning, Journal of Applied Physics **91**, 7355-7357 (2002).

96. A. F. Andreev, Journal of Experimental and Theoretical Physics Letters **63**, 758-762 (1996).

97. G. G. Stoney, Proceedings of the Royal Society of London. Series A **82**, 172-175 (1909).

98. E. H. Yang and S. S. Yang, Sensors and Actuators A: Physical **54**, 684-689 (1996).

99. G. Urbain, P. Weiss, and F. Trombe, Comptes Rendus **200**, 2132-2134 (1935).

100. J. Jensen and A. R. Mackintosh, *Rare earth magnetism: structures and excitations*. (Oxford: Clarendon Press; New York: Oxford University Press, 1991).

101. M. A. Ruderman and C. Kittel, Physical Review **96**, 99-102 (1954).

102. R. Wu and A. J. Freeman, Journal of Magnetism and Magnetic Materials **99**, 81-84 (1991).

103. A. Heys and P. E. Donovan, Journal of Magnetism and Magnetic Materials **126**, 326-328 (1993).

104. A. Heys, P. E. Donovan, A. K. Petford-Long, and R. Cywinski, Journal of Magnetism and Magnetic Materials **131**, 265-272 (1994).

105. A. Barth, F. Treubel, M. Marszałek, W. Evenson, O. Hellwig, C. Borschel, M. Albrecht, and G. Schatz, Journal of Physics: Condensed Matter **20**, 395232 (2008).

106. M. Taborelli, R. Allenspach, G. Boffa, and M. Landolt, Physical Review Letters **56**, 2869-2872 (1986).

107. D. Haskel, G. Srajer, J. C. Lang, J. Pollmann, C. S. Nelson, J. S. Jiang, and S. D. Bader, Physical Review Letters **87**, 207201 (2001).

108. J. W. A. Robinson, F. Chiodi, M. Egilmez, G. B. Halász, and M. G. Blamire, Scientific Reports **2**, 699 (2012).

109. T. Katayama, M. Hirano, Y. Koizumi, K. Kawanishi, and T. Tsushima, IEEE Transactions on Magnetics **13**, 1603-1605 (1977).

110. M. Nawate, K. Doi, and S. Honda, Journal of Magnetism and Magnetic Materials **126**, 279-281 (1993).

111. T. Eimüller, R. Kalchgruber, P. Fischer, G. Schütz, P. Guttmann, G. Schmahl, M. Köhler, K. Prügl, M. Scholz, F. Bammes, and G. Bayreuther, Journal of Applied Physics **87**, 6478-6480 (2000).

112. S. Tomonori, O. Kouji, O. Kenshou, O. Yutaka, M. Shunsuke, and S. Yoshifumi, Japanese Journal of Applied Physics **13**, 201 (1974).

113. J. C. T. Lee, J. J. Chess, S. A. Montoya, X. Shi, N. Tamura, S. K. Mishra, P. Fischer, B. J. McMorran, S. K. Sinha, E. E. Fullerton, S. D. Kevan, and S. Roy, Applied Physics Letters **109**, 022402 (2016).

114. S. A. Montoya, S. Couture, J. J. Chess, J. C. T. Lee, N. Kent, D. Henze, S. K. Sinha, M.-Y. Im, S. D. Kevan, P. Fischer, B. J. McMorran, V. Lomakin, S. Roy, and E. E. Fullerton, arXiv:1608.01368.

115. K. Cherifi, C. Dufour, P. Bauer, G. Marchal, and P. Mangin, Physical Review B **44**, 7733-7736 (1991).

116. R. E. Camley and D. R. Tilley, Physical Review B **37**, 3413-3421 (1988).

117. C. D. Stanciu, F. Hansteen, A. V. Kimel, A. Kirilyuk, A. Tsukamoto, A. Itoh, and T. Rasing, Physical Review Letters **99**, 047601 (2007).

118. S. Mangin, M. Gottwald, C. H. Lambert, D. Steil, V. Uhlíř, L. Pang, M. Hehn, S. Alebrand, M. Cinchetti, G. Malinowski, Y. Fainman, M. Aeschlimann, and E. E. Fullerton, Nature Materials **13**, 286-292 (2014).

119. T. A. Ostler, J. Barker, R. F. L. Evans, R. W. Chantrell, U. Atxitia, O. Chubykalo-Fesenko, S. El Moussaoui, L. Le Guyader, E. Mengotti, L. J. Heyderman, F. Nolting, A. Tsukamoto, A. Itoh, D. Afanasiev, B. A. Ivanov, A. M. Kalashnikova, K. Vahaplar, J. Mentink, A. Kirilyuk, T. Rasing, and A. V. Kimel, Nature Communications **3**, 666 (2012).

120. A. Kirilyuk, A. V. Kimel, and T. Rasing, Reports on Progress in Physics **76**, 026501 (2013).

121. C. Xu, T. A. Ostler, and R. W. Chantrell, Physical Review B **93**, 054302 (2016).

122. C.-H. Lambert, S. Mangin, B. S. D. C. S. Varaprasad, Y. K. Takahashi, M. Hehn, M. Cinchetti, G. Malinowski, K. Hono, Y. Fainman, M. Aeschlimann, and E. E. Fullerton, Science **345**, 1337-1340 (2014).

123. R. Morales, J. I. Martín, and J. M. Alameda, Physical Review B **70**, 174440 (2004).

124. C. Blanco-Roldán, Y. Choi, C. Quirós, S. M. Valvidares, R. Zarate, M. Vélez, J. M. Alameda, D. Haskel, and J. I. Martín, Physical Review B **92**, 224433 (2015).

125. S. Honda, M. Nawate, and I. Sakamoto, Journal of Applied Physics **79**, 365-372 (1996).

126. R. Ranchal, C. Aroca, M. Maicas, and E. López, Journal of Applied Physics **102**, 053904 (2007).

127. R. Ranchal, C. Aroca, and E. López, Journal of Applied Physics **100**, 103903 (2006).

128. P. N. Lapa, J. Ding, J. E. Pearson, V. Novosad, J. S. Jiang, and A. Hoffmann, arXiv:1703.08626 (2017).

129. K. Y. Guslienko, Journal of Nanoscience and Nanotechnology **8**, 2745-2760 (2008).

130. T. Shinjo, T. Okuno, R. Hassdorf, K. Shigeto, and T. Ono, Science **289**, 930-932 (2000).

131. K. Bussmann, G. A. Prinz, S.-F. Cheng, and D. Wang, Applied Physics Letters **75**, 2476-2478 (1999).

132. R. Hertel, Nature Nanotechnology **8**, 318-320 (2013).

133. K. Y. Guslienko, V. Novosad, Y. Otani, H. Shima, and K. Fukamichi, Applied Physics Letters **78**, 3848-3850 (2001).

134. K. Y. Guslienko, G. N. Kakazei, J. Ding, X. M. Liu, and A. O. Adeyeye, Scientific Reports **5**, 13881 (2015).

135. K. Y. Guslienko, X. F. Han, D. J. Keavney, R. Divan, and S. D. Bader, Physical Review Letters **96**, 067205 (2006).

136. V. Novosad, F. Y. Fradin, P. E. Roy, K. S. Buchanan, K. Y. Guslienko, and S. D. Bader, Physical Review B **72**, 024455 (2005).

137. K. Y. Guslienko, V. Novosad, Y. Otani, H. Shima, and K. Fukamichi, Physical Review B **65**, 024414 (2001).

138. M. Urbánek, V. Uhlíř, C.-H. Lambert, J. J. Kan, N. Eibagi, M. Vaňatka, L. Flajšman, R. Kalousek, M.-Y. Im, P. Fischer, T. Šikola, and E. E. Fullerton, Physical Review B **91**, 094415 (2015).

139. V. L. Mironov, B. A. Gribkov, A. A. Fraerman, S. A. Gusev, S. N. Vdovichev, I. R. Karetnikova, I. M. Nefedov, and I. A. Shereshevsky, Journal of Magnetism and Magnetic Materials **312**, 153-157 (2007).

140. P. Vavassori, M. Grimsditch, V. Metlushko, N. Zaluzec, and B. Ilic, Applied Physics Letters **86**, 072507 (2005).

141. M. Rahm, J. Biberger, V. Umansky, and D. Weiss, Journal of Applied Physics **93**, 7429-7431 (2003).

142. G. Mihajlović, M. S. Patrick, J. E. Pearson, V. Novosad, S. D. Bader, M. Field, G. J. Sullivan, and A. Hoffmann, Applied Physics Letters **96**, 112501 (2010).

143. I. V. Roshchin, C.-P. Li, H. Suhl, X. Batlle, S. Roy, S. K. Sinha, S. Park, R. Pynn, M. R. Fitzsimmons, J. Mejía-López, D. Altbir, A. H. Romero, and I. K. Schuller, Europhysics Letters **86**, 67008 (2009).

144. K. S. Buchanan, K. Y. Guslienko, A. Doran, A. Scholl, S. D. Bader, and V. Novosad, Physical Review B **72**, 134415 (2005).

145. J. Wu, D. Carlton, E. Oelker, J. S. Park, E. Jin, E. Arenholz, A. Scholl, H. Chanyong, J. Bokor, and Z. Q. Qiu, Journal of Physics: Condensed Matter **22**, 342001 (2010).

146. J. Sort, K. S. Buchanan, V. Novosad, A. Hoffmann, G. Salazar-Alvarez, A. Bollero, M. D. Baró, B. Dieny, and J. Nogués, Physical Review Letters **97**, 067201 (2006).

147. S. O. Parreiras and M. D. Martins, Physics Procedia **75**, 1142-1149 (2015).

148. H. Shima, V. Novosad, Y. Otani, K. Fukamichi, N. Kikuchi, O. Kitakamai, and Y. Shimada, Journal of Applied Physics **92**, 1473-1476 (2002).

149. C. A. Ross, H. I. Smith, T. Savas, M. Schattenburg, M. Farhoud, M. Hwang, M. Walsh, M. C. Abraham, and R. J. Ram, Journal of Vacuum Science & Technology B **17**, 3168-3176 (1999).

150. P. N. Lapa, J. Ding, C. Phatak, J. E. Pearson, J. S. Jiang, A. Hoffmann, and V. Novosad, arXiv:1705.06398 (2017).

151. G. Scheunert, W. R. Hendren, C. Ward, and R. M. Bowman, Applied Physics Letters **101**, 142407 (2012).

152. A. K. Petford-Long and J. N. Chapman, in *Magnetic Microscopy of Nanostructures*, edited by H. Hopster and H. P. Oepen (Springer Berlin Heidelberg, Berlin, Heidelberg, 2005), pp. 67-86.

153. D. Larbalestier, A. Gurevich, D. M. Feldmann, and A. Polyanskii, Nature **414**, 368-377 (2001).

154. L. T. Baczewski, R. Kalinowski, and A. Wawro, Journal of Magnetism and Magnetic Materials **177**, 1305-1307 (1998).

155. M. Vaezzadeh, B. George, and G. Marchal, Physical Review B **50**, 6113-6118 (1994).

156. K. Takanashi, Y. Kamiguchi, H. Fujimori, and H. Motokawa, Journal of the Physical Society of Japan **61**, 3721-3731 (1992).

157. J. Colino, J. P. Andrés, J. M. Riveiro, J. L. Martínez, C. Prieto, and J. L. Sacedón, Physical Review B **60**, 6678-6684 (1999).

158. K. Takanashi, H. Kurokawa, and H. Fujimori, Applied Physics Letters **63**, 1585-1587 (1993).

159. D. LaGraffe, P. A. Dowben, and M. Onellion, Journal of Vacuum Science & Technology A **8**, 2738-2742 (1990).

160. T. McGuire and R. Gambino, IEEE Transactions on Magnetics **14**, 838-840 (1978).

161. R. Ranchal, C. Aroca, M. Sánchez, P. Sánchez, and E. López, Applied Physics A **82**, 697-701 (2006).

162. R. E. Camley, Physical Review B **35**, 3608-3611 (1987).

163. Y. Jian, Solid State Communications **74**, 1221-1224 (1990).

164. R. E. Camley, Physical Review B **39**, 12316-12319 (1989).

165. R. Mallik, E. V. Sampathkumaran, P. L. Paulose, and V. Nagarajan, Physical Review B **55**, R8650-R8653 (1997).

166. A. Vansteenkiste, J. Leliaert, M. Dvornik, M. Helsen, F. Garcia-Sanchez, and B. V. Waeyenberge, AIP Advances **4**, 107133 (2014).

167. R. K. Dumas, K. Liu, C.-P. Li, I. V. Roshchin, and I. K. Schuller, Applied Physics Letters **91**, 202501 (2007).

168. M. S. Dresselhaus and I. L. Thomas, Nature **414**, 332-337 (2001).

169. P. F. Ribeiro, B. K. Johnson, M. L. Crow, A. Arsoy, and Y. Liu, Proceedings of the IEEE **89**, 1744-1756 (2001).

170. M. H. Devoret, A. Wallraff, and J. M. Martinis, arXiv:cond-mat/0411174.

171. K. D. Irwin and G. C. Hilton, in *Cryogenic Particle Detection*, edited by C. Enss (Springer Berlin Heidelberg, Berlin, Heidelberg, 2005), pp. 63-150.

172. A. C. Basaran, J. E. Villegas, J. S. Jiang, A. Hoffmann, and I. K. Schuller, MRS Bulletin **40**, 925-932 (2015).

173. J. G. Bednorz and K. A. Müller, Zeitschrift für Physik B Condensed Matter **64**, 189-193 (1986).

174. W. L. McMillan, Physical Review **167**, 331-344 (1968).

175. C. C. Tsuei and J. R. Kirtley, Reviews of Modern Physics **72**, 969-1016 (2000).

176. M. R. Norman, Science **332**, 196-200 (2011).

177. A. D. Caviglia, S. Gariglio, N. Reyren, D. Jaccard, T. Schneider, M. Gabay, S. Thiel, G. Hammerl, J. Mannhart, and J. M. Triscone, Nature **456**, 624-627 (2008).

178. B. Baek, W. H. Rippard, M. R. Pufall, S. P. Benz, S. E. Russek, H. Rogalla, and P. D. Dresselhaus, Physical Review Applied **3**, 011001 (2015).

179. A. F. Andreev, Journal of Experimental and Theoretical Physics Letters **19**, 1228-1231 (1964).

180. P. G. De Gennes, Reviews of Modern Physics **36**, 225-237 (1964).

181. P. G. De Gennes, *Superconductivity of metals and alloys*. (Addison-Wesley, 1989).

182. H. Meissner, Physical Review **117**, 672-680 (1960).

183. F. S. Bergeret, A. F. Volkov, and K. B. Efetov, Reviews of Modern Physics **77**, 1321-1373 (2005).

184. B. D. Josephson, Physics Letters **1**, 251-253 (1962).

185. B. D. Josephson, Reviews of Modern Physics **46**, 251-254 (1974).

186. P. W. Anderson and J. M. Rowell, Physical Review Letters **10**, 230-232 (1963).

187. T. Mühge, N. N. Garif'yanov, Y. V. Goryunov, G. G. Khaliullin, L. R. Tagirov, K. Westerholt, I. A. Garifullin, and H. Zabel, Physical Review Letters **77**, 1857-1860 (1996).

188. Y. V. Fominov, N. M. Chtchelkatchev, and A. A. Golubov, Physical Review B **66**, 014507 (2002).

189. J. S. Jiang, D. Davidović, D. H. Reich, and C. L. Chien, Physical Review Letters **74**, 314-317 (1995).

190. C. Attanasio, C. Coccorese, L. V. Mercaldo, S. L. Prischepa, M. Salvato, and L. Maritato, Physical Review B **57**, 14411-14415 (1998).

191. Y. Obi, H. Wakou, M. Ikebe, and H. Fujimori, Czechoslovak Journal of Physics **46**, 721-722 (1996).

192. J. Aarts, J. M. E. Geers, E. Brück, A. A. Golubov, and R. Coehoorn, Physical Review B **56**, 2779-2787 (1997).

193. T. Mühge, K. Westerholt, H. Zabel, N. N. Garif'yanov, Y. V. Goryunov, I. A. Garifullin, and G. G. Khaliullin, Physical Review B **55**, 8945-8954 (1997).

194. V. V. Ryazanov, V. A. Oboznov, A. Y. Rusanov, A. V. Veretennikov, A. A. Golubov, and J. Aarts, Physical Review Letters **86**, 2427-2430 (2001).

195. Y. Blum, A. Tsukernik, M. Karpovski, and A. Palevski, Physical Review Letters **89**, 187004 (2002).

196. F. S. Bergeret, A. F. Volkov, and K. B. Efetov, Physical Review Letters **86**, 4096-4099 (2001).

197. F. S. Bergeret, A. F. Volkov, and K. B. Efetov, Physical Review B **68**, 064513 (2003).

198. V. L. Berezinskii, Journal of Experimental and Theoretical Physics Letters **20**, 287-289 (1974).

199. A. Di Bernardo, S. Diesch, Y. Gu, J. Linder, G. Divitini, C. Ducati, E. Scheer, M. G. Blamire, and J. W. A. Robinson, Nature Communications **6**, 8053 (2015).

200. I. Sosnin, H. Cho, V. T. Petrashov, and A. F. Volkov, Physical Review Letters **96**, 157002 (2006).

201. Y. Gu, J. W. A. Robinson, M. Bianchetti, N. A. Stelmashenko, D. Astill, F. M. Grosche, J. L. MacManus-Driscoll, and M. G. Blamire, APL Materials **2**, 046103 (2014).

202. A. I. Buzdin, Reviews of Modern Physics **77**, 935-976 (2005).

203. D. Sprungmann, K. Westerholt, H. Zabel, M. Weides, and H. Kohlstedt, Physical Review B **82**, 060505 (2010).

204. T. S. Khaire, M. A. Khasawneh, W. P. Pratt, and N. O. Birge, Physical Review Letters **104**, 137002 (2010).

205. J. W. A. Robinson, J. D. S. Witt, and M. G. Blamire, Science **329**, 59-61 (2010).

206. K. Halterman and O. T. Valls, Physical Review B **65**, 014509 (2001).

207. K. Halterman and O. T. Valls, Physical Review B **66**, 224516 (2002).

208. I. Baladié and A. Buzdin, Physical Review B **64**, 224514 (2001).

209. M. Zareyan, W. Belzig, and Y. V. Nazarov, Physical Review Letters **86**, 308-311 (2001).

210. F. S. Bergeret, A. F. Volkov, and K. B. Efetov, Physical Review B **65**, 134505 (2002).

211. T. Kontos, M. Aprili, J. Lesueur, and X. Grison, Physical Review Letters **86**, 304-307 (2001).

212. T. Yokoyama, Y. Tanaka, and A. A. Golubov, Physical Review B **75**, 134510 (2007).

213. M. Knežević, L. Trifunovic, and Z. Radović, Physical Review B **85**, 094517 (2012).

214. L. R. Tagirov, Physical Review Letters **83**, 2058-2061 (1999).

215. A. I. Buzdin, A. V. Vedyayev, and N. V. Ryzhanova, Europhysics Letters **48**, 686 (1999).

216. R. G. Deminov, L. R. Tagirov, R. R. Gaifullin, T. Y. Karminskaya, M. Y. Kupriyanov, Y. V. Fominov, and A. A. Golubov, Journal of Magnetism and Magnetic Materials **373**, 16-17 (2015).

217. Y. V. Fominov, A. A. Golubov, T. Y. Karminskaya, M. Y. Kupriyanov, R. G. Deminov, and L. R. Tagirov, Journal of Experimental and Theoretical Physics Letters **91**, 308-313 (2010).

218. G. Deutscher and F. Meunier, Physical Review Letters **22**, 395-396 (1969).

219. I. C. Moraru, W. P. Pratt, and N. O. Birge, Physical Review B **74**, 220507 (2006).

220. P. Cadden-Zimansky, Y. B. Bazaliy, L. M. Litvak, J. S. Jiang, J. Pearson, J. Y. Gu, C.-Y. You, M. R. Beasley, and S. D. Bader, Physical Review B **77**, 184501 (2008).

221. J. Y. Gu, C. Y. You, J. S. Jiang, J. Pearson, Y. B. Bazaliy, and S. D. Bader, Physical Review Letters **89**, 267001 (2002).

222. A. Potenza and C. H. Marrows, Physical Review B **71**, 180503 (2005).

223. K. Westerholt, D. Sprungmann, H. Zabel, R. Brucas, B. Hjörvarsson, D. A. Tikhonov, and I. A. Garifullin, Physical Review Letters **95**, 097003 (2005).

224. I. C. Moraru, W. P. Pratt, and N. O. Birge, Physical Review Letters **96**, 037004 (2006).

225. G.-X. Miao, A. V. Ramos, and J. S. Moodera, Physical Review Letters **101**, 137001 (2008).

226. P. V. Leksin, N. N. Garif'yanov, I. A. Garifullin, J. Schumann, H. Vinzelberg, V. Kataev, R. Klingeler, O. G. Schmidt, and B. Büchner, Applied Physics Letters **97**, 102505 (2010).

227. P. V. Leksin, N. N. Garif'yanov, I. A. Garifullin, J. Schumann, V. Kataev, O. G. Schmidt, and B. Büchner, Physical Review Letters **106**, 067005 (2011).

228. P. V. Leksin, N. N. Garif'yanov, I. A. Garifullin, J. Schumann, V. Kataev, O. G. Schmidt, and B. Büchner, Physical Review B **85**, 024502 (2012).

229. G. Nowak, K. Westerholt, and H. Zabel, Superconductor Science and Technology **26**, 025004 (2013).

230. B. Li, N. Roschewsky, B. A. Assaf, M. Eich, M. Epstein-Martin, D. Heiman, M. Münzenberg, and J. S. Moodera, Physical Review Letters **110**, 097001 (2013).

231. V. I. Zdravkov, J. Kehrle, G. Obermeier, D. Lenk, H. A. Krug von Nidda, C. Müller, M. Y. Kupriyanov, A. S. Sidorenko, S. Horn, R. Tidecks, and L. R. Tagirov, Physical Review B **87**, 144507 (2013).

232. N. Banerjee, C. B. Smiet, R. G. J. Smits, A. Ozaeta, F. S. Bergeret, M. G. Blamire, and J. W. A. Robinson, Nature Communications **5**, 3048 (2014).

233. Y. Gu, G. B. Halász, J. W. A. Robinson, and M. G. Blamire, Physical Review Letters **115**, 067201 (2015).

234. A. A. Jara, C. Safranski, I. N. Krivorotov, C.-T. Wu, A. N. Malmi-Kakkada, O. T. Valls, and K. Halterman, Physical Review B **89**, 184502 (2014).

235. G. Nowak, H. Zabel, K. Westerholt, I. Garifullin, M. Marcellini, A. Liebig, and B. Hjörvarsson, Physical Review B **78**, 134520 (2008).

236. J. Zhu, I. N. Krivorotov, K. Halterman, and O. T. Valls, Physical Review Letters **105**, 207002 (2010).

237. M. G. Flokstra, T. C. Cunningham, J. Kim, N. Satchell, G. Burnell, P. J. Curran, S. J. Bending, C. J. Kinane, J. F. K. Cooper, S. Langridge, A. Isidori, N. Pugach, M. Eschrig, and S. L. Lee, Physical Review B **91**, 060501 (2015).

238. X. L. Wang, A. Di Bernardo, N. Banerjee, A. Wells, F. S. Bergeret, M. G. Blamire, and J. W. A. Robinson, Physical Review B **89**, 140508 (2014).

239. P. Fuchs, U. Ramsperger, A. Vaterlaus, and M. Landolt, Physical Review B **55**, 12546-12551 (1997).

240. L. Zhang, J. Cao, Y. Wang, J. Bai, and F. Wei, Materials Letters **73**, 50-52 (2012).

241. G. Binasch, P. Grünberg, F. Saurenbach, and W. Zinn, Physical Review B **39**, 4828-4830 (1989).

242. M. N. Baibich, J. M. Broto, A. Fert, F. N. Van Dau, F. Petroff, P. Etienne, G. Creuzet, A. Friederich, and J. Chazelas, Physical Review Letters **61**, 2472-2475 (1988).

243. S. Bandiera, R. C. Sousa, Y. Dahmane, C. Ducruet, C. Portemont, V. Baltz, S. Auffret, I. L. Prejbeanu, and B. Dieny, IEEE Magnetics Letters **1**, 3000204-3000204 (2010).

244. P. N. Lapa, T. Khaire, J. Ding, J. E. Pearson, V. Novosad, A. Hoffmann, and J. S. Jiang, AIP Advances **6**, 056107 (2016).

245. J. A. Anthony, F. S. Daniel, F. Luigi, C. Gianluigi, J. R. Michael, F. Aviad, and E. P. Daniel, Nanotechnology **21**, 445202 (2010).

246. Y. Wang, P. Zhou, L. Wei, H. Li, B. Zhang, M. Zhang, Q. Wei, Y. Fang, and C. Cao, Journal of Applied Physics **114**, 153109 (2013).

247. S. Sarangi, S. P. Chockalingam, and S. V. Bhat, arXiv:cond-mat/0511705 (2005).

248. T. G. S. M. Rijks, W. J. M. d. Jonge, W. Folkerts, J. C. S. Kools, and R. Coehoorn, Applied Physics Letters **65**, 916-918 (1994).

249. S. P. Chockalingam, M. Chand, J. Jesudasan, V. Tripathi, and P. Raychaudhuri, Physical Review B **77**, 214503 (2008).

250. R. P. Erickson, K. B. Hathaway, and J. R. Cullen, Physical Review B **47**, 2626-2635 (1993).

251. J. C. Slonczewski, Physical Review Letters **67**, 3172-3175 (1991).

252. Z. Celinski, B. Heinrich, and J. F. Cochran, Journal of Magnetism and Magnetic Materials **145**, L1-L5 (1995).

253. A. Vedyayev, B. Dieny, N. Ryzhanova, J. B. Genin, and C. Cowache, Europhysics Letters **25**, 465 (1994).

APPENDIX A

SINGLE-DOMAIN COHERENT ROTATION MODEL

The total energy of a superconducting SV with a SAF per area, E_{Total}, is

$$E_{Total}(\varphi_1, \varphi_2, \varphi_3) = E_{Zeeman} + E_{AF} + E_{Paras} + E_{Uniaxial} + E_{Unidirect} =$$
$$- t_1 M_1 H \cos(\varphi_1) - t_2 M_2 H \cos(\varphi_2) - t_3 M_3 H \cos(\varphi_3) + \qquad \text{(A-1)}$$
$$+ J_1 (1 - \cos(\varphi_1 - \varphi_2)) + J_2 \cos^2(\varphi_1 - \varphi_2) + J_{PAR} (1 - \cos(\varphi_f - \varphi_2)) +$$
$$+ t_1 Ku \sin^2(\varphi_1 - \varepsilon_U) + t_2 Ku \sin^2(\varphi_2 - \varepsilon_U) + t_3 Ku \sin^2(\varphi_3 - \varepsilon_U) +$$
$$+ K_{EB} (1 - \cos(\varphi_1 - \varepsilon_{EB})),$$

where φ_1, φ_2, φ_3 are the angles between magnetization in the F layers and the magnetic field; ε_U is the angle between the axis of the uniaxial anisotropy and the magnetic field, ε_{EB} is the angle between the axis of the unidirectional anisotropy (pinning direction) and the magnetic field (Figure A.1), t_1, t_2, t_3 are thicknesses of the F layers, J_1 and J_2 are the coefficients of the bilinear and biquadratic interlayer coupling between the F1 and F2 layers of the SAF, J_{PAR} is the coefficient of the parasitic interlayer coupling between the Ff and F2 layers, Ku is the coefficient of the uniaxial anisotropy induced in the F layers due to the films growth in magnetic field, K_{EB} is the coefficient of the unidirectional anisotropy induced in the F1 layer due to proximity with the AF.

Minimizing $E_{Total}(\varphi_1, \varphi_2, \varphi_3)$ with respect to φ_1, φ_2, φ_3 enables finding stable magnetization configurations in the SVs in a magnetic field. A MathCad script was written for determining minima of the $E_{Total}(\varphi_1, \varphi_2, \varphi_3)$ function numerically. If the magnetic anisotropy of the system is present, that is Ku, $K_{EB} \neq 0$, the system may demonstrate a

hysteresis. The script does not look for global minima at each given field but for the local ones. Hence, it enables finding quasi-stable states realized for a hysteretic system.

For the simulations of the SAF stacks, it was assumed that M_3 = 0 emu/cm^3, J_{par} = 0 erg/cm^2, t_3 = 0 cm, K_{EB} = 0 erg/cm^3.

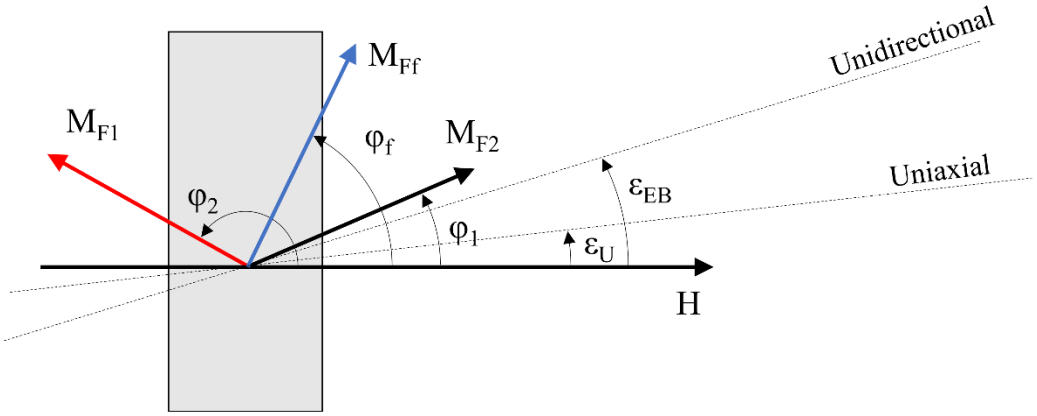

Figure A.1 The schematic illustrates the SDCR simulation model.